Varying the Porosity of Electrospun Monoaxial and Coaxial Collagen Nanofibers

A Thesis

Submitted to the Faculty

of

Drexel University

by

Ryan Christopher Gifford-Hollingsworth

in partial fulfillment of the

requirements for the degree

of

Master of Science in Materials Science and Engineering

June 2014

Dedication

I would like to dedicate this work to my parents Kirby Hollingsworth and Cynthia Gifford-Hollingsworth as well as my siblings Kirby Gifford-Hollingsworth and Katie Gifford for their unwavering love and support.

Aknowledgments

I would like to thank my principal investigator, Dr. Caroline Schauer for all of her support and guidance during my time here at Drexel University. I would also like to thank my committee members Dr. Christopher Li and Dr. Hao Cheng for all of their time and technical guidance.

I want to thank all members of the natural polymers and photonics lab for their support and friendship over the last few years. This group is truly like a family and I couldn't have done it without any of them. I would like to extended a special acknowledgment to Laura Toth as you spent much time mentoring and assisting me with my research.

I would also like to thank Dr. Palmese and his group for allowing me to use the equipment in their lab for sample analysis.

Table of Contents

List of Tables

List of Figures

Abstract

Varying the Porosity of Electrospun Monoaxial and Coaxial Collagen Nanofibers
Ryan Christopher Gifford-Hollingsworth
Dr. Caroline Schauer, Ph. D.

As the average age in the United States increases, so do the costs associated with a variety of chronic conditions, which when symptom management is applied can lead to drug tolerance and the onset of side effects over long term drug exposure. Personalized medicine is an area of research, which proposes to manage symptoms and/or treat disorders without long term tolerance or side effects. Electrospinning is a rapid, cost effective technique, which can be utilized to generate non-woven, nanofibrous matrices that resemble the body's own extra cellular matrix (ECM). The ability for these mats to resemble the natural ECM leads to high levels of cell adhesion, growth, proliferation and differentiation. The unique capabilities of electrospun matrices were investigated here by applying the technique to generate: matrices of gelatin and collagen with varying salt concentrations and matrices containing the glycosaminoglycan (GAG) chondroitin sulfate (ChS).

The gelatin and collagen matrices were analyzed for their ability to trap salts both within the matrix and within the individual fibers. The matrices were subsequently leached to form pores. The mats were analyzed using FESEM, FTIR and EDS to determine the presence and release of salt. It was shown that the salt entrapment could be controlled by controlling the solution salt concentration and that, after covalently crosslinking the fibers, the salts could be leached while maintaining some of the fibrous structure.

The ChS containing matrices were analyzed to determine the effect of blend polymer net charge on the fiber forming capacity of the polymer blend solutions. The mats were analyzed with FESEM, FTIR and EDS to determine the presence of the various blend polymers and ChS. It was found that the molar ratio of ChS:blend polymer in solution

played a large role in the concentration of ChS in the final fibrous matrices. Also, it was found that electrospinning another GAG, hyaluronic acid (HA), with ChS led to the highest concentration of ChS in the fibrous matrices. These mats will be further investigated for applications in regenerating cartilaginous tissue for articulating joint repair.

1. INTRODUCTION

1.1. PROBLEM STATEMENT

The ever-aging population and development of complex and evolutionarily advanced diseases and disorders have introduced new challenges in the fields of medicine and healthcare. It is estimated that by 2030 more than 19% of the total US population will be 65 or older and by 2050 this will increase to more than 20% [1]. As the population ages, the incidence of chronic health disorders such as Alzheimers, heart disease, cancer, other forms of neurodegenerative disorders, arthritis and many other less prevalent conditions, increases proportionally [2]. The most concerning aspect of the problem is that, despite the efforts of medical professionals to educate and treat these elderly patients, 80% of the older population is affected by at least one chronic condition and 50% is affected by two or more [2].

Although the incidence of health conditions is growing, large scale, clinically curative treatments are not yet readily available. This apparent gap has not gone unnoticed by the scientific community and a great deal of research has been directed toward finding treatments for chronic conditions such as heart disease, neurodegenerative disorders and arthritis [3, 4, 5, 6]. A large portion of the current research is focused on the development of regenerative medicine and pharmacogenomic treatments, both of which are considered to be individualized therapies. Prior to clinical trials and commercialization, these new treatment methods require a great deal of research and optimization. This process normally involves the expensive use of animal testing, a lengthy period of time from testing to trials and expensive high throughput screening. Some of the fall-backs of the current testing methods can be eliminated by developing better techniques and equipment to quickly and efficiently screen for more indicative cellular responses. This will help pharmaceutical and device manufacturers avoid costly ineffective trials and better treat the needs of each individual patient.

1.2. OSTEOARTHRITIS

Osteoarthritis (OA) is a disorder classified by the focal degeneration of articulating cartilage within synovial joints, which results in the hypertrophy of the surrounding bone [**Figure 1**] [7]. Patients with osteoarthritis often experience joint pain, local inflammation, decreased joint mobility and tenderness [8]; accordingly, OA of the knee and hip joints is one of the leading causes of pain and locomotive disability in the world [9]. While this disorder is not considered to be directly life threatening, it can drastically decrease the quality of life for those affected by it. The most startling aspect about this disorder is it's global prevalence. The Center for Disease Control and Prevention (CDC) estimated that approximately 27 million people within the continental US were affected by OA in 2008 and the World Health Organization (WHO), estimated that approximately 10% of the male population and 18% of the female population aged 60 or older were affected [10, 11]. Many of those who are affected require full locomotion of their limbs and joints for employment and/or other purposes, making this rheumatic disorder highly detrimental for them.

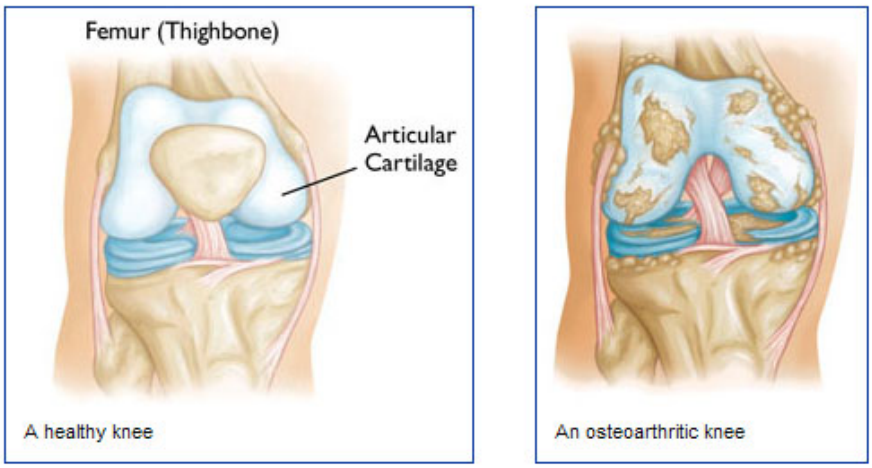

Figure 1: Normal articulating cartilage *vs.* OA of the knee demonstrating focal tissue degeneration (Source: [12])

As a result of the detrimental effects of OA on the locomotion and health-related quality of life, the afflicted individuals often look to treatment to help reduce the effects of this

disorder [13]. The good news for these patients is the number of available treatments, including pharmacological, non-pharmacological and surgical procedures. The down fall of these procedures is that many of these treatments provide a very limited degree of relief [9]. The low efficacy of treatments such as exercise rehabilitation, surgical debridement, osteotomies, arthroplasties and many pharmacological therapies, results in the need for total joint replacement. Total joint replacement is regarded as a last resort by most health professionals that will only be performed when all other treatment options have failed to provide sufficient relief. The reason being that the replacement does not increase the patients quality of life but only slightly decreases the effects on quality of life associated with OA [13]. Along with only minor positive effects, there exists the potential for the implanted joint to fail mechanically within a decade. In order to decrease the need for patients receiving total joint replacement, multiple prophylactic steps must be taken by both patients and physicians. According to treatment efficacy data, three major treatments have been shown the most effective. The first treatment involves the prevention of OA by eliminating potential risk factors including elevated BMIs, knee injuries and intensive physical activities [14]. The remaining two treatments involve local injections of hyaluronic acid (HA) into the synovial joint and treatments with administered chondroitin sulfate (ChS). The injection of HA into the synovial joint showed the longest lasting effect on joint mobility, function and pain reduction while ChS treatment helped to decrease the rate of hypertrophy in the joint [9].The development of an implantable, nanofibrous scaffold composed of HA-ChS could provide increased benefits for patients suffering from OA by serving as a matrix for regeneration of the natural tissue.

1.3. ATRIAL FIBRILLATION

Atrial Fibrillation (AFib) is defined as a ”supraventricular arrhythmia characterized by uncoordinated atrial activation with consequent deterioration of atrial mechanical function” [15]. AFib can be more simply described as an irregular heart rhythm which originates

from the uncoordinated firing of a cluster of contractile cardiomyocytes within the atrium. This disorder is normally diagnosed after patients present with symptoms of dyspnea, heart palpitations or an irregular heart rhythm. The irregularities are further investigated and diagnosed via an electrocardiogram (ECG) [16]. The prevalence of AFib in the US is quite high as approximately 3.22 million or 1.1% of the total US population was diagnosed in 2005. This number is expected to more than double to 8 million by 2050 [**Figure 2**][17]. Those who are afflicted are more likely to have co-morbidities such as hypertension, tachycardiomyopathy, valvular heart disease, atrial septal defects, obesity, diabetes mellitus, chronic obstructive pulmonary disease (COPD), sleep apnea, chronic renal disease, thyroid dysfunctions and coronary artery disease [16]. The list of co-morbidities is long and patients diagnosed with AFib tend to experience further increases in the occurrence of these disorders as they age. It has been demonstrated that AFib afflicted patients, especially those within the geriatric communities, are over four times more likely to fall victim to congestive heart failure and five times more likely to experience a stroke than their non-afflicted peers [15, 17].

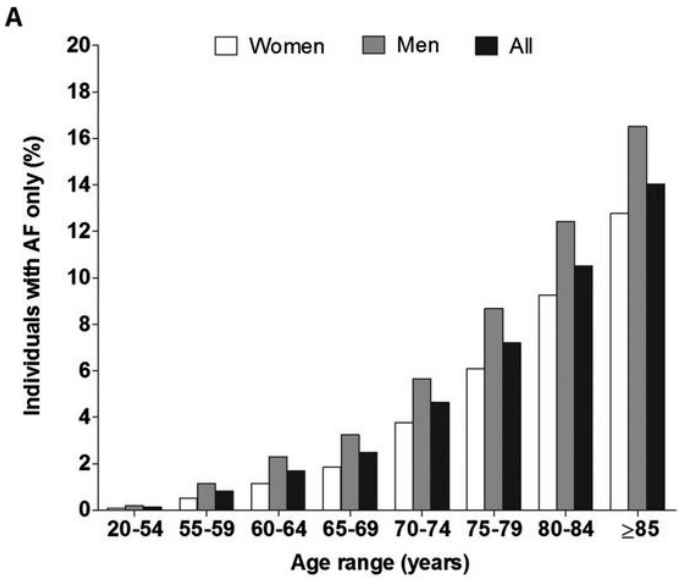

Figure 2: Prevalence of AFib by age and gender in the US (Source: [17])

With such a high incidence rate and large array of co-morbidities, AFib requires treat-

ment and monitoring. A number of possible treatments are currently available which include both surgical and non-surgical approaches while monitoring is subject to mainly implantable monitors or ECG monitoring. The majority of current treatments avaiable fall into one of four major categories: cardioversion (resetting the heart rate), heart rate control, catheterization/ablation techniques or blood clot prevention/management [18]. Many of these procedures are risky and involve long term prophylactic therapy with medication post treatment. In the case of cardioversion, the reset heart rate needs to be maintained long term, utilizing one of an array of medications including vitamin K antagonists (i.e warfarin) and antiplatlet therapy [19]. The available medications indicated for this use have been found to have a very low success rate leading to patients having to undergo other surgical procedures and or another cardioversion [18]. These downfalls present the need for new treatments and medications that can be screened quickly and efficiently for their effectiveness in-vitro. This need can be satisfied with the development of an inexpensive, efficient, bench top screening tool that mimics the natural environment and returns an optimized, clinically significant output.

2. BACKGROUND

2.1. ELECTROSPINNING

Electrospinning is a well known and highly utilized electrostatic fabrication method, used to fabricate nanometer to micrometer sized polymeric based fibers. This method can and has been used to create fiber mats that are composed of natural and/or synthetic polymers with fibers that randomly aligned, directionally aligned or a combination of both [20, 21, 22]. The technique involves pumping a polymer solution through a conducting syringe needle, attaching a high voltage power source to the conductive needle tip and to a collection device at some distance from the needle tip and applying a potential across the distance. During processing, a Taylor cone is formed as a result of the electric field overcoming the the surface tension of the solution. The polymer fibrils are pulled by the applied electrostatic field and the long continuous strands land on the collector. The use of electrospinning as a fabrication technique was first patented by Anton Formhals in 1934 although previous research and literature on electrostatic spraying led to this discovery [21, 23]. Despite its early discovery, its use was not commercially relevant until the 1970's, and within the last two decades, there has been a drastic increase in research efforts devoted to the use of this novel method in a multitude of fields [**Figure 3**][20, 24, 25]. These fields are mainly regenerative medicine, drug delivery, capacitors and energy storage, energy generation, filtration and clothing [20].

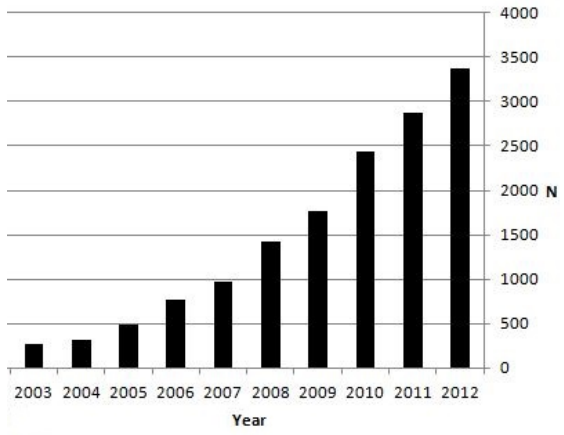

Figure 3: Number (N) of scientific publications and patents per year (2003-2012) referencing ”electrospinning” (Source: SciFinder)

The recent flux of literature and research involving electrospun fiber mats is due to the unique properties and vast assortment of fiber mats that can be generated. An example of this is the use of electrospun polymeric fibers as a precursor for ceramic or metallic fibers, which can then be utilized for a wide array of applications [26, 27, 28, 29, 30]. Aside from the utilization of electrospinning to create materials from the majority of material classes, electrospinning is well known for its ability to create fibers with advantageous properties. These properties include a high surface to volume ratio, a large degree of porosity, long fiber lengths and small fiber diameters. The fiber mat properties can be controlled by changing the solution and spinning/processing parameters [**Table 1**] [31, 32, 33]. The number of variables involved in the formation of fibers is large and is one reason as to why the technology is still being investigated in research and development labs and is rarely seen in large scale operations.

Table 1: Electrospinning Parameters and Effects

Solution Parameters	Processing Parameters	Effects
Volumetric charge density	Distance from collector	Solution spraying
Solution viscosity	Applied electrical potential	Varied fiber diameters
Solution density	Initial jet radius	Varied fiber morphology
Surface tension	Relative humidity	Film formation
Molecular weight		
Vapor diffusivity		
Solvent vapor pressure		

The method of spinning can also be varied. Some examples include varying the environment by processing in a chemical vapor chamber, changing the type of collector and electrospinning multiple polymers from different solutions at once. The latter of these options is known as coaxial electrospinning and involves pumping multiple polymer solutions into a single charged tip and pulling the fibers concurrently. This method is relatively novel while the majority of previous and current literature involves the use of a monoaxial electrospinning set-up.

2.1.1. MONOAXIAL

Monoaxial electrospinning is the most prominent method of electrospinning used to electrospin a single polymer solution. The solution may contain more than one polymer or a number of other solutes that can be trapped and pulled along with the polymer jet. The set-up can be made to spin horizontally, vertically onto a rotating drum, onto a conductive plate or into a solution bath [**Figure 4**]. The variety of these monoaxial set-ups have been applied to help researchers better understand the method and its applications to a higher degree. These researchers have attempted to use monoaxial electrospinning to develop polymer blend mats, drug encapsulations, unique tissue scaffolds, highly porous capacitors, piezoelectric generators and many other specialized mats for which a new and creative set-up was required [23, 25, 34, 35, 36].

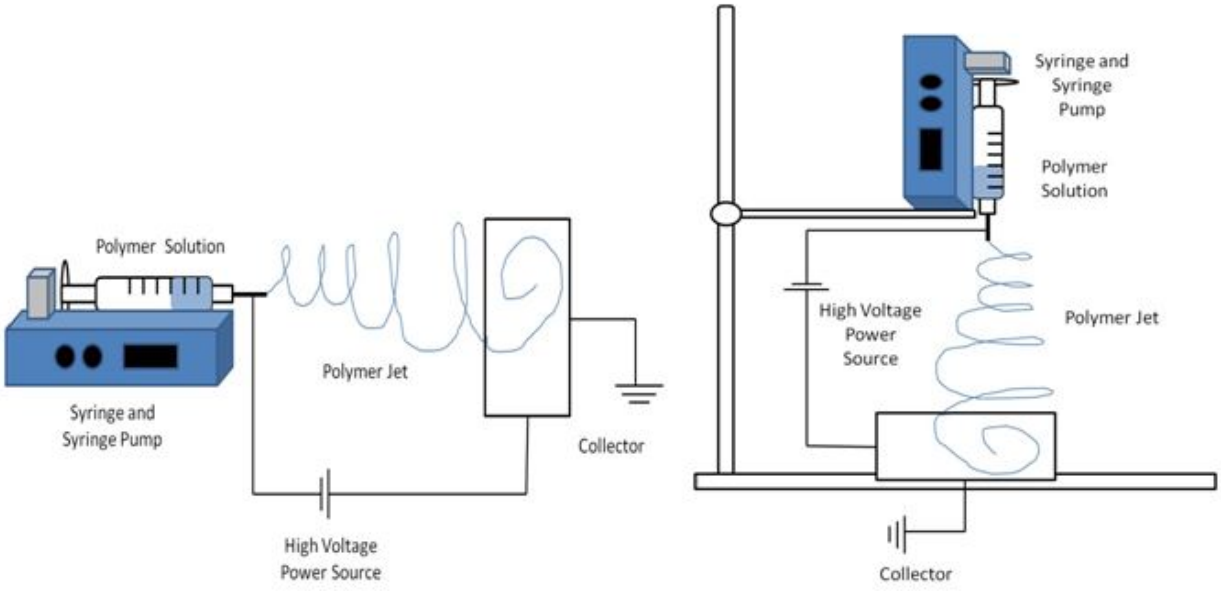

Figure 4: Monoaxial electrospinning set-up showing both horizontal and vertical set-ups

Along with a great deal of innovative research and set-ups, has also come a great deal of insight into the electrospinning process itself. A great deal of knowledge about the electrospinning process and its parameters have come from monoaxial electrospinning research [32, 33, 37, 38]. This knowledge has led to increases in specifically tailored polymer mats and a decrease in time wasted when altering parameters to optimize a process. These insights have also given information about monoaxial electrospinning's drawbacks and limitations, which has led to more novel methods of electrospinning.

2.1.2. COAXIAL

Coaxial electrospinning is a subset nanotechnology fabrication method of electrospinning. Its use was first discussed approximately 10 years ago by several research groups as a method to develop micro and nanofibers consisting of a core and a shell polymer [39, 40, 41, 42]. The process involves the use of two or more spinnerets that pump two different and commonly immiscible polymer solutions at varying rates through a single port. The shell polymer flows around the core polymer's spinneret (needle point) until the end of

the head at which point the two solutions come into contact to be pulled by the electrostatic potential [**Figure 5**]. The core-shell structure is commonly maintained during this process and long, continuous, concentric core-shell fiber mats are produced. This is not the only method used to fabricate coaxial fibers, however, and a great deal of interest has been expressed in the utilization of emulsions to coaxially electrospin from a single solution [43]. This application is justified by its ability to be more easily scaled up to a commercially applicable process [44].

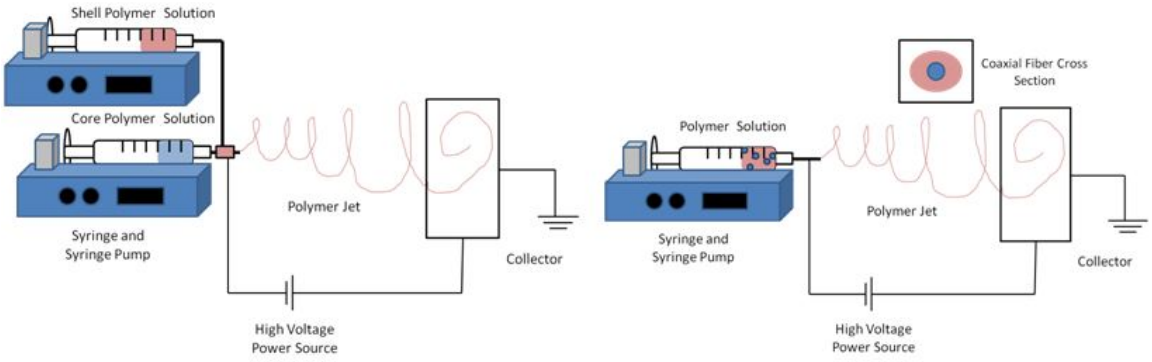

Figure 5: Coaxial electrospinning set-up showing a horizontal set-up although others are possible (L) double spinneret set-up (R) emulsion set-up

The applications for coaxial fibers are just as vast as those associated with monoaxial fibers, although the applications of coaxial fibers have found great success in a few specific fields including controlled release rate drug delivery, nanosensors, optical and electrical cables, capacitors, solar cells, and even in the production of long carbon nanotubes for nanofluidic devices [24, 43, 45]. What is most promising about these fibers is that as more and more research is conducted the fiber mats being produced are becoming increasingly tailored based on known parameters. For coaxial fibers, the majority of known parameters remain the same as the monoaxial case with the addition of parameters such as interfacial energy, miscibility and surface tension between the two polymer systems. These parameters drastically affect the formed fibers morphology including porosity, surface roughness, continuity of the core/shell and the physical properties of the polymers [46, 47, 48].

Some promising and very thought provoking research has come from coaxial electro-

spun fiber mats in recent years. By utilizing the unique functionalities of these fibers to completely encapsulate both, materials with a high degree of spinnability as well as materials with low or no spinnability, researchers have spun material systems unachievable using monoaxial systems. Such systems include spinning biological substance in the core such as live cells, bacteria, solution sensitive biomaterials and hollow fibers [24, 49, 50, 51]. All of this research has not gone unnoticed by industry and several patents have been filed and industrial upscaling of these processes has begun within the last few years.

Although coaxial electrospinning maintains a large base of research with just two solutions an even more recent undertaking has been noted for a triaxial system. In the triaxial system, three solutions are spun resulting in a shell–core–core structure. This research has already proven to have applications in drug/molecule release systems and its application in other fields is sure to be established as the knowledge of the system increases [52, 53].

2.2. FIBER POROSITY

Materials with a large density of pores are greatly sought due to their ability to interact with many systems including but not limited to capacitors, biomimetic scaffolds and filters. The need for highly porous structures in these applications is due in part to the requirement for these systems to have a large specific surface area and to allow for an elevated total flow. These parameters are important for high capacitances in capacitors, for cell spreading and nutrient flow in scaffolds and for increased levels of filtration and permeability in water filters [54, 55, 56].

With the increased need for these highly porous materials many fabrication methods have been established and suggested as potential options. The methods most often cited include forms of lithography, casting/templating, controlled polymerization and electrospinning [54, 55, 56, 57, 58]. The later of these methods has been highly utilized due to its well known ability to consistently generate fiber matrices with an extensive degree of porosity and thusly a large specific surface area. What is important to note about electrospinning

is that two different types of porosities are make up the overall porosity and specificity of the final product: interfiber porosity and intrafiber porosity. The first represents the vacant space between individual fibers while that later represents the porosity (surface roughness) of each individual fiber.

2.2.1. INTERFIBER POROSITY

Interfiber porosity is defined as the vacant space between fibers in a fibrous mesh/matrix. Interfiber porosity is extremely important in cellular research applications, it permits nutrient and oxygen diffusion and cellular ingrowth [56, 59, 60]. If the interfiber pores are too small then diffusion and ingrowth will be restricted and if the density of pores is too low, then the cells will have a decreased resource of nutrients. These result in decreased levels of proliferation, migration, spreading and adhesion [59]. Researchers now attempt to increase both the pore size and the density of pores without changing the fiber size for better cell proliferation, migration, spreading, and adhesion.

In order to achieve these porous matrices, several methods have been attempted to increase the pore size and connectivity of pores, including wet electrospinning, salt or polymer leaching, phase separation, laser irradiation, electric field control and cryogenic electrospinning [60, 61, 62, 63]. Of these methods wet electrospinning and salt leaching are the most cost efficient ways to control the pore structure and increase cellular ingrowth.

Wet electrospinning involves electrospinning into a solution bath rather than onto a solid collector. The density of the mats can be decreased by about half and a corresponding increase in the porosity and pore size of the structure is seen [**Figure 6**]. The fiber morphology including pore structure and pore density can be altered by altering the solution and it's associated surface tension resulting in a semi-controllable process [64, 65]. The other, more commonly cited method of salt leaching is the use of salts into the fiber mats *via* a suspension in the electrospinning solution, a sieving process onto the forming mats or as a semi-coaxial deposition process [66]. This method is widely cited and utilized due

to its simplicity and controllable parameters such as varying salt size and concentration to increase the formed pores and number of pores. Similar to wet electrospinning, cell studies on these porous mats have demonstrated a greater degree of cellular ingrowth than non-salt leached mats [59, 67].

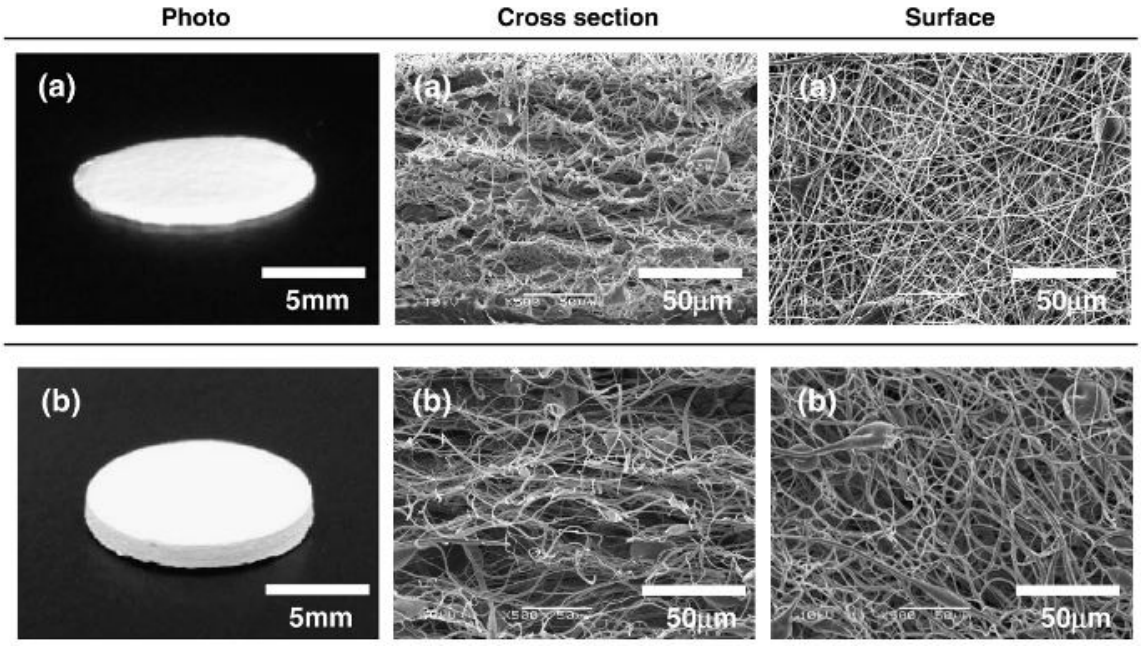

Figure 6: SEM images of wet electrospun poly (glycolic acid) fiber mats (b) versus normally electrospun poly (glycolic acid) mats (a) showing the difference in pore and scaffold structure (Image Source: [64])

It is important to note that despite the promise these methods hold there are also some drawbacks. For the wet electrospinning process choosing the right solvent bath can be difficult because it must not alter or swell the fibers. This method also requires the need for lyophilization post-processing. Salt leaching maintains drawbacks such as heterogenity of pores as well as difficulty in removing deeply embedded salt particles from the mats.

2.2.2. INTRAFIBER POROSITY

Intrafiber porosity is described as the vacant space within an individual fiber including both the degree of surface roughness and porous channels through the fiber. This porosity is also commonly referred to as nanoporosity due to the extremely small nature of the

pores. What is important about being able to increase the intrafiber porosity is the effect it has on the hydrophobic or hydrophillic properties of the fibers. Nanoporosity will enhance the intrinsic hydrophobicity or hydrophilicity of the polymer fibers [24]. Another important feature of nanoporosity is that in coaxial systems the core polymer will experience a greater degree of interaction with the environment if the shell polymer maintains a large degree of nanoporosity. This type of morphology would be important for coaxial drug delivery systems and biosensors while the increases in hydrophilicity or hydrophobicity are of great value in tissues scaffolds for increasing protein and cell adhesion.

Due to the unique and specific applications of fibers with these morphologies along with the relative youth of this specific field of study, only a small amount of literature has been published on the topic of processing parameters to form these structures. What has been published though, indicates that there are several methods in which to achieve this morphology including sacrificial polymer blends, the breath figure process and thermally induced phase separations. The most commonly cited of these processes is the use of co-solvents with varying evaporation rates and vapor pressures, to induce pores that form during the thermal phase separations between the polymer and the solvents [62, 68, 69, 70]. Despite this method being the most commonly cited there are drawbacks due to the complicated nature of picking the correct solvents. A more simplistic method is that of the sacrificial polymer/particle leaching method which, although not as well cited for generating interporosity, maintains a good deal of research. In this fabrication method, two polymers that phase separate when electrospun or a polymer and particle type are chosen such that specific domains are formed within the individual monoaxial fibers after electrospinning. One of these polymers or the particles are then leached out of the system resulting in highly nanoporous fiber mats [**Figure 7**] [39, 71, 72].

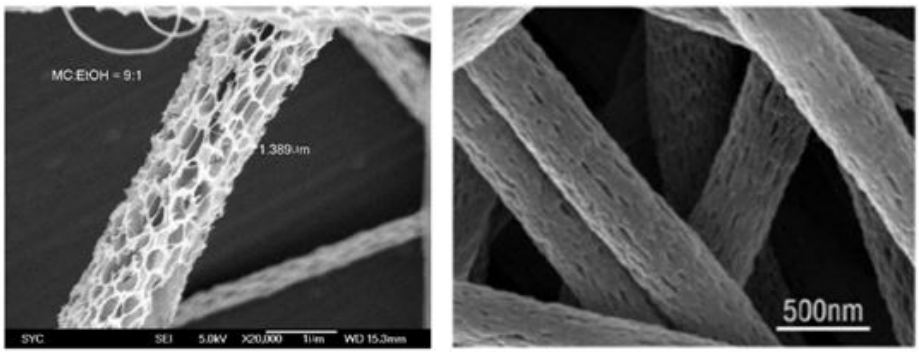

Figure 7: SEM images of nanoporous fibers formed via (L) phase separation (Image Source: [62]) and (R) polymer leaching (Image Source: [71])

Utilizing methods similar to those used by Mehraben *et al*, nanoporous biomimetic scaffolds can be produced for tissue regeneration and cellular applications. This system is simple in that they use nanosized salt particles can be suspended in solution with the polymer and pulled along with the polymer jet. The salts can then be leached out in solvent leaving behind porous fibers similar to those seen with other leaching methods. The pore size can be altered by altering the salt crystal size and concentration making the system controllable. Such fibers would present themselves for many biological applications.

2.3. POLYMERS

Polymers are classified as macromolecular chains which consist of many smaller repeating units known as monomers. Synthetic polymers have been produced since their discovery in the 1830's. The first known polymeric materials were vulcanized rubber and the precursor to nitrocellulose. These initial discoveries involved modifications to natural polymers while the first industrially produced synthetic polymer was Bakelite, produced by Leo Baekeland in 1907 [73]. Since their discovery and establishment of use in industry, polymers have maintained a unique place in technological developments and innovations.

Polymers are unique from other materials in that they form completely amorphous solids or structures with varying degrees of crystallinity depending on the processing steps and side groups present. The most basic polymer structure is polyethylene, which con-

sists of a carbon backbone and hydrogen side groups. These side groups can be replaced with other groups such as hydroxyls, halogens, carboxyls and amides. These side chains are extremely important in determining the structure and function of the polymer and their importance is apparent in all applications.

The mechanical, chemical, electrical and chemical properties can be easily altered by changing the molecular weight (MW), the side groups or performing further processing. Primary processing techniques include the techniques used to initially form the polymers. The most commonly cited methods are injection molding, extruding, casting and more recently electrospinning. The structure of the polymer can be altered during the primary processing process by adding additives such as vulcanizing agents, dyes, salts and many other agents or by altering the processing parameters such as temperature, speed, volume, molecular weight and other parameters dependent on the specific method. After the initial product is formed its properties can be further altered by techniques such as crosslinking the side groups on the polymer chains and modifying the surface side groups.

2.4. SYNTHETIC POLYMERS

2.4.1. POLY (ETHYLENE OXIDE)

Poly (ethylene oxide) (PEO) is a very common polyether, which has found uses as applications in fields ranging from medicine and commercial products to chemical and biological processes. PEO consists of an opened ethylene oxide ring monomeric unit which can form polymeric chains of varying molecular weight [**Figure 8**].

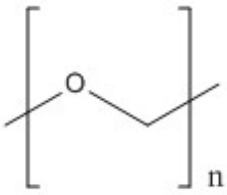

Figure 8: Chemical structure of PEO

PEO has been used in biomedical research since the 1960's due to its biocompatibility

and its controllable water solubility properties [74, 75]. The ability for this polymer to have a controllable degradation in aqueous solutions makes it a prime target for research into drug delivery and bioresorbable scaffolds [76]. Aside from being used as coatings in implantable biomedical devices, PEO is rarely processed without a blended polymer or another chemical component, such as a drug stored inside of its micelle structure. The use of PEO in this manner is noted as using the polymer as a carrier, which can prove to be very promising for processing or transporting previously difficult systems.

The use of PEO as a carrier polymer has been well investigated and utilized due to the ability for this synthetic polymer to be processed *via* electrospinning at concentrations well above its chain entanglement concentration [77, 78, 79, 80]. Although PEO has been used as a carrier polymer for many natural polymers such as alginate, hyaluronic acid (HA) and chitosan, there has been little research on the use of PEO as a carrier for most natural polymeric glycosaminoglycans (GAGs) such as chondroitin sulfate (ChS), dermatan sulfate and keratan sulfate.

The use of PEO with sulfated GAGs has been primarily demonstrated *via* hydrogel production and most of these studies demonstrated very promising results about decreased inflammation and increased specific tissue regeneration [81, 82, 83]. These promising results demonstrate the potential application of blended PEO-ChS electrospun nanofibrous scaffolds for similar applications. Due to the known carrier potential of PEO along with the recent research demonstrating the in *vivo* potential of PEO-ChS hydrogels an attempt to induce greater cell proliferation and viability by increasing the pore concentration and surface area by electrospun fabrication is supported.

2.4.2. POLY (VINYLIDENE FLUORIDE-CO-TRIFLUOROETHYLENE)

Poly (vinylidene fluoride-co-trifluoroethylene) (PVDF-TrFE) is a widely studied ferroelectric copolymer, which exists in one of two major crystal polymorphs, α or β. Although five distinct crystal polymoprhs exist for the PVDF monomer, the addition of the copolymer

induces only these two major forms. The major form of PVDF-TrFE at room temperature is the piezoelectric β phase, which is induced in PVDF by the addition of the TrFE monomers [84, 85]. Other methods of inducing the β phase have been demonstrated including poling, mechanical drawing, solution specific crystallization, addition of copolymers or nanoclays and several other methods [84, 86, 87]. The copolymer repeat unit consists of a vinylidene fluoride monomer covalently attached to a trifluoroethylene monomer [**Figure 9**]. The polymer is processed *via* free radical polymerization of the VDF and TrFE monomers.

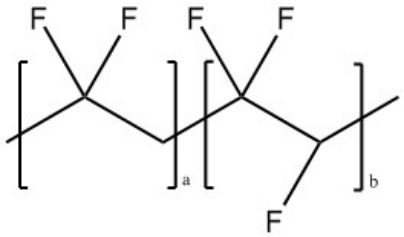

Figure 9: Chemical structure of PVDF-TrFE

PVDF-TrFE has been used as a component in several areas of research including nanocomposite dielectrics for energy storage, low power generation, sensors and biomedicine [88, 89, 90]. The two fields of most interest for the current study include its use a sensor and as a biomedical device in previous literature. In these fields, there have been several studies looking at potential applications, drawbacks and improvements of utilizing PVDF and its copolymers. These studies include observing PVDF-TrFE composites for future DC magnetic field sensors, as tissue scaffolds which induce differentiation, as pressure sensors and as drug delivery devices. [91, 92, 93, 94].

2.4.3. POLY(ARYLIC ACID)

Poly(acrylic acid) (PAA) is an anionic synthetic polymer which is produced from the free radical polymerization of acrylic acid monomers, the repeat unit is demonstrated in**Figure 10**. This polymer was first patented as a super absorbent in 1966 due to its ability to swell to more than 1000 times its original mass in the presence of water [95, 96].

Since its original patent this polymer has been utilized across a variety of fields including as a cleaning agent, as an absorbent in diapers, as a component in drug delivery systems, as a component in heavy metal filtration and as substrates for cell adhesion and activation [96, 97, 98, 99].

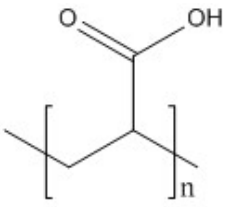

Figure 10: Chemical structure of PAA

Although there are many applications for PAA and its derivatives, PAA is rarely used without modification. Typical modifications include surface functionalization, copolymerizaiton, blend polymer and nanoparticle additions [98, 100, 101]. Of interest to this proposal are the blend and copolymer modifications. These modifications have been commonly researched for use in biomedical applications as drug delivery systems, layer-by-layer (LBL) micelles and scaffolds, and in electrospun composite scaffolds for tissue regeneration [98, 101, 102]. In a study conducted by McKeon-Fischer *et al.*, a PAA and poly (vinyl alcohol) (PVA) polymer blend was used as a carrier polymer in a coaxial set-up for poly (ε-caprolactone) and carbon nanotubes [102]. The generated scaffolds were then analyzed for their potential as artificial skeletal muscle.

Despite PAAs use as a carrier polymer and its applications in biomedicine, it has received little attention as a potential carrier for glycosaminoglycans (GAGs) such as chondroitin sulfate. This application is of interest due to PAAs ability to act mechanically similar to that of articulating cartilage when blended with other polymers [103]. The limited research that has been conducted involving PAA and GAGs involved the use of polyelectrolytic complexes of PAA and hyaluronic acid (HA) and their applications in drug delivery [104].

2.4.4. POLY(ALLYLAMINE)

Poly(allylamine) (PAAm) is a synthetic cationic polyelectrolyte, which is synthesized by the addition polymerization of allylamine monomers [**Figure 11**]. PAAm is used in many applictaions but is very well established for its use as a cationic polymer in polyelectrolytic complexes and layer-by-layer (LBL) films [105, 106, 107, 108]. These LBL films have been applied in a variety of fields including forward osmosis membranes, one dimensional nanowires, drug delivery vesicles [108, 109, 110].

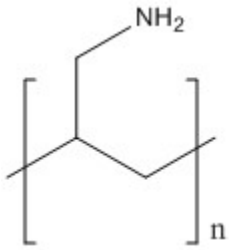

Figure 11: Chemical structure of PAAm

Aside from PAAms use in LBL layered films and non-planer surfaces, it has also been investigated for its potential application as a nanofibrous mat fabricated *via* the electrospinning method. By utilizing this method, researchers can fabricate two and three dimensional matrices, which exhibit an increased surface to volume ratio with respect to a film of comparable size. This increased surface availability will also act to increase the interaction of the cationic pendant groups with the local environment. Researchers have taken advantage of this property by adding additional coatings, drugs, polymers and other surface modifications to electrospun PAAm mats. Chunder *et al* have shown that by electrospinning these polyelectrolytes, their ionic groups remained available for further layering with polyelectroylyte coatings and oppositely charged drug loading [111]. Research by Kundu *et al* also demonstrated that the availability of free amino groups is important for functionalizing the PAAm mats and that the availability of free amino groups could be increased by utilizing the electrospinning fabrication technique [112].

Despite the extensive research into the use of PAAm as a candidate for drug delivery, there has been little research into the use of electrospun PAAm in other areas of medicine. Schiffman *et al* investigated the potential of using such mats in future biomedical applications and found that when crosslinked these fibers showed promise [113]. This studies' findings, along with PAAms ability to be functionalized with a wide array of molecules, makes it appealing for future research in biomedicine and as a potential carrier polymer for important biomolecules.

2.5. NATURAL POLYMERS

2.5.1. CHONDROITIN SULFATE

Chondroitin sulfate (ChS) is a glycosaminoglycan (GAG) which consists of repeating residues of the amino sugar, *N*-acetyl-galatosamine, and the hexuronic acid, D-glucuronic acid [**Figure 12**]. This repeat unit is sulfated at either the 4- or the 6- position of the *N*-acetyl-galatosamine, which results in the two major occurring types of this GAG, chondroitin sulfate A and chondroitin C, respectively. ChS is found primarily as a side chain of the proteoglycan (PG), aggrecan which is a major component in cartilage, acting as a primary source of shock absorption and as an initiator for cell to extra cellular matrix (ECM) interaction [114].

Within the past few decades ChS has been researched as a potential therapeutic agent for the treatment of osteoarthritis when administered either orally or directly into a joint. Many of these clinical studies have demonstrated that ChS, when administered orally, will show significant decreases in disease progression in comparison with placebo controls [115, 116, 117]. The patients in these trials also reported greater joint flexibility, less pain and the joint space in treated patients was maintained while placebo and untreated patients experienced a decrease. Unfortunately, despite these promising clinical trials other studies have shown that ChS in poorly absorbed in the gastrointestinal (GI) tract and has a short biological half life of 3-15 minutes in the circulatory system [118].

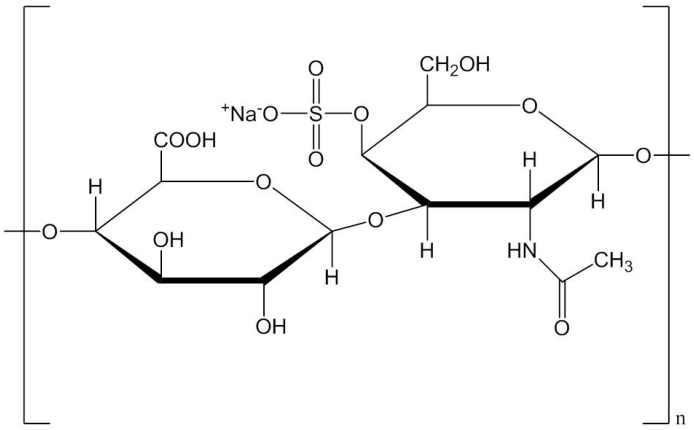

Figure 12: Chemical structure of Chondroitin Sulfate A sodium salt

Promising results of ChS as a therapeutic agent for the treatment of degenerative joint disorders, such as osteoarthritis, spurred interest in ChS as a target for more direct treatments including regenerative medicine. Several studies have shown that incorporation of ChS into fibrous mats and hydrogels is important for the onset and enhancement of chondrogenesis [119, 120]. Coburn *et al* have demonstrated that the incorporation of ChS into their electrospun poly (vinyl alcohol) (PVA) matrices induced markedly increased collagen type II production both *in vitro* and *in vivo* [119]. Also, earlier work by Varghese *et al* showed that the inclusion of ChS inhibited mesenchymal stem cells (MSCs) from further differentiating into hypertrophic chondrocytes as well as increasing the production of cartilaginous tissue [121]. ChS has also showed promise as a potential agent in promoting regeneration of other tissues as well including hepatic and several cell types within the central nervous system (CNS) [118].

2.5.2. HYALURONIC ACID

Hyaluronic acid (HA) is a non-sulfated GAG which consists of repeating disaccharide units of β-1,4-D-glucuronic acid and β-1,3-*N*-acetyl D-glucosamine [**Figure 13**]. This polysaccharide is found within many tissues of the human body including the ECM of cartilage tissue [122]. It's primary functions in the ECM have been noted as water hemeostasis,

filtration, lubrication, wound repair, cell signaling, morphogenesis, matrix organization and plasma protein distribution [122, 123].

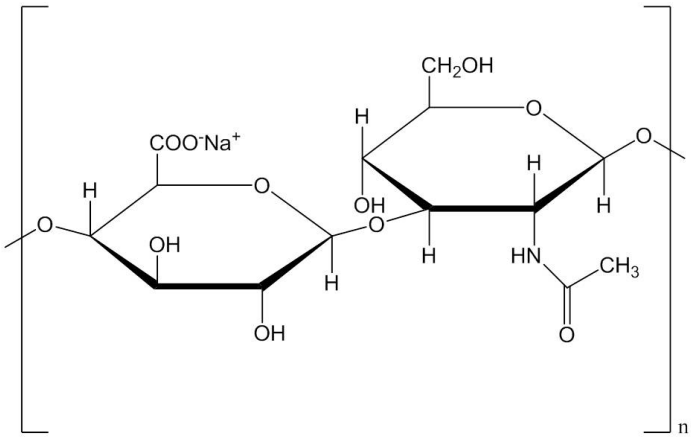

Figure 13: Chemical structure of HA sodium salt

HA has been investigated and utilized clinically for over 30 years. It has been used clinically as an agent in viscosurgery, viscoaugmentation, viscoseparation, viscosupplementation and viscoprotection [124]. Of these areas, viscosupplementation has drawn great attention and its use and efficacy in the alleviation of pain and decreased joint mobility in osteoarthritis has been of greatest interest. Intra-articular hyaluronic acid (IAHA) injections have been given since the late 1980s for treatment of the symptoms associated with osteoarthritis including joint pain and decreased joint mobility [124]. A recent meta-analysis by Bannuru *et al* in 2011 concluded that IAHA injections were acting therapeutically to reduce symptoms at 4 weeks post injection, with the therapeutic effect peaking at about 8 weeks but still remaining detectable up until 24 weeks post injection [125]. The study also concluded that IAHA injections performed at a much higher rate then its common alternatives including acetominophen, nonsteroidal antiinflammatory drugs (NSAIDs) and cyclooxygenase-2 (COX-2) inhibitors [125]. Other methods of administration of HA aside from intra-articular injections have been attempted but have much lower efficacy due to the rapid clearance of HA from circulation by several organs including the liver and spleen [126].

The vast success of IAHA injections has spurred a great deal of interest in utilizing HA as either a drug delivery system, an encapsulated therapeutic agent or as a scaffold in regenerative medicine. Researchers have found that HA hydrogels and electrospun mats can be conjuagted with a wide array of drug molecules, which upon the enzymatic degradation of HA, can be moved across the cell membrane *via* CD44 receptors and release the drug intracellularly [127]. Other research has focused instead on the use of HA hydrogels for either cell or molecule delivery [123]. A study by Toh *el al* in 2010 demonstrated that the use of a HA hydrogel seeded with human embryonic stem cells (hESCs) could act to repair an osteochondral defect without any long term tumorigenicity while maintaining its viability [128]. Other studies have looked instead at using HA hydrogels as a scaffold loaded with growth factors in many different tissues [123].

2.5.3. COLLAGEN

Collagen is the most abundant protein in all mammalian species and it makes up just under one third of all the proteins in humans. This abundant protein exists in 28 different forms, a result of the 46 unique polypeptide chains, which have been observed in the many forms of collagen in vertebrates [129]. This polypeptide is most commonly known for its role as the major structural protein in the human body and for its unique triple helix quaternary structure. The well-noted, triple helix structure is a result of the arrangement of amino acids in each individual peptide chain. Although the amino acids vary within the backbone it has been established that every third amino acid must be a glycine (Gly) in order for the triple helix to form. This results in a polpeptide chain with a repeating unit of three amino acids labeled as Gly-X-Y, with X being primarily proline (Pro) and Y being primarily hydroxyproline (Hyp) [**Figure 14**] [129, 130]. The individual triple helices, also referred to as tropocollagen, then arrange themselves into microfibrils, which are then crosslinked by lysyl oxidase to form collagen fibers [129].

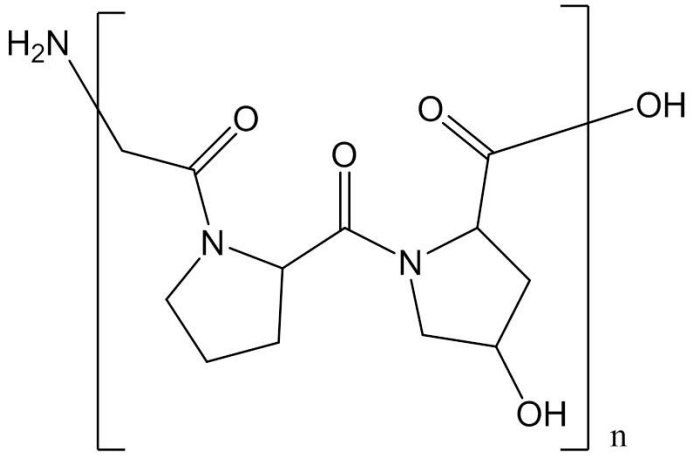

Figure 14: Chemical structure of Collagen's major subunit

Collagen has been well-researched and is greatly utilized in a wide variety of biomedical applications. It has been investigated and utilized as a material for skin grafts, bone-graft substitutes, drug delivery, metal implant coatings, thrombogenic sealants, sutures and as cell scaffolds for a variety of tissues [131, 132, 133]. Of greatest interest is the use of collagen as a scaffold for cell seeding. These scaffolds are typically electrospun nanofibrous mats or hydrogels and are normally physically or chemically crosslinked to increase their mechanical and chemical stability. Researchers have also synthesized collagen scaffolds as bi- and tri-polymer systems in order to increase their chemical stability. Several studies have demonstrated the success of these collagen matrices for cellular adhesion, growth and proliferation of the tissue of interest [134, 135, 136, 137]. These scaffolds have not been without drawbacks including low mechanical stability of collagen and poor cell infiltration. Although these issues present complications researchers have already started to work to mitigate these effects by generating matrices with greater degrees of crosslinking and with higher porosity.

2.5.4. GELATIN

Gelatin is a natural polymer that is derived from both mammalian and non-mammalian collagen sources. Gelatin is formed when collagen, typically collagen type I, is hydrolyzed

via acidic or alkaline processing. The hydrolysis of collagen results in the loss of the unique collagen triple helix quaternary structure. The hydrolysis is considered to be irreversible and gelatin can never be fully renatured to form collagen but only a gelatinous triple helical structure resemblant of the tropocollagen structure [138]. The main repeating subunit of the polypeptide chain is almost exactly the same as its parent protein collagen with Gly-X-Y representing the most prevalent amino acid residues, where X is mostly proline and the majority of Y residues are hydroxyproline [**Figure 14**] [130]. These residues are extremely important in order for the triple helix to form at low temperatures and for gelling to occur as the quaternary structure forms. This formation of the structure at low temperatures is inverse to that of its parent in which the triple helical structure of collagen forms as the temperature raises slightly from 20 to 28 °C [138]. Along with these three primary amino acids involved in the structural conformations of the gelatin protein there are also many other amino acid residues of importance within the polypeptide. One amino acid sequence of great importance for cell proliferation, growth and adhesion is the arginine-glycine-aspartic acid sequence found in gelatin [139]. This sequence along with the known structure makes gelatin a prime target protein for biomedical applications.

The ability for gelatin to form a structure similar to that of collagen has proven to be extremely important in utilizing the cheaper, much more readily available denatured form of collagen in biomedical applications. The use of gelatin in biomedical device and drug delivery applications has been and continues to be vastly studied [139, 140, 141, 142, 143]. The majority of this research uses gelatin in a co-polymer matrix with either another natural polymer or synthetic polymer in order to increase the matrices' mechanical and or specific biochemical properties. Along with adding other polymers and growth factors the gelatin matrices are rarely generated *via* an electrospinning process and normal processing techniques are hydrogel and film forming techniques. This is in part due to the hindered fiber formation of gelatin, which is a result of its charged nature and its strong hydrogen bonding [20]. The use of gelatin as a scaffold without functionalization, co-polymers, or

crosslinking is also considered to be ineffective in most cases and thusly the majority of research in biomedicine involves the use of one of these processes.

Despite gelatin's disputable uses as an electospun scaffold several studies have looked into utilizing a gelatin system or some derivative of it for cell and tissue regeneration studies. There has been a large pursuit of such applications in chondrocyte occupied tissues such as cartilage (*i.e.* articulating cartilage) and bone tissue [34, 144, 145]. These studies have demonstrated that gelatin when crosslinked with itself and/or with a co-polymer can act to greatly increase cartilage and bone tissue regeneration. It has also been shown from these studies that the fiber diameter and mechanical properties of gelatin can be easily manipulated by varying certain electrospinning parameters and the degree of crosslinking, respectfully. The ability to manipulate gelatin's properties makes it extremely useful as a scaffold component despite previous literature, which doubted its usefulness.

One physical parameter of electrospun gelatin matrices that has been studied in relation to its biological significance is the matrix porosity [146, 147]. It has been shown from this research as well as studies with other systems that matrix porosity is extremely important for cell in growth, differentiation and proliferation. Despite the research into interfiber porosity of gelatin scaffolds there has been very little to no known research into the effects of intrafiber porosity of the gelatin matrix fibers. This physical surface modification would be useful in increasing the surface roughness and thusly affecting quantities such as protein adhesion and wettability of the matrix. If the polymer matrix were a coaxial system then there would also be an increase in exposure of the inner core polymer to the environment, which could effect the properties of the system.

3. MATERIALS AND METHODS

3.1. MATERIALS

The materials used in fabricating chondoritin sulfate blend fibers were obtained from several varying sources. The sodium salt of hyaluronic acid was procured from Dali Hyaluronic Acid Co. (Liuzhou, Guangxi province, China). The poly (acrylic acid) powder (Mv $\sim$ 450,000), poly (ethylene oxide) powder (Mv $\sim$ 600,000), poly (allylamine) aqueous solution (20 wt %) (Mw $\sim$ 65,000), N-N-dimethylformamide (DMF) solvent and trifluoroacetic acid (TFA) solvent were acquired from Sigma-Aldrich ® (St. Louis, Missouri, USA). The chondroitin sulfate powder was procured from INDOFINE Chemical Company (Hillsborough, New Jersey, USA).

The materials used in synthesizing gelatin and collagen monoaxial and coaxial fibers of varying porosity were also obtained from a variety of sources. The gelatin, from porcine skin (type A), powder was procured from Sigma-Aldrich ® (St. Louis, Missouri, USA). The collagen, from bovine cartilage, powder was obtained from Kensey Nash Co. (Recently acquired by Royal DSM) (Exton, Pennsylvania, USA). The salts used to generate porosity, trisodium citrate and ACS reagent sodium chloride, as well as the solvent methyl ethyl ketone (MEK) were procured from Sigma-Aldrich ® (St. Louis, Missouri, USA). The piezoelectric core polymer poly (vinylidene fluoride - trifluoroethylene) was acquired from our research collaborators at Measurement Specialties^{TM} (Hampton, Virginia, USA). The solvent 1,1,1,3,3,3-hexafluoro-2-propanol (HFIP) was obtained from Oakland Chemicals Co.

The enzyme used for enzyme kinetic activity assays of the co-polymer chondroitin sulfate fibers, chondroitinase ABC from Proteus vulgaris and lysozyme were also procured from Sigma-Aldrich ® (St. Louis, Missouri, USA). All other solvents and/or materials were obtained from in lab synthesis (i.e. deionized water).

3.2. SOLUTION PREPARATION

3.2.1. HYALURONIC ACID AND CHONDROITIN SULFATE

Solutions consisting of hyaluronic acid (HA) and condroitin sulfate (ChS) were created in order to determine the fiber forming capacity of the anionic natural polymer HA for ChS. These solutions were made by adding 4 wt/v% HA to a 1:1 deionized water (DI):DMF solution in a 20mL glass sample vial. Following the addition of HA, 10 wt/v% ChS was then added to the same solution and the solution was vortexed on a Scientific Industries Inc. Vortex-Genie^{TM} (Bohemia, New York, USA) for approximately 15 min . The solution was stored on an Elmeco Engineering, Inc. Arma-Rotator A-1 (Rockville, Maryland, USA) for several days or until the solution was deemed to be homogeneous.

3.2.2. POLY (ACRYLIC ACID) AND CHONDROITIN SULFATE

Solutions consisting of poly (acrylic acid) (PAA) and ChS were formulated in order to determine the fiber forming capacity of the anionic synthetic polymer PAA for ChS. These solutions were synthesized by adding 5 wt/v% PAA to DI in a Falcon^{TM} 15mL conical centrifuge tube. This process was followed by immediately adding 10 wt/v% ChS to the same solution and then vortexing the solution on the Vortex-Genie^{TM} mentioned in previous solution preparations for approximately 15 min. The solution was then stored on the Arma-Rotator described previously for several days or until the solution was homogeneous.

3.2.3. POLY (ETHYLENE OXIDE) AND CHONDROITIN SULFATE

Poly (ethylene oxide) (PEO) and ChS solutions were prepared in order to characterize the fiber forming capacity of the neutral polymer PEO for ChS. Solutions containing this polymer blend were made by adding 5 wt/v% PEO to DI in a Falcon^{TM} 15mL conical centrifuge tube. The solution was then subjected to the same methods of mixing as previously described solutions including vortexing and time spent on a rotator until the solution was

deemed homogeneous.

3.2.4. POLY (ALLYLAMINE) AND CHONDROITIN SULFATE

Poly (allylamine) (PAAm) and ChS solutions were synthesized in order to characterize the fiber forming capacity of the cationic synthetic polymer (in neutral pH) PAAm for ChS. This solution was original attempted under purely aqueous conditions but due to its apparent ability to form a gelled polyelectrolytic complex at neutral pH the preparation had to be altered in order to reduce the dissimilar charge attraction. In order to accomplish this, the solution was acidified using TFA. The final solutions were synthesized by preparing a 1:1 TFA:(20 wt/v% PAAm in DI) solution in a 5mL Eppendorf Tube®. After the PAAm solution was acidified with TFA, 10 wt/v% ChS was added to the Eppendorf Tube® and the solution was vortexed for approximately 30-60 min. The solution was then allowed to rotate on the Arma-Rotator for 1-2 h prior to electrospinning.

3.2.5. GELATIN

Gelatin solutions were prepared with varying salt types, concentrations and sizes in order to control the degree of intrafiber porosity obtained *via* the salt leaching method. These solutions were synthesized by adding 7.5 wt/v% gelatin to HFIP in a Falcon™ 15mL conical centrifuge tube, vortexing and allowing the solution to homogenize on the rotator. Once homogeneous, 4 or 20 wt/v% of sodium chloride or sodium citrate would be added and allowed to disperse in solution for an average of three hours on the rotator. In order to reduce the salt size prior to addition, the salts would be mortar and pestled into a fine powder.

3.2.6. COLLAGEN

Collagen solutions were also prepared with varying salt types, concentrations and sizes in order to control the degree of intrafiber porosity obtained via the salt leaching method.

These solutions were synthesized similarly to gelatin by adding 7.5 wt/v% collagen to HFIP in a Falcon^{TM} 15mL conical centrifuge tube, vortexing and allowing the solution to homogenize on the rotator. Once homogeneous, 4 or 20 wt/v% of sodium chloride (NaCl) or sodium citrate ($Na_3C_6H_5O_7$) would be added and allowed to disperse in solution for an average of three hours on the rotator. In order to reduce the salt size prior to addition, the salts were ground into a fine powder using a mortar and pestle.

3.2.7. POLY (VINYLIDENE FLUORIDE TRIFLUOROETHYLENE)

Poly (vinylidene fluoride - trifluoroethylene) (PVDF-TrFE) solutions were synthesized in order to measure the effect intrafiber porosity of the shell polymer had on the overall piezoelectric response of the piezoelectric PVDF-TrFE core polymer in coaxial electrospun fibers. The solutions were prepared by adding 15 wt/v% of PVDF-TrFE to MEK in a Falcon^{TM} 15mL conical centrifuge tube. The solutions were then vortexed and allowed to homogenize on the Arma-Rotator.

3.3. SOLUTION CHARACTERIZATION

3.3.1. PH MEASUREMENT

In order to determine the pH for the various solutions, three pH measurements were recorded for each prepared solution. The testing was preformed using a Mettler-Toledo Delta 320 pH meter (Columbus, Ohio, USA) and the solutions were only measured after they had reached a homogeneous state and could be processed *via* electrospinning. Prior to taking measurements, the pH meter would be calibrated using a series of standard solutions.

3.3.2. CONDUCTIVITY

An Oakton CON 5110 conductivity meter (Vernon Hills, Illinois, USA) was utilized to probe the various solutions in order to determine their conductivities. PAH and ChS solutions which normally contained 50% TFA were diluted to 1% TFA in order to avoid

damaging the conductivity probe. Prior to taking measurements the conductivity meter would be calibrated using a series of standard solutions.

3.3.3. VISCOMETRY

The viscosities of all electrospun polymer solutions were determined by a size 7 Zeitfuchs® Cross-Arm Viscometer. A minimum of 1 mL of solution was required per measurement and a total of three measurements per solution were collected. The viscosity tests were conducted in a constant temperature bath maintained at room temperature (25 °C).

3.4. ELECTROSPINNING

3.4.1. MONOAXIAL ELECTROSPINNING

The monoaxial nanofiber mats were electrospun utilizing a set-up similar to the one shown in **figure 15**. The set-up was built in house and its major components consist of an acrylic Nalgene brand disposal and storage container housing (Thermo Fisher Scientific, Rochester, NY), a high-voltage power source (Gamma High Voltage Research Inc., Ormond Beach, FL), a syringe pump (Harvard Apparatus, Plymouth Meeting, PA) and a copper collecting plate wrapped in aluminum foil.

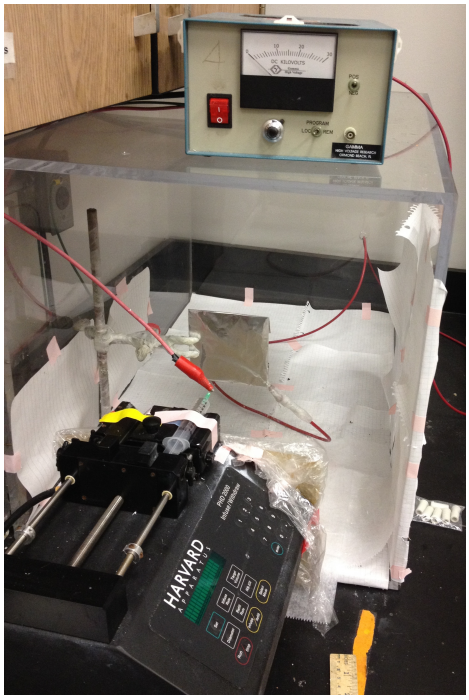

Figure 15: Monoaxial electrospinning set-up demonstarating the pump, collector, power source and acrylic housing

For most of the polymer solutions a 5 mL slip tip syringe (Becton Dickinson and Co., Franklin Lakes, NJ) was loaded manually by suctioning the solution through the syringe tip. For PAAm/ChS and HA/ChS solutions a 1 mL slip tip syringe (Becton Dickinson and Co., Franklin Lakes, NJ) was used instead due to its relative ease of loading and solution volume. A PrecisionGlide^{TM} 21-gauge needle (Becton Dickinson and Co, Franklin Lakes, NJ) would then be attached to the loaded syringes placed on the syringe pump. The syringe is directly attached to the positive electrode of the high-voltage power source *via* an alligator clip and the conductive collector would be connected to the negative electrode *via* another alligator clip. The distance from needle tip to collector, voltage, and pump rate would be varied dependent on the solution being electrospun (for exact values see **Table 2**). The relative humidity (%) and temperature (°C) of the lab during electrospinning was monitored by a digital thermohygrometer (Fisher Scientific, Pittsburgh, PA).

Any electrospun nanofiber mat prior to any further processing including crosslinking or salt leaching is considered and referred to as ”As Spun”.

Table 2: Monoaxial electrospinning set-up parameters per solution

Solution	Distance	Voltage	Pump Rate
PAA/ChS	15 cm	20 kV	0.8 ml/hr
PEO/ChS	15 cm	20 kV	0.8 ml/hr
PAAm/ChS	10 cm	15 kV	1.0 ml/hr
HA/ChS	18 cm	22 kV	60 μl/min
Gelatin (w or w/o salts)	12 cm	12 kV	1.0 ml/hr
Collagen (w or w/o salts)	12 cm	12 kV	1.0 ml/hr

3.4.2. COAXIAL ELECTROSPINNING

The coaxial electrospun nanofiber mats were electrospun utilizing a set-up similar to that shown in **figure 16**. The set-up is exactly the same as the monoaxial set-up described previously with the exception of the pump and the addition of a spinneret. The syringe pump utilized in the coaxial electrospinning set-up allowed for the operation of two syringes at two varying pump rates (Harvard Apparatus, Plymouth Meeting, PA). The spinneret utilized was made in house and consists of a dual capillary system, a shell polymer reservoir and a feed line into the capillary system from the shell polymer solution's syringe. For the coaxial polymer solutions a 5 mL slip tip syringe (Becton Dickinson and Co., Franklin Lakes, NJ) was loaded manually by suctioning the shell solution through the syringe tip. The core polymer solution was loaded into a 5 mL glass syringe *via* a similar method as the shell. The syringes were placed on the pump with the core syringe centered at a distance from the collector and the shell syringe placed in the remaining slot.

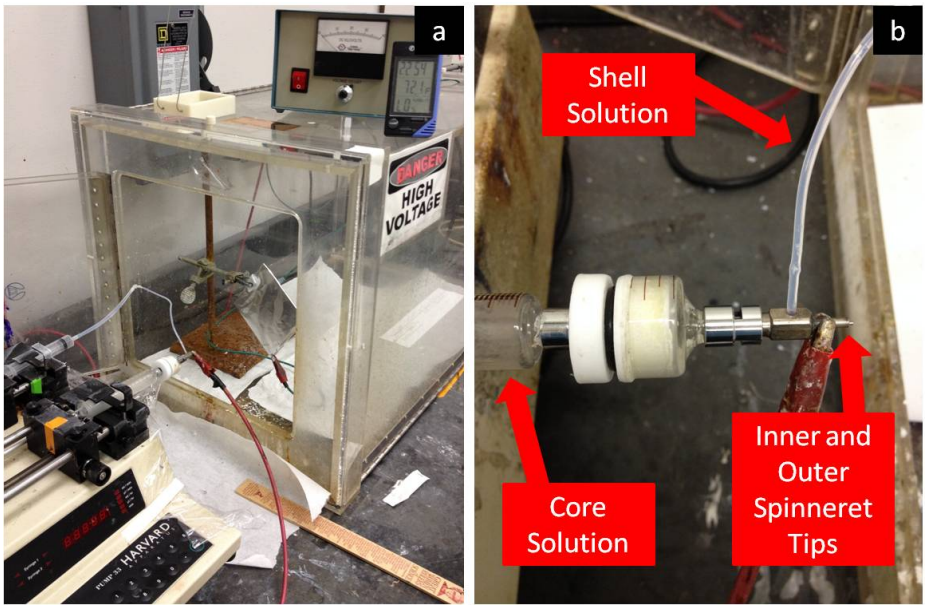

Figure 16: Coaxial electrospinning set-up demonstarating (a) the full set-up of the pump, collector, power source, acrylic housing and spinneret and (b) a close up of the coaxial spinneret

The inner capillary would be attached to the tip of the glass syringe and the feed line for the shell would be attached to the tip of the plastic syringe. The other end of the feed line would be inserted into the outer capillary/reservoir system and the outer capillary would be positioned around the inner capillary [**Figure 16b**]. The alligator clips would be attached in the same manner described in monoaxial electrospinning and the needle to collector distance would be set. The distance from needle tip to collector, voltage, and pump rate would be varied dependent on the solution being electrospun (for exact values see **Table 3**). The relative humidity (%) and temperature (°C) of the lab during electrospinning was monitored by a digital thermohygrometer (Fisher Scientific, Pittsburgh, PA).

Table 3: Coaxial electrospinning set-up parameters per solution

Solution	**Distance**	**Voltage**	**Pump Rate**
Gelatin (shell) (w or w/o salts)	12 cm	12 kV	1.0 ml/hr
Collagen (shell) (w or w/o salts)	12 cm	12 kV	1.0 ml/hr
PVDF-TrFE (core)	12 cm	12 kV	0.8 ml/hr

3.5. DEHYDROTHERMAL CROSSLINKING (DHT)

Prior to the leaching of deposited salts in water, the gelatin and collagen nanofibrous mats were crosslinked to increase their chemical stability. The crosslinks that form are covalent due to condensation reactions between carboxyl and amino groups when the water concentration falls below 0.2 g per100 g of protein [148, 149]. This method of crosslinking is preferential in biological applications due to the lack of residual cytotoxic molecules, which can be present in other methods of crosslinking. The samples were placed in a vacuum oven for 24 hours at 140 ± 2 °C.

3.6. SALT LEACHING

In order to generate intrafiber porosity, the collagen and gelatin samples needed to be immersed in a distilled water bath. The samples were immersed for time increments of 5 min in order to leach the salts while retaining the fibrous structure. The fibers after leaching were then analyzed for porosity and residual salts utilizing a scanning electron microscope (SEM) and an attached energy dispersive spectrometer (EDS).

3.7. OPTICAL MICROSCOPY

An Olympus PMG3 optical microscope was utilized in order to determine the presence of fibers after a sample had been electrospun and to determine the average particle size of ground or as received salt sources. If after electrospinning the fiber mat formed showed fibers under the optical microscope, then an SEM sample would be prepared for further analysis. For the salt analysis, a representative sample of the as received or mortar and pestled salt would be placed on a Corning glass microscope slide (Corning, NY, USA) and analyzed for average size via ImageJ image analysis software (National Institutes of Health, Bethesda, Maryland, USA).

3.8. SCANNING ELECTRON MICROSCOPY

A Zeiss Supra 50/VP field emission scanning electron microscope (FESEM) was utilized to image the morphology of all electrospun and post processed samples including as spun, DHT crosslinked and post leached. The majority of the images found throughout this thesis have been taken *via* this microscope. Before the FESEM images could be taken the fibrous mats had to be coated with platinum for 40 s *via* a Denton vacuum desk II sputtering machine.

3.8.1. ENERGY DISPERSIVE SPECTROSCOPY

The FESEM was equipped with an energy dispersive spectrometer, which was used to determine the sodium concentration and dispersion of sodium citrate and sodium chloride salts in gelatin and collagen samples. This analytical tool was also used to determine the concentration and dispersion of sulfate within the chondroitin sulfate polymer blend mats.

3.8.2. FIBER DIAMETER MEASUREMENTS

Fiber diameters and pore size were measured by taking a minimum of 50 measurements per FESEM image utilizing ImageJ software (National Institutes of Health, Bethesda, Maryland, USA). After the measurements had been recorded all statistics were analyzed *via* MATLAB® software (MathWorks, Natick, MA, USA).

3.9. FOURIER TRANSFORM INFRARED SPECTROSCOPY

The Fourier Transform Infrared Spectrometer (FTIR) used for sample analysis was a Thermo Nicolet Nexus 870 FT-IR Spectrometer. All samples were analyzed in transmission mode and their spectra were analyzed utilizing both the FTIR's associated software OMNIC® (Nicolet Instrument Corporation, Madison, WI, USA) and Origin software (OriginLab Corp., Northampton, MA, USA). Fibrous samples were cut from the mats

using a razor blade and placed on the FTIR stand. Bulk powders were also analyzed by placing a representative sample on the stand.

3.10. ENZYME KINETIC ACTIVITY

In order to determine if the carrier polymers of ChS would slow the enzyme catalyzed degradation of ChS, enzyme kinetic assays were conducted. For this assay the procedure conducted by *Pakulska et al* was modified, 10 μg of chondroitinase ABC (ChSase) was added to a 2 ml quartz cuvette along with 90 μl of 10 mg/ml of ChS. The absorbance at 232 nm of the double bond formed after chondroitinase ABC digests chondroitin sulfate was monitored and recorded every 60 s for 20 min [**Figure 17**] [150]. The absorbance was measured using an Ocean Optics USB2000 Miniature Fiber Optic UV-Vis spectrometer operating in the mid-UV range. The molar ratios of the solutions were used to estimate the ChS concentration per unit area of fibrous sample, which could then be used to determine the area of sample required in order to add 10 mg/ml to solution.

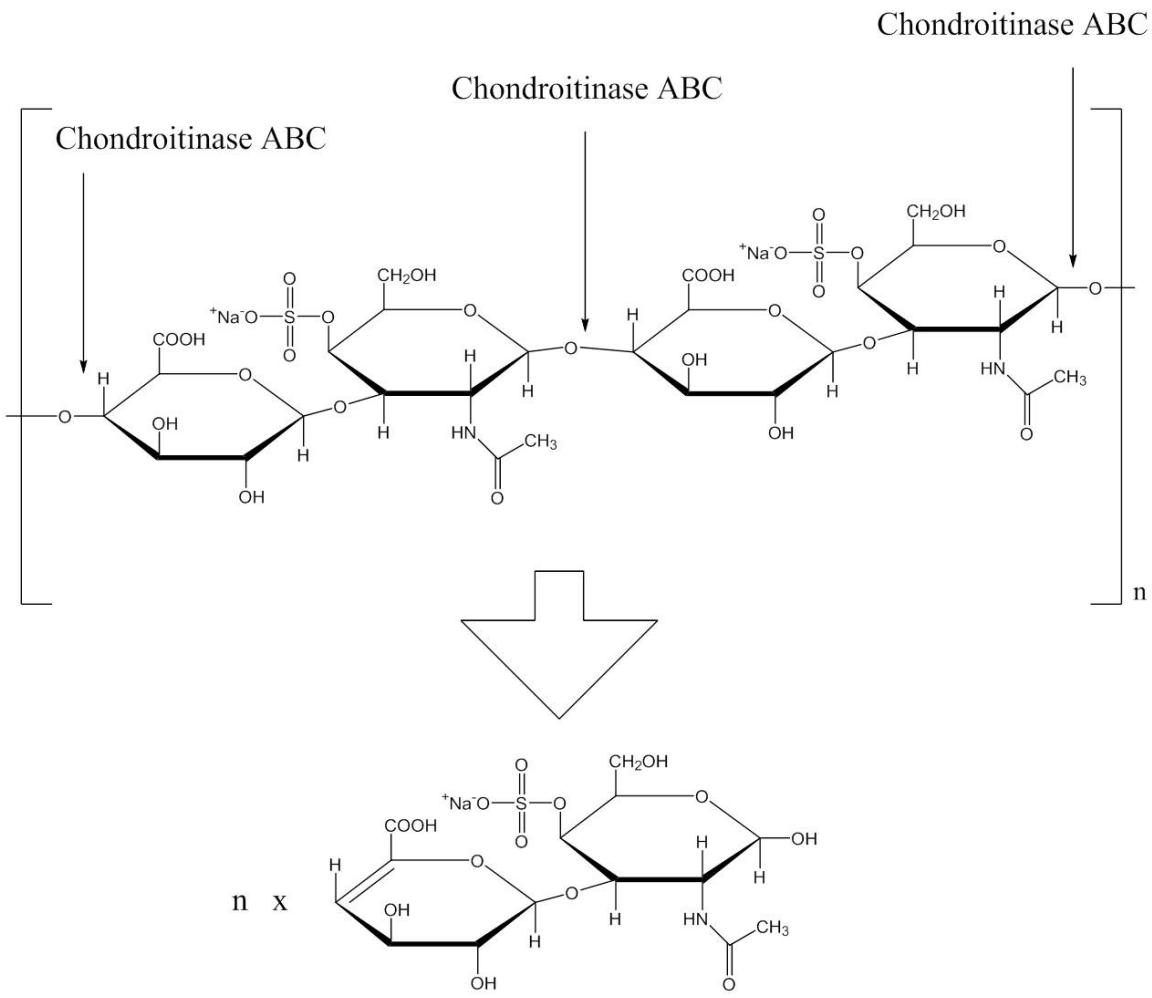

Figure 17: Basic diagram depicting the chondroitinase ABC digestion of ChS

4. SAFETY

4.1. PERSONAL PROTECTIVE EQUIPMENT

While in the laboratory, proper attire was worn. The general requirements consisted of long pants, closed toe footwear, a long white lab coat, wrap around safety glasses and nitrile or other chemically resistant gloves. The personal protective equipment (PPE) would change only when indicated by the material safety data sheet (MSDS) of the chemicals with which one was working, the protocols/standard operating procedures (SOPs) for the equipment one was using or when the situation required extra/additional PPE. Situations when extra PPE was required included working with strongly acidic or alkaline solvents such as HFIP.

4.2. MATERIAL SAFETY DATA SHEET AWARENESS

Prior to working with any chemicals the MSDS would be addressed in order to determine appropriate PPE requirements, storage and transfer requirements and specific hazards. Some of the solvents' MSDSs required extra precautions such as the use of butyl rubber gloves when transferring, the use of glass sample tubes instead of plastic and specific environments and materials to avoid. All solvents, with the exception of deionized water, were opened and transferred only within the well-ventilated chemical fume hood.

4.3. EQUIPMENT SAFETY

Prior to using equipment all available SOPs were read and all safety precautions were noted. Equipment such as the electrospinning set-ups have specific precautions to take note of including the use of high voltage DC power source (60 kV) which can generate significant amperage (600-750 A) and the potential for puncture wounds from syringe tips. Other equipment that was monitored and bared with signs when in use included the vacuum oven and atmospheric oven.

5. RESULTS AND DISCUSSION

5.1. COLLAGEN AND GELAIN INTRAFIBER POROSITY AND SALT INFILTRATION

5.1.1. MONOAXIAL GELATIN WITH SODIUM CHLORIDE

Gelatin-sodium chloride (GNaCl) solutions were investigated for their capacity to generate controllable, porous nanofibrous mats, which could be used as a control for further analysis with collagen. The gelatin polymer was dissolved in HFIP and the solution was then loaded with ground NaCl, where you could still visually observe crystals. HFIP was used in order to ensure that the NaCl salt would not dissolve in solution. After addition, the NaCl was visibly suspended and well dispersed in solution, which is important for salt infiltration and entrapment to occur. The salt concentration was varied between 4 wt/v% (GNaCl4) and 20 wt/v% (GNaCl20). The concentration was varied in order to determine if the salt infiltration and entrapment could be controlled by NaCl concentration in solution. Once the NaCl had been added to the 7.5 wt/v% gelatin solution, it was allowed to mix for 2-3 h on a rotator prior to electrospinning. Initial trials were also run with as received salts in order to determine if salt size had an effect on infiltration. The solutions were measured prior to electrospinning in order to determine pH, conductivity (change with respect to deionized water) and kinematic viscosity. These solution parameters can be found in **table 4**. The unusual nature of the conductivity spurred further analysis of the method of measurement and readings were taken for the various NaCl concentrations in water and HFIP. The three different solvent/solution systems were compared in **table 5**. It appears as though the conductivity of the salts in HFIP plateaus, which may play a role in explaining the behavior of the GNaCl solution conductivities. The increase in conductivity from 0 to 4 wt/v% NaCl is due to the very slight dissolution of salts, which can interact with the gelatin in solution. The salts dissolve to a greater extent in the presence of gelatin then in the HFIP solvent on its own, which may be attributable to availability of ionized groups

on the polypeptide. The conductivity increase may also be attributable to the salt acting as a dispersant in the gelatin solution. With no salts the gelatin may agglomerate due to the non-polar nature of the solvent HFIP. When the salts are added to solution the ionic interactions may act to disperse the polymer, this will both increase the conductivity and decrease the viscosity due to chain entanglement. As the NaCl concentration is drastically increased to 20 wt/v% the free ions in solution may start to form colloids which could fall out of solution. Once the colloids are formed the conductivity will tend to decrease and the dispersant effect would decrease. It is also important to note that the sample size is small and although the change in conductivity appears relatively large, the difference cannot be said to be statistically significant. Further study into this effect may be indicated.

Table 4: Gelatin with NaCl Solution Parameters

[NaCl]	**pH**	**Conductivity (μS)**	**Kinematic Viscosity (cSt)**
0 wt/v%	7.0	7.7	81.47
4 wt/v%	7.0	69.5	47.73
20 wt/v%	7.0	44.0	55.71

Table 5: Conductivity of various [NaCl] in water, HFIP and GNaCl

[NaCl]	**DI Water**	**HFIP**	**Gelatin**
0 wt/v%	12.8 μS	0.75 μS	7.7 μS
4 wt/v%	25.6 mS	1.12 μS	69.5 μS
20 wt/v%	93.6 mS	1.16 μS	44.0 μS

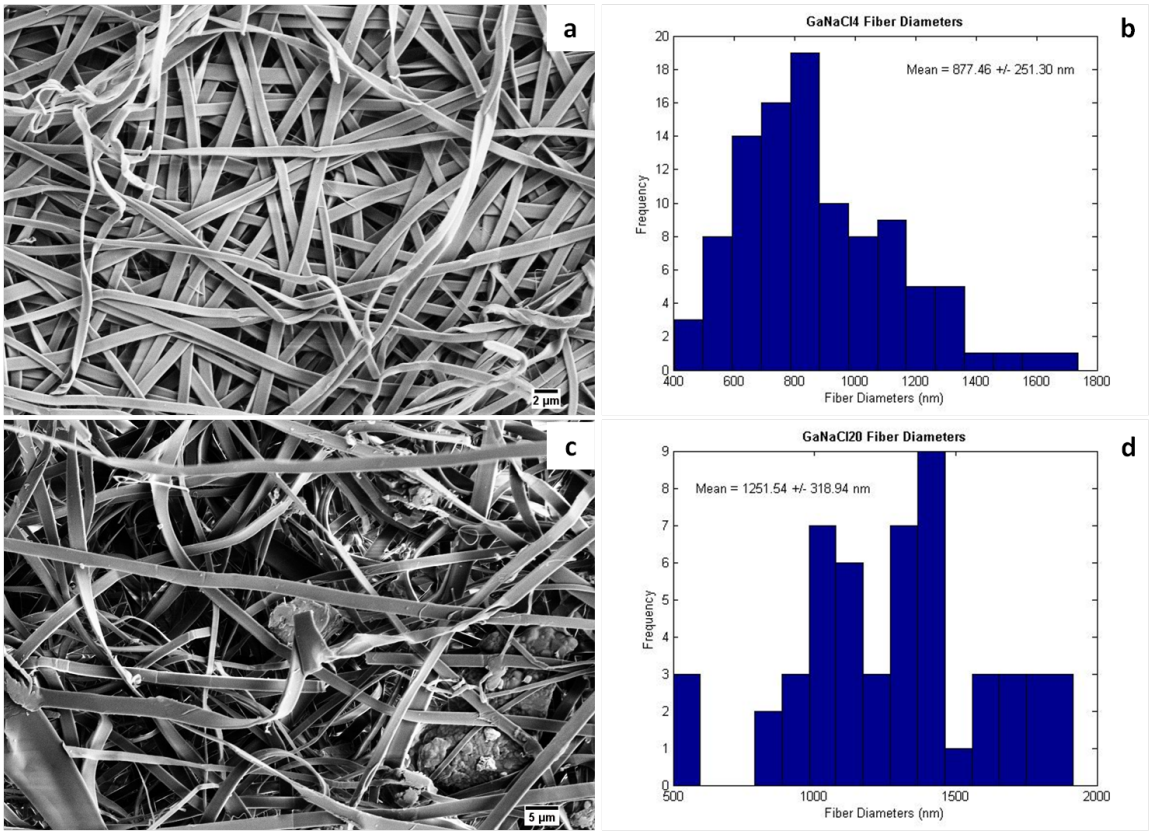

Figure 18: FESEM images and histograms of associated fiber diameters for gelatin nanofibers with (a and b) 4 wt/v% NaCl and (c and d) 20 wt/v% NaCl

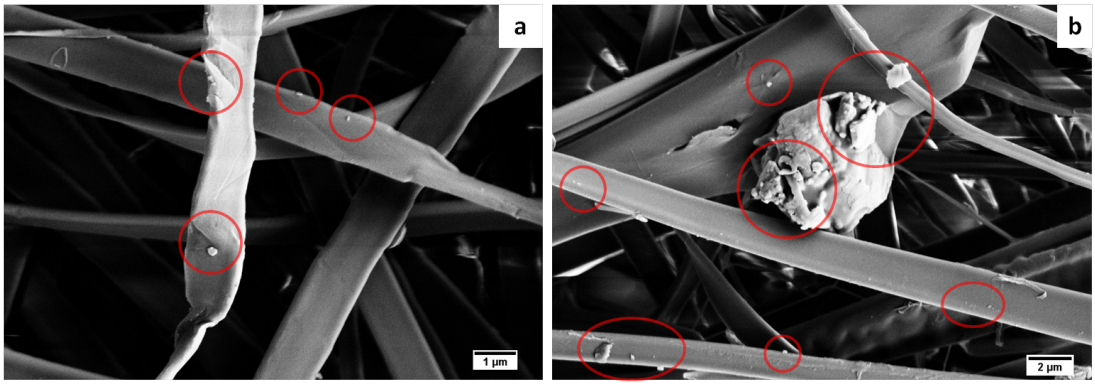

Figure 19: High magnification FESEM images of gelatin nanofibers with (a) 4 wt/v% and (b) 20 wt/v% NaCl with intrafiber salts circled in red

Table 6: Average diameters of the fibers formed from various GNaCl solutions

[NaCl]	Average Diameter (nm)	Standard Deviation (nm)
4 wt/v%	878	± 251
20 wt/v%	1252	± 319

Three solutions were electrospun under similar environmental conditions and utilizing the same electrospinning parameters. Once electrospun, the fibers' morphology and average fiber diameter were analyzed utilizing FESEM images. **Figure 18** demonstrates the morphology and size distributions of the GNaCl4 and GNaCl20 fibers. It can be seen from the FESEM images obtained, that GNaCl4 fibers demonstrate randomly aligned, continuous, ribbon like fiber morphologies with a very limited presence of NaCl salts. The salts appear to be sparse and poorly distributed in the GNaCl4 fibers but their presence can be better visualized under high magnification (intrafiber salts circled in red) [**Figure 19a**]. The size distribution of these fibers (n = 100) was mostly normal with a mean diameter residing at 878 nm (± 251 nm) as demonstrated by the histogram and **table 6**. The FESEM obtained for the GNaCl20 nanofibers demonstrate a similar morphology to that of the GNaCl4 fibers. The fibers exhibit a randomly aligned, continuous, ribbon like morphology with a very dense distribution of visible salts. The majority of the fibers in the FESEM image maintain several surface lying and subsurface intrafiber salts which can be visualized as lumps within or on the surface of the fibers. This image also demonstrates the ability for these fibers to entrap larger NaCl salts which can be visualized in the bottom right corner of **figure 18c**. The salt containing fibers can also be seen at higher magnification in **figure 19b**. In this image the intrafiber salts have been circled in red to better point out their location. It can be seen that these salts vary in size, orientation and degree of fiber infiltration which indicates a good distribution of salt in the matrix. The size distribution for these fibers (n = 50) appears to be a mostly normal distribution with a mean residing at 1252 nm (± 319 nm) [**Table 6**]. Although the average fiber diameters for both NaCl concentrations appear high in comparison to previous literature, this could be due to the increased con-

ductivity and viscosity of solutions [151, 152, 153]. The continuous ribbon morphology of the electrospun gelatin fibers has also been previously described in literature. What is novel about these fibers is the presence of intra- and interfiber salts. Salt infiltration has not previously been attempted or described in electrospun gelatin mats which leads to a lack of comparison to previous literature.

It was also of interest to investigate the effect that salt size may have on salt infiltration and entrapment. In order to investigate this effect, gelatin nanofibers were electrospun with as-received NaCl. These fibers yielded no visible indications of entrapped salts under FESEM analysis. The fibers did however exhibit a cylindrical morphology instead of the ribbon morphology witnessed in the fibers reported upon here. The lack of salts was in part, anticipated due to the average salt diameters of the as received salts residing around 5 μm. The ground salts average diameter was difficult to determine due to the limited magnification capacity of the optical microscope but the average was estimated to be less than 1 μm.

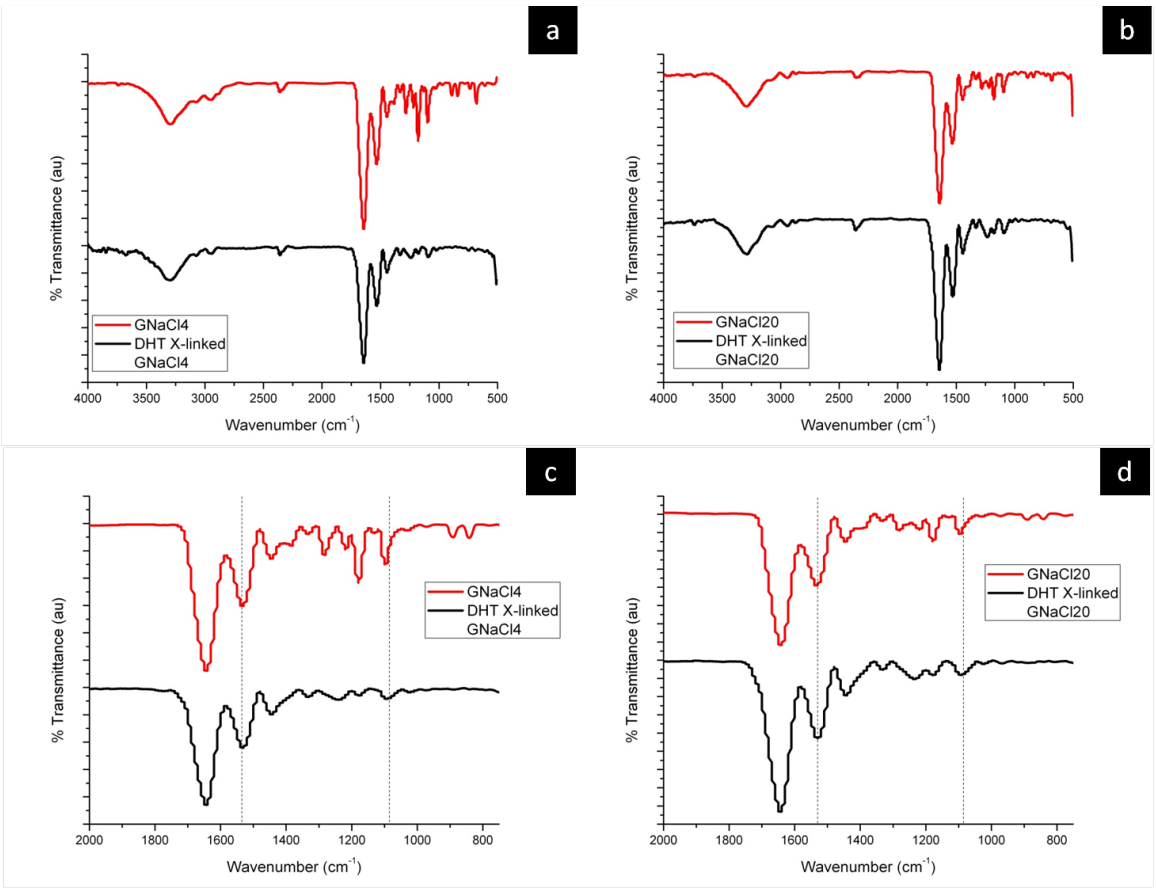

Figure 20: FTIR spectrographs of as spun and DHT crosslinked gelatin nanofibers with 4 wt/v% NaCl (a) at 500-4000 cm^{-1} & (c) 750-2000 cm^{-1} and 20 wt/v% NaCl (b) at 500-4000 cm^{-1} & (d) 750-2000 cm^{-1}

Table 7: GNaCl FTIR peaks of interest

Group	Mode	Peak Location (cm^{-1})
Amide II band (N-H)	Bending	1530-1550
Ester Bond (C-O)	Stretch	1090-1110

Prior to leaching out the infiltrating and fiber entrapped NaCl in deionized water, the GNaCl fibers needed to be crosslinked to increase their chemical stability. The fibers were analyzed by FTIR, DHT corsslinked and then analyzed again by FTIR to determine if the DHT process had been successful. **Figure 20** demonstrates the resulting FTIR spectra and the peaks of interest are listed in **table 7**. Increases in the intensity of both the amide peak at 1535 cm^{-1} and the ester peak at 1095 cm^{-1} would indicate that the DHT crosslinking

method was successful. Increases in these peaks would indicate that covalent crosslinks are forming at several potential residues in gelatin including: hydroxyproline (13.5%), glutamate (11.5%), arginine (8.8%), aspartate (6.7%), lysine (4.4%) and serine (4.25%) [154]. Although all of these residues, with the exception of hydroxyproline, are not components of the most common triplet of gelatin they make up a large percentage of the amino acids as indicated by the percentages listed with the amino acid. When analyzing these spectra it is hard to differentiate whether an increase has occurred after DHT treatment. These peaks appear to present slight increases but these increases in peak intensity could be attributable to an increased sample size which makes the difference inconclusive. Another interesting peak to point out is the weak shoulder peak just below 1400 cm^{-1} which disappears after DHT treatment. This peak is most likely attributable to the presence of residual HFIP which evaporates during the DHT processing.

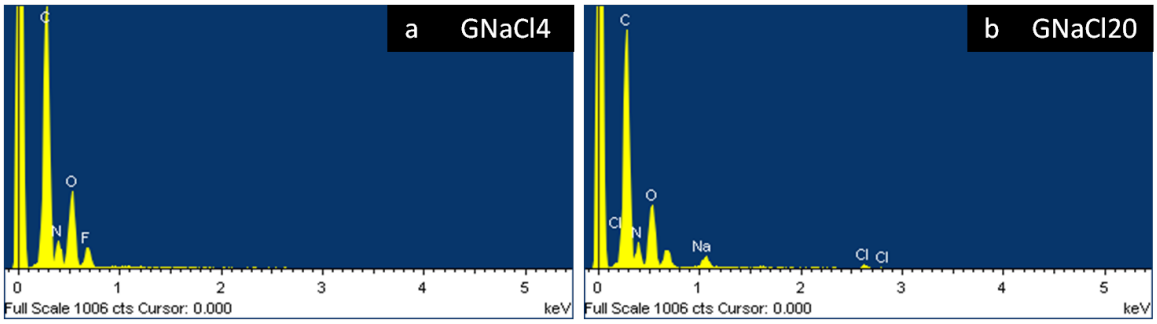

Figure 21: EDS spectrographs of as spun (a) gelatin nanofibers with 4 wt/v% and (b) 20 wt/v% sodium chloride

Table 8: The atomic and weight percents of specific elements in GNaCl fibers

	GNaCl4		**GNaCl20**	
Element	**Weight %**	**Atomic %**	**Weight %**	**Atomic %**
C	50.1	56.7	53.2	60.7
N	16.9	16.4	15.4	15.1
O	24.7	21.0	24.6	21.1
F	8.3	5.9	Undetected	Undetected
Na	Undetected	Undetected	2.4	1.4
Cl	Undetected	Undetected	4.5	1.7

In order to further determine the presence of NaCl in the GNaCl nanofibrous mats, the mats were analyzed utilizing EDS [**Figure 21**]. It can be seen from these spectra that the salt distribution observed in the FESEM images is reciprocated by the presence of a few highly apparent peaks. The GNaCl4 EDS spectra demonstrates no peaks which would indicate the presence of NaCl in the fiber mats. The spectra does however demonstrate the peaks for elements indicative of gelatin including carbon (C), oxygen (O) and nitrogen (N). Along with these peaks, the spectra also demonstrates a fluorine (F) peak which implies the presence of residual HFIP in the GNaCl4 fibrous mats [**Table 8**]. The second spectra located in **figure 21b** corresponds to the spectra obtained from GNaCl20 fibers. Again, this spectra demonstrates peaks indicative of gelatin and residual HFIP, although the fluorine peak indicating the presence of HFIP is not labeled it can be visualized around 0.7 keV. What is of primary interest in this spectra are the peaks for the elements sodium (Na) and chlorine (Cl) [**Table 8**]. The presence of these peaks indicates that the GNaCl20 fibers were electrospun with a relatively substantial amount of intrafiber and interfiber entrapped salts. Both of these spectra correlate back to what was visualized under FESEM.

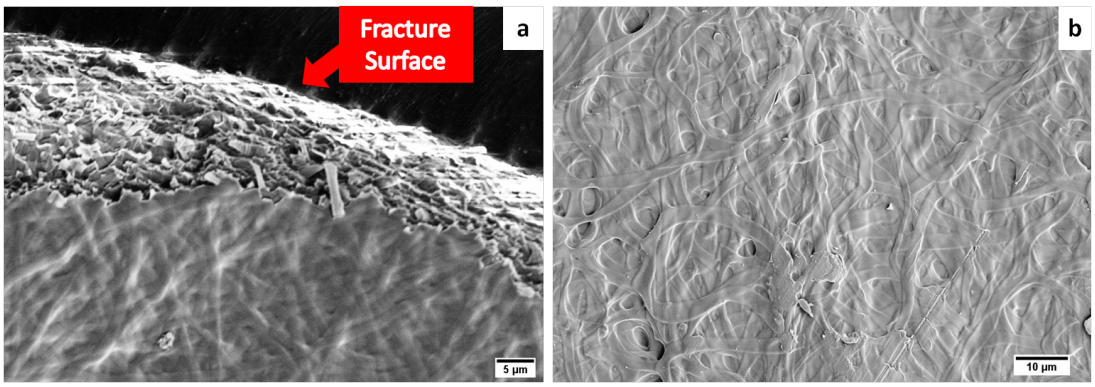

Figure 22: FESEM images of leached gelatin nanofibers with (a) 4 wt/v% and (b) 20 wt/v% NaCl

After the presence of salts was confirmed and the fibers had been DHT crosslinked the mats were placed in deionized water baths for 5 min in order to leach the salts while attempting to prevent fiber swelling and filming. After leaching, the fibers were placed on precut Teflon sheets and heated in the vacuum oven at 70 °C to remove residual water. In

order to confirm that the salts had been leached while retaining fibrous mats the leached mats were again imaged under FESEM. **Figure 22a** demonstrates the resulting mat for the GNaCl4 fibers which under close analysis seems to present with no residual salts. Unfortunately, the fibers also appear to have filmed after the leaching process preventing the formation of any intrafiber pores. Although the fibrous structure is still slightly visible on the surface and protruding out from the fracture surface at the top of the image, the fibers have lost most of their previous morphology. **Figure 22b** demonstrates the resulting mat for the GNaCl20 fibers. This fibrous mat appears to have retained some of its fibrous structure post leaching but there is significant, visible, swelling and filming. Overall, it can be seen that these fibers experienced some crosslinking although further crosslinking is indicated. It can also be seen, under close observation, that these fibers no longer present with a large dispersion of salts. This implies that the salts were effectively leached from the fibers but that the potentially generated pore structures were lost as a result of fiber filming and swelling. This may imply that the DHT crosslinking process utilized may have required more time or a higher temperature and that another method of crosslinking may need to be utilized in future work.

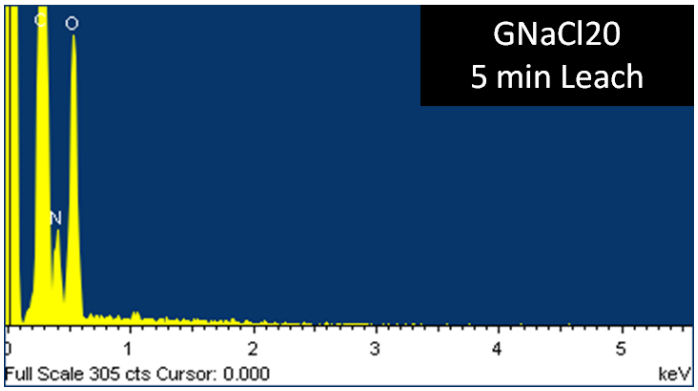

Figure 23: EDS of gelatin nanofibers with 20 wt/v% NaCl after leaching

Table 9: The atomic and weight percents of specific elements in leached GNaCl20 fibers

Leached GNaCl20		
Element	**Weight %**	**Atomic %**
C	55.3	61.0
N	15.9	15.1
O	28.8	23.9

Another method that was utilized to determine if the salts had been leached was post leaching EDS of sample that had previously demonstrated sodium peaks. Unfortunately, due to time and equipment constraints only one post leaching EDS was able to be obtained. **Figure 23** demonstrates the post leaching EDS for the GNaCl20 fibers previously analyzed under EDS [**Figure 21b**]. As can be seen form this spectra and from **table 9**, the previous peaks for sodium and chloride have been lost demonstrating that the salts have been leached from the fibers.

Overall, it appears as though the GNaCl4 fibers had entrapped NaCl within its fibers but to a much lesser degree then the GNaCl20 fibers. This result is expected and demonstrates the ability to control salt infiltration and entrapment by varying the solution concentration of NaCl. It is also apparent that the method of crosslinking may need to be altered in order to ensure the fibrous structure is retained within all of the mats. It should also be noted that the leaching process was successful at removing the NaCl from the fiber mats but due to the loss of fibrous structure did not generate the proposed porosity.

5.1.2. MONOAXIAL GELATIN WITH SODIUM CITRATE

Gelatin-sodium citrate (GNaCit) solutions were investigated for their capacity to generate controllable, porous nanofibrous mats, which could be used as a control for further analysis with collagen. The sodium citrate (NaCit) salt was also investigated in order to determine if salt type and complexity could be used to control salt infiltration. The gelatin polymer was dissolved in HFIP and the solution was then loaded with ground NaCit. HFIP was again used in order to ensure that the NaCit salt would only very slightly dissociate in

the solution. This very slight dissociation is due to the slight solubility of NaCit in HFIP, which does not occur with NaCl salts. After addition, the NaCit was visibly suspended and well dispersed in solution, which again, is important for salt infiltration and entrapment. The concentration of the salts was varied similarly to GNaCl solutions, with GNaCit solutions containing 4 wt/v% (GNaCit4) and 20wt/v% (GNaCit20). The concentration was varied in order to determine if the salt infiltration and entrapment could be controlled by NaCit concentration in solution. Once the NaCit had been added to the 7.5 wt/v% collagen solution, it was allowed to mix for 2-3 hours on a rotator prior to electrospinning. The solutions were measured prior to electrospinning in order to determine pH, conductivity (change with respect to deionized water) and kinematic viscosity. These solution parameters can be found in **table 10**. Trends in conductivity and viscosity of the GNaCit solutions, were similar to those observed in the GNaCl solutions. Again, this trend was compared to other solvent systems in order to assure the method of measurement was not flawed [**Table 11**]. A similar mechanism to that described previously, may very well play a role in these solutions as well.

Table 10: Gelatin with NaCitrate Solution Parameters

[NaCitrate]	**pH**	**Conductivity (μS)**	**Kinematic Viscosity (cSt)**
0 wt/v%	7.0	7.7	81.47
4 wt/v%	7.0	23.1	26.8
20 wt/v%	7.0	19.4	71.3

Table 11: Conductivity of various [NaCit] in water, HFIP and GNaCit

[NaCit]	**DI Water**	**HFIP**	**Gelatin**
0 wt/v%	12.8 μS	0.75 μS	7.7 μS
4 wt/v%	25.6 mS	1.06 μS	23.1 μS
20 wt/v%	93.6 mS	1.24 μS	19.4 μS

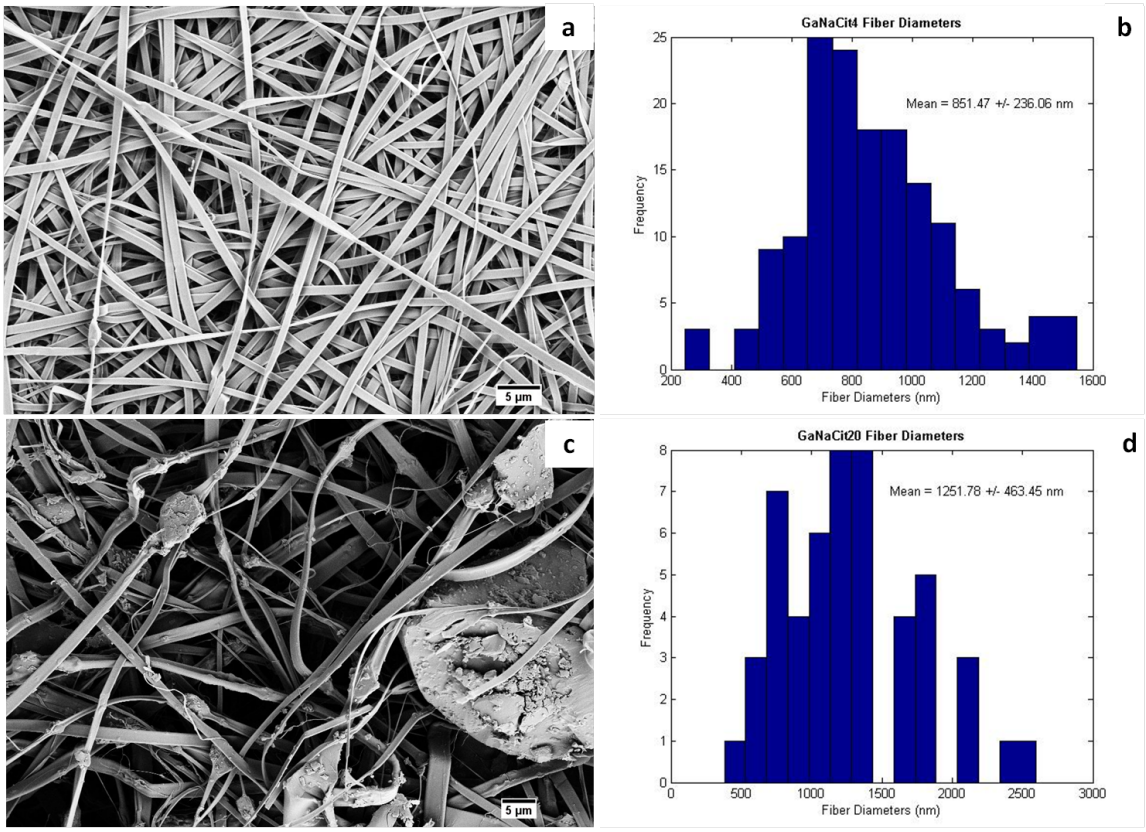

Figure 24: FESEM images and histograms of associated fiber diameters for gelatin nanofibers with (a and b) 4 wt/v% NaCit and (c and d) 20 wt/v% NaCit

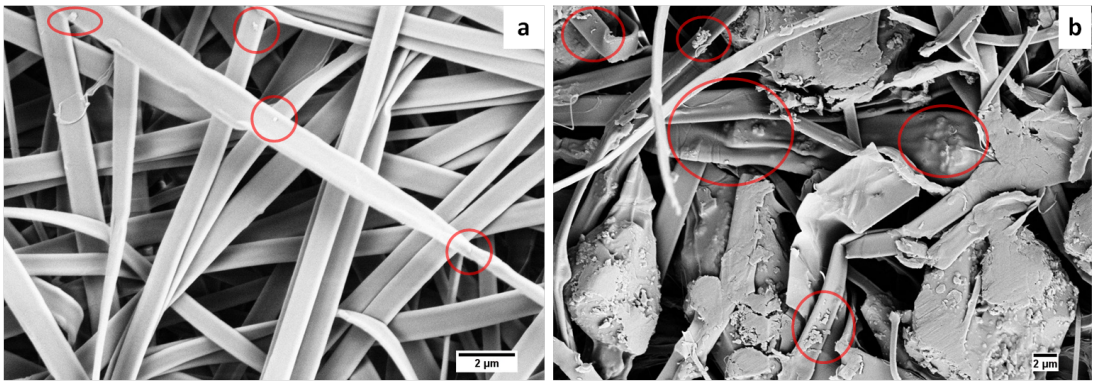

Figure 25: High magnification FESEM images of gelatin nanofibers with (a) 4 wt/v% and (b) 20 wt/v% NaCit with intrafiber salts circled in red

Table 12: Average diameters of the fibers formed from various GNaCit solutions

[NaCit]	Average Diameter (nm)	Standard Deviation (nm)
4 wt/v%	852	± 236
20 wt/v%	1252	± 464

Three solutions were electrospun under similar environmental conditions and utilizing the same electrospinning parameters. Once electrospun the fibers were analyzed for morphology and average fiber diameter utilizing FESEM images. **Figure 24** demonstrates the morphology and size distributions of the GNaCit4 and GNaCit20 fibers. It can be seen from the FESEM images obtained, that GNaCit4 fibers demonstrate randomly aligned, continuous, ribbon like fiber morphologies with a very limited presence of NaCl salts. This is very similar to what was previously observed with the GNaCl4 fibers. The salts are difficult to locate due to their sparsity in the GNaCit4 fibers but their presence can be seen under high magnification (intrafiber salts circled in red) [**Figure 25a**]. The size distribution of these fibers (n = 150) was mostly normal with a mean diameter residing at 852 nm (± 236 nm) as demonstrated by the histogram. The FESEM obtained for the GNaCit20 nanofibers demonstrates a morphology similar to that of all previously described gelatin samples but with a large resemblance to the GNaCl20 images. The fibers, again exhibit a randomly aligned, continuous, ribbon like morphology with a very dense distribution of visible salts. Similar to the GNaCl20 fibers, the majority of fibers in the GNaCit20 fibers exhibit several surface penetrating and subsurface intrafiber salts. This FESEM also indicates the ability for these fibers to entrap larger NaCit salts, which can be visualized throughout the sample but a very large salt is shown in the bottom right corner of **figure 24c**. At higher magnification the salt infiltration and entrapment can be better visualized [**Figure 25b**]. In this image the intrafiber salts have been circled in red to better indicate their location. It can be seen that these salts vary in size, orientation and degree of fiber infiltration which indicates that the NaCit salts are well distributed in the matrix. The size distribution for these fibers (n = 50) appears to be a mostly normal distribution with a mean residing at 1252 nm (±

464 nm). Although the average fiber diameters for both NaCit concentrations appear high in comparison to previous literature on electrospun gelatin, this could be due, in part, to the increased viscosity of solutions [151, 152, 153]. The ribbon morphology observed at both salt concentrations has also been previously described in literature regarding electrospun gelatin. Again, the novel component of these nanofibrous mats is the presence of intra- and interfiber salts. Salt infiltration has not previously been attempted or described in electrospun gelatin mats which leads to a lack of comparison to previous literature.

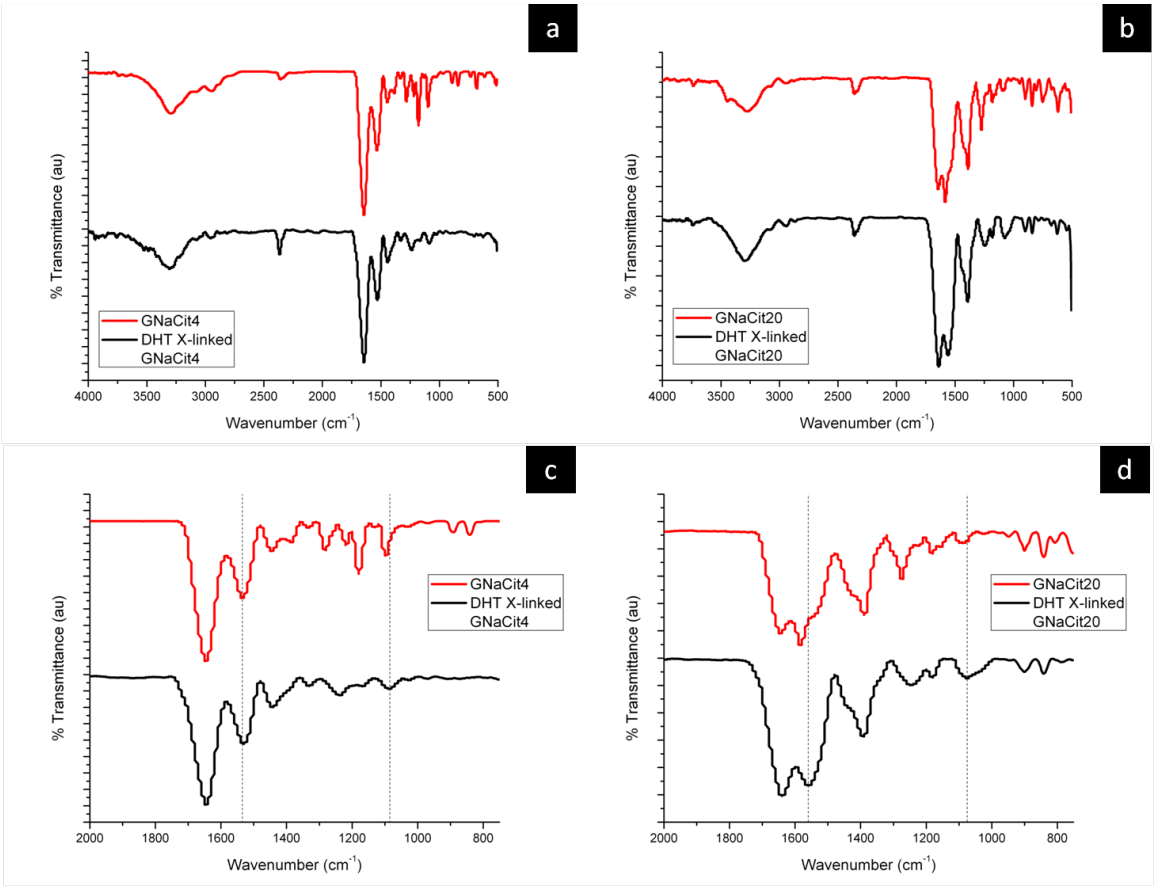

Figure 26: FTIR spectrographs of as spun and DHT crosslinked gelatin nanofibers with 4 wt/v% NaCit (a) at 500-4000 cm^{-1} & (c) 750-2000 cm^{-1} and 20 wt/v% NaCit (b) at 500-4000 cm^{-1} & (d) 750-2000 cm^{-1}

Table 13: GNaCit FTIR peaks of interest

Group	Mode	Peak Location (cm^{-1})
Amide II band (N-H)	Bending	1530-1550
Ester Bond (C-O)	Stretch	1090-1110

Prior to leaching out the infiltrating and fiber entrapped NaCit in deionized water, the GNaCit fibers needed to be crosslinked to increase their chemical stability. The fibers were analyzed by FTIR, DHT corsslinked and then analyzed again by FTIR to determine if the DHT process had been successful. **Figure 26** demonstrates the resulting FTIR spectra and the peaks of interest are listed in **table 13**. Similar to the GNaCl spectra, increases in the intensity of both the amide peak at 1535 cm^{-1} and the ester peak at 1095 cm^{-1} would indicate that the DHT crosslinking method was successful. Increases in these peaks would be attributable to covalent crosslinks forming at the residues previously described in the gelatin and NaCl analysis. When analyzing the GNaCit4 spectra it is hard to differentiate whether an increase has occurred after DHT treatment, similar to the GNaCl spectra. These peaks appear to present slight increases but these increases in peak intensity could be attributable to an increased sample size which again makes the difference inconclusive.

What is interesting in the GNaCit20 spectra is that the distinct amide I and amide II bands experience a significant decrease in intensity. This behavior has been described before when coupling gelatin to sodium citrate capped gold nanopraticles [155]. Previously, this behavior was attributed to the coordination of amide containing amino acid side chains with the sodium citrate capped gold nanoparticles. This however is unlikely due to the significant lack of amide containing amino acid side chains present in both gelatin and collagen (0.11%) [154]. The amide peaks observed in the FTIR spectra are instead attributed to the heterogeneity of neighboring peptide backbone carbonyl stretching modes [156]. When denatured, many of the amide groups hydrogen bond strongly to water and thus the bands increase in intensity due to increased heterogeneity of the associated backbone carbonyl stretching [156]. It is likely that the presence of sodium citrate acts to greatly reduce

the heterogeneity by hydrogen bonding to the carbonyl and potentially to the amide groups as well. When the concentration of sodium citrate is high enough to hydrogen bond a large portion of the peptide backbone, the hydrogen bonding is homogenized across the peptide as is the associated carbonyl stretching modes.

The significant reduction in the intensity of the amide bands allows for a greater visibility of both the amide II band and the ester band. This allows for the visualization of a significant increase in both bands after DHT crosslinking. These significant increases are indicative of the formation of covalent crosslinks but it is important to note that these increases could again be attributed to sample size differences. This however is unlikely due to the relatively large increases in intensity.

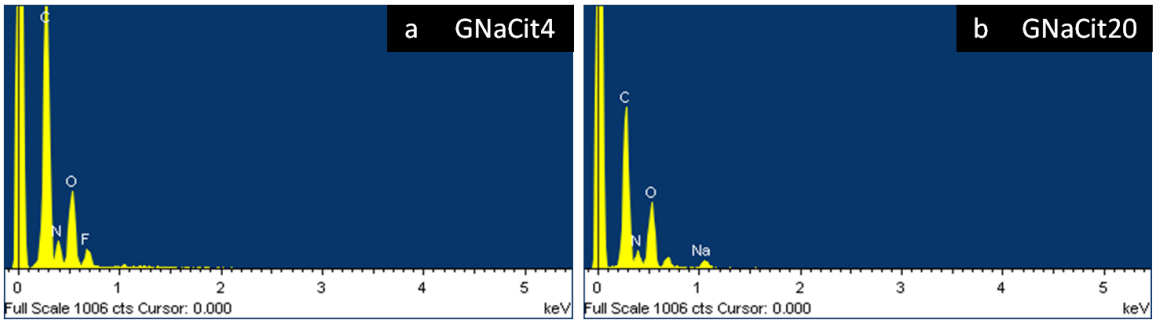

Figure 27: EDS spectrographs of as spun (a) gelatin nanofibers with 4 wt/v% and (b) 20 wt/v% sodium citrate

Table 14: The atomic and weight percents of specific elements in GNaCit fibers

	GNaCit4		**GNaCit20**	
Element	**Weight %**	**Atomic %**	**Weight %**	**Atomic %**
C	51.8	58.3	49.3	55.9
N	16.1	15.6	13.6	13.2
O	24.6	20.8	34.4	29.3
F	7.5	5.3	Undetected	Undetected
Na	Undetected	Undetected	2.7	1.6

Similarly to the GNaCl fibers, EDS was utilized to further indicate the presence of NaCit in the fibrous mats [**Figure 27**]. It can be seen from these spectra that the salt distribution observed in the FESEM images is again reciprocated by the presence of a

single pronounced peak. Similar to the GNaCl4 fiber spectra, the GNaCit4 EDS spectra demonstrates no peaks which would indicate the presence of NaCit in the fiber mats. There does exist a small jump from the baseline noise at around 1.05 keV but it is too small to implicit the presence of Na. The spectra does however demonstrate peaks for elements present in both citrate and gelatin including carbon (C), oxygen (O) and nitrogen (N). Along with these peaks, the spectra also demonstrates a fluorine (F), peak which implies the presence of residual HFIP in the GNaCit4 fibers [**Table 14**]. The second spectra located in **figure 27b** corresponds to the spectra obtained from GNaCit20 fibers. Again, this spectra demonstrates peaks indicative of gelatin and residual HFIP with an unlabeled but present fluorine peak. This spectra also demonstrates the presence of the single element of interest, Na, at around 1.05 keV. The presence of this peak indicates that the GNaCit20 fibers were electrospun with a relatively substantial amount of intrafiber and interfiber entrapped salts. Both of these spectra correlate back to what was visualized under FESEM.

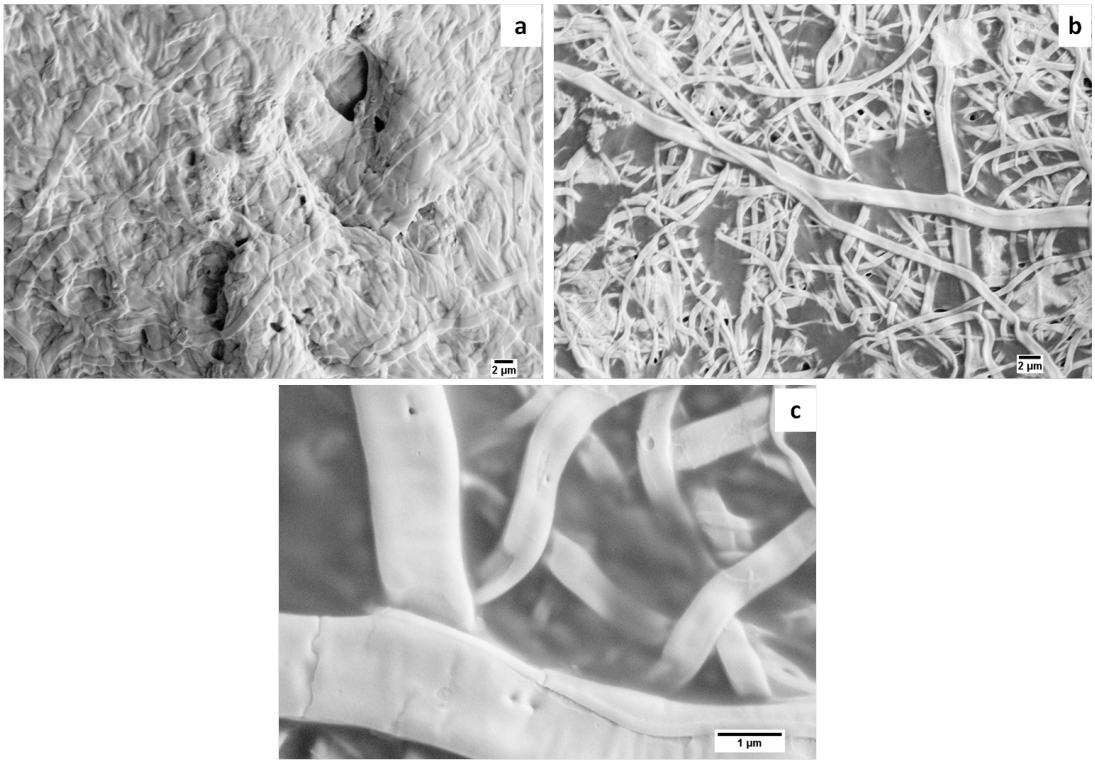

Figure 28: FESEM images of leached gelatin nanofibers with (a) 4 wt/v% and (b) 20 wt/v% NaCit and (c) high magnification FESEM of leached GNaCit20 fibers

After the presence of salts was confirmed and the fibers had been DHT crosslinked the mats were placed in deionized water baths for 5 min in order to leach the salts while attempting to prevent fiber swelling and filming. After leaching, the fibers were placed on precut Teflon sheets and heated in the vacuum oven at 70 °C to remove residual water. In order to confirm that the salts had been leached while retaining fibrous mats the leached mats were again imaged under FESEM. **Figure 28a** demonstrates the resulting mat for the GNaCit4 fibers which exhibit no apparent salts. The fibers here appear to have retained a large amount of their fibrous structure with some slight swelling and filming. The fibers, although still present, appear to have no apparent intrafiber pores but do present some pores which may be a result of dislocated interfiber salts. **Figure 28b** demonstrates the resulting mat for the GNaCit20 fibers. These fibers have again retained their fibrous structure with some fiber swelling and filming. As was seen with the GNaCit4 fibers, this fiber mat appears to exhibit large pores where interfiber salts may have been leached from. What is of extreme importance is that these fibers demonstrate intrafiber pores. These intrafiber pores are poorly dispersed but are very present and can be better visualized in **figure 28c**. These results indicate that the salt infiltration and subsequent leaching method is a viable option for generating controlled inter- and intrafiber pores. Although pores were observed, their size and distribution may have been effected by the partial swelling and filming of the fibers during leaching. This may indicate that the DHT crosslinking process could be improved by either increasing the time and/or temperature or by utilizing another method of crosslinking.

5.1.3. MONOAXIAL COLLAGEN WITH SODIUM CHLORIDE

Collagen-sodium chloride (CNaCl) solutions were investigated for their capacity to generate controllable, porous nanofibrous mats, which could potentially be used as cell scaffolds. The collagen polymer was dissolved in HFIP and the solution was then loaded with ground NaCl. HFIP was used, despite previous literature that demonstrated it dena-

tured collagen, in order to ensure that the NaCl salt would not dissociate in the solution. After addition, the NaCl was visibly suspended and well dispersed in solution. The concentration of the salts was varied with samples being electrospun from solutions containing 4 wt/v% (CNaCl4) and 20wt/v% (CNaCl20). The concentration was varied in order to determine if the salt infiltration and entrapment in collagen could be controlled by NaCl concentration in solution. Once the NaCl had been added to the 7.5 wt/v% collagen solution, it was allowed to mix for 2-3 hours on a rotator prior to electrospinning. The solutions were measured prior to electrospinning in order to determine pH, conductivity (change with respect to deionized water) and kinematic viscosity. These solution parameters can be found in **table 15**. The CNaCl solutions displayed a trend in conductivity which was unexpected. The CNaCl solutions were expected to behave similarly to the GNaCl solutions but instead there appears to be little to no significant effect on the solution parameters by adding salts. Again, in order to ensure the data was correct the conductivity was compared to other solvents with the fully or partially dissolved salts [**Table 16**]. The changes from 0 wt/v% NaCl to 4 wt/v% are relatively small and indicate no major interactions between the polypeptide and the salts. The changes seen when 20 wt/v% NaCl is added are attributed to the extreme variability of this extremely opaque suspension. Again, these differences cannot be stated to be statistically significant and these findings may be a result of sample randomness. As with gelatin these findings indicate further investigation.

Table 15: Collagen with NaCl Solution Parameters

[NaCl]	**pH**	**Conductivity (μS)**	**Kinematic Viscosity (cSt)**
0 wt/v%	7.0	87.6	33.0
4 wt/v%	7.0	80.7	30.7
20 wt/v%	7.0	55.3	38.3

Table 16: Conductivity of various [NaCl] in water, HFIP and CNaCl

[NaCl]	DI Water	HFIP	Collagen
0 wt/v%	12.8 μS	0.75 μS	87.6 μS
4 wt/v%	25.6 mS	1.12 μS	80.7 μS
20 wt/v%	93.6 mS	1.16 μS	55.3 μS

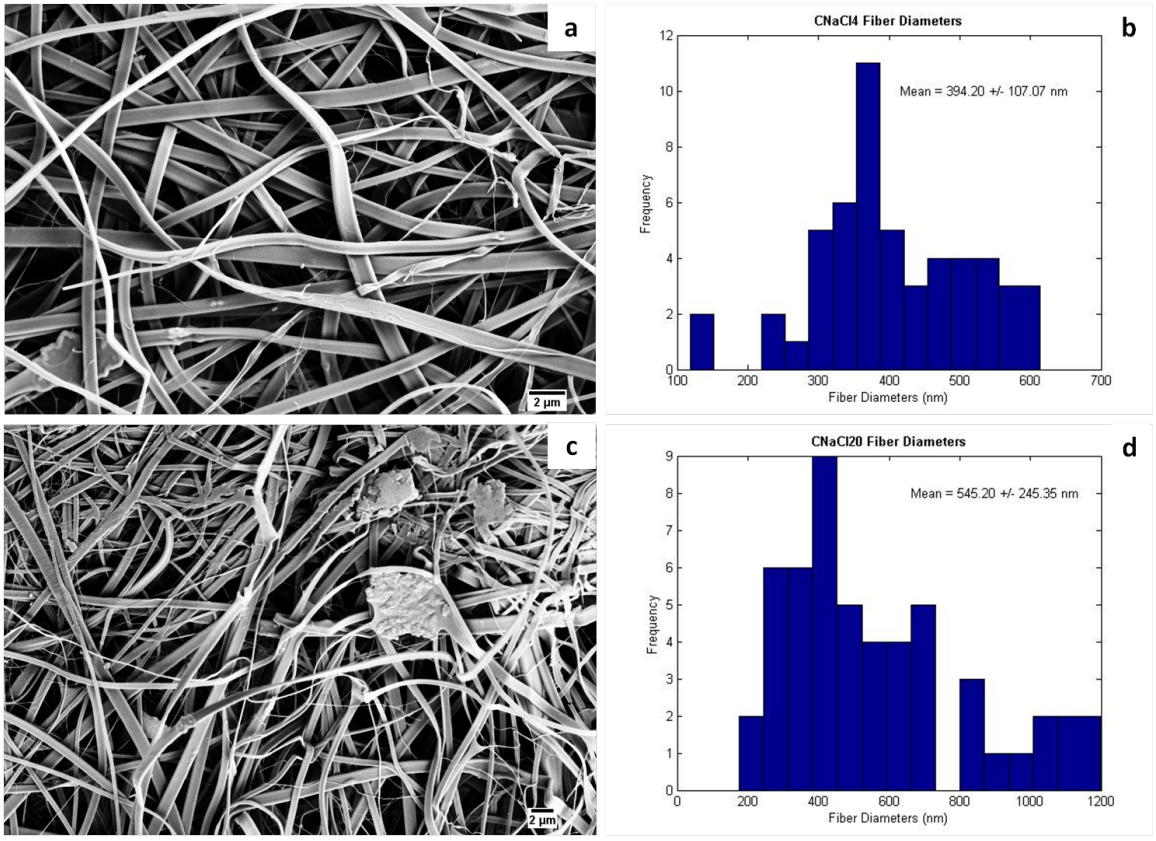

Figure 29: FESEM images and histograms of associated fiber diameters for collagen nanofibers with (a and b) 4 wt/v% NaCl and (c and d) 20 wt/v% NaCl

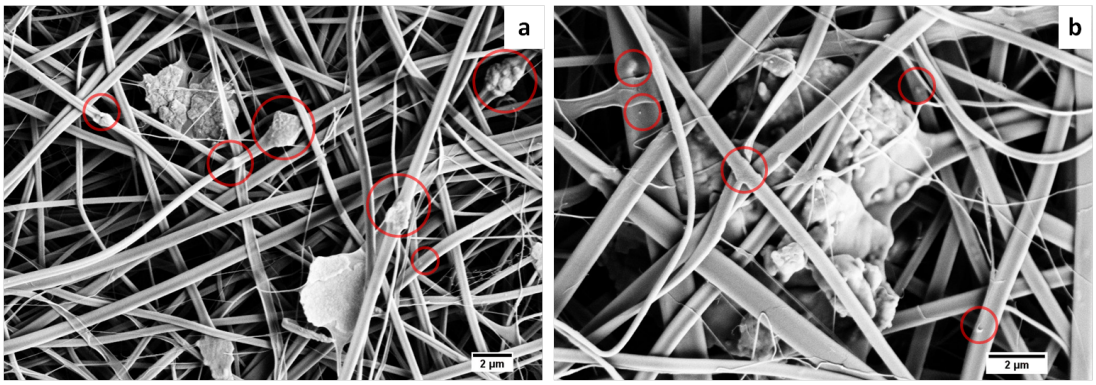

Figure 30: High magnification FESEM images of collagen nanofibers with (a) 4 wt/v% and (b) 20 wt/v% NaCl with intrafiber salts circled in red

Table 17: Average diameters of the fibers formed from various CNaCl solutions

[NaCl]	Average Diameter (nm)	Standard Deviation (nm)
4 wt/v%	384	± 107
20 wt/v%	545	± 245

Three solutions were electrospun under similar environmental conditions and utilizing the same electrospinning parameters. Once electrospun the fibers were analyzed for morphology and average fiber diameter utilizing FESEM images. **Figure 29** demonstrates the morphology and size distributions of the CNaCl4 and CNaCl20 fibers. It can be seen from the FESEM images obtained, that both the CNaCl4 and CNaCl20 fibers demonstrate randomly aligned, continuous, ribbon like fiber morphologies. The major difference is that the CNaCl4 fibers present with a reduced NaCl salt density in comparison to their heavily concentrated counterpart. This is very similar to what was previously observed with both the GNaCl and GNaCit fibers. A major difference here is that the CNaCl4 samples exhibit more obvious salts then their gelatin counterparts. The salts are still slightly difficult to locate due to their sparsity in the CNaCl4 fibers but this changes under high magnification (intrafiber salts circled in red) [**Figure 30a**]. The size distribution of these fibers (n = 50) was mostly normal with a mean diameter residing at 384 nm (± 107 nm) as demonstrated by the histogram. The FESEM obtained for the CNaCl20 nanofibers shows a very dense

distribution of visible salts. Similar to the the high concentration gelatin fibers, the majority of fibers in the sample exhibit several surface penetrating and subsurface intrafiber salts. One area of unique interest in this image is the vastly rough surface of a fiber in the top left corner which indicates a large presence of subsurface salts [**Figure 29c**]. This FE-SEM also indicates the ability for these fibers to entrap larger NaCl salts, which are highly visible in the top right corner of **figure 29c**. At higher magnification the salt infiltration and entrapment can be better visualized [**Figure 30b**]. In this image the intrafiber salts have been circled in red to better indicate their location. It can be seen that these salts vary in size, orientation and degree of fiber infiltration which indicates that the NaCl salts are well distributed in the matrix. The size distribution for these fibers (n = 50) appears to be a mostly normal distribution with a slight positive skew and a mean residing at 545 nm ($\pm$ 245 nm). The average fiber diameters for both NaCl concentrations appear typical and have been described previously in literature for electrospun collagen [137, 152, 157]. The ribbon morphology observed at both salt concentrations has also been previously described in literature involving electrospun collagen. Mineralization of collagen has been attempted previously which demonstrated entrapment and fiber surface roughening similar to what was observed [158]. It is important to note that the mineralization did not generate interfiber components as was observed in the CNaCl fibers.

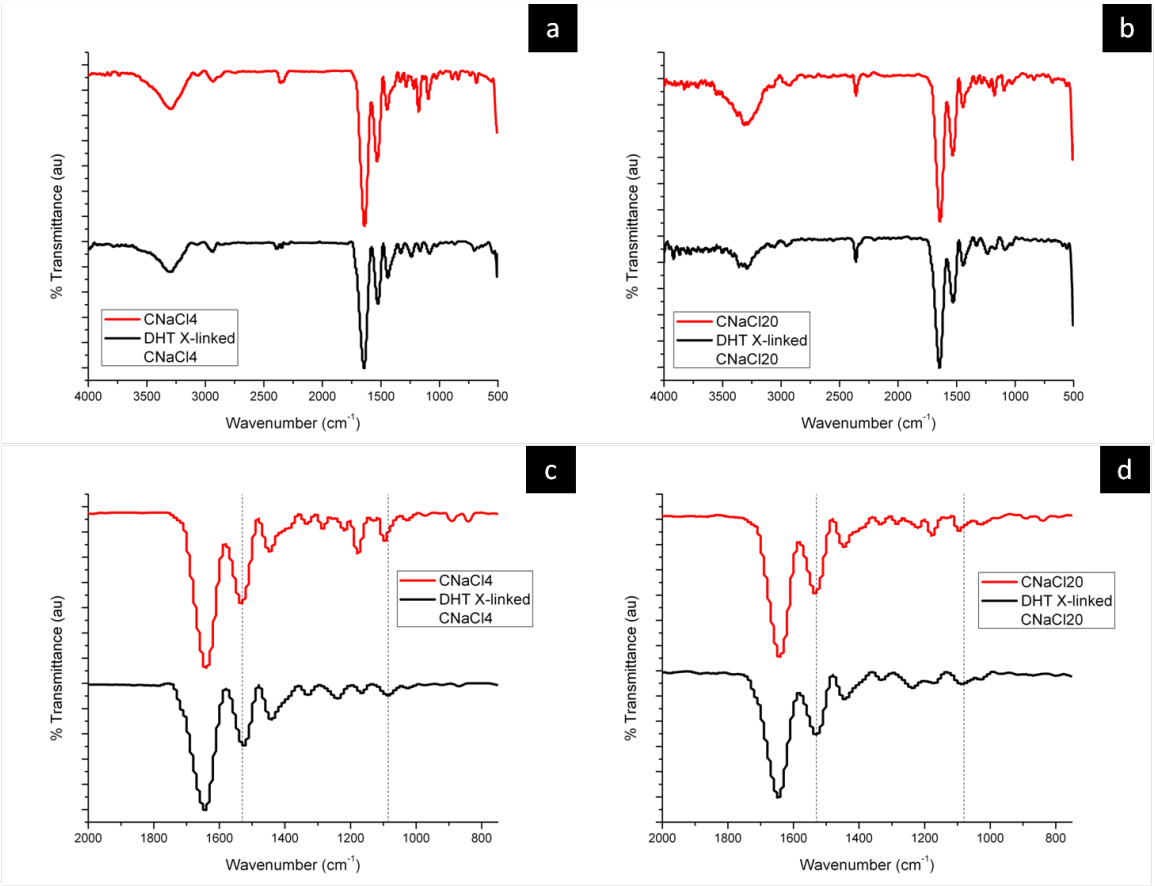

Figure 31: FTIR spectrographs of as spun and DHT crosslinked collagen nanofibers with 4 wt/v% NaCl (a) at 500-4000 cm^{-1} & (c) 750-2000 cm^{-1} and 20 wt/v% NaCl (b) at 500-4000 cm^{-1} & (d) 750-2000 cm^{-1}

Table 18: CNaCl FTIR peaks of interest

Group	Mode	Peak Location (cm^{-1})
Amide II band (N-H)	Bending	1530-1550
Ester Bond (C-O)	Stretch	1090-1110

Prior to leaching out the infiltrating and fiber entrapped NaCl in deionized water, the CNaCl fibers needed to be crosslinked to increase their chemical stability. The fibers were analyzed by FTIR, DHT corsslinked and then analyzed again by FTIR to determine if the DHT process had been successful. **Figure 31** demonstrates the resulting FTIR spectra and the peaks of interest are listed in **table 18**. Increases in the intensity of both the amide peak at 1535 cm^{-1} and the ester peak at 1095 cm^{-1} would indicate that the DHT crosslinking

method was successful. Increases in these peaks would indicate that covalent crosslinks are forming at several potential residues described previously in the gelatin-NaCl section. When analyzing these spectra it is hard to differentiate whether an increase has occurred after DHT treatment. These peaks appear to present slight-to-no increases but any changes in peak intensity could be attributable to a change in sample size, which makes the difference inconclusive. Another interesting peak to point out is the weak shoulder peak just below 1400 cm^{-1} which disappears after DHT treatment. This peak, as previously described, is most likely attributable to the presence of residual HFIP which evaporates during the DHT processing.

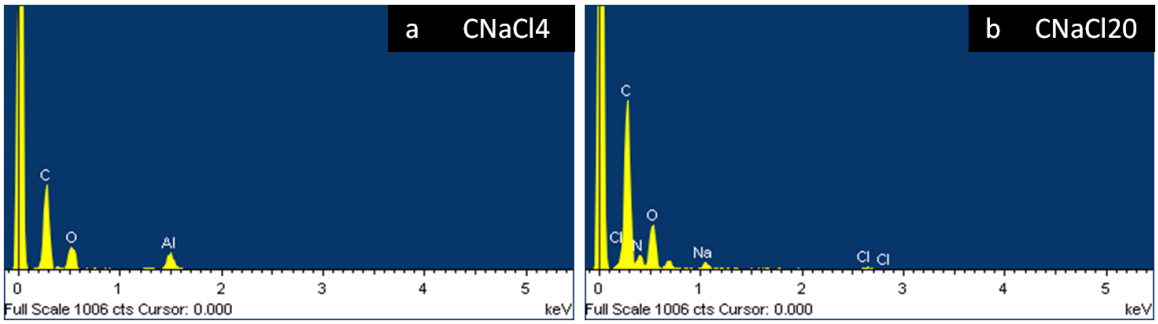

Figure 32: EDS spectrographs of as spun (a) collagen nanofibers with 4 wt/v% and (b) 20 wt/v% sodium chloride

Table 19: The atomic and weight percents of specific elements in CNaCl fibers

	CNaCl4		**CNaCl20**	
Element	**Weight %**	**Atomic %**	**Weight %**	**Atomic %**
C	59.1	69.9	55.8	63.6
N	Undetected	Undetected	12.3	12.1
O	23.5	20.9	24.5	21.0
Al	17.5	9.2	Undetected	Undetected
Na	Undetected	Undetected	2.3	1.4
Cl	Undetected	Undetected	5.0	2.0

In order to further determine the presence of NaCl in the CNaCl nanofibrous mats, the mats were analyzed utilizing EDS [**Figure 32**]. It can be seen from these spectra that the salt distribution observed in the FESEM images is supported by the presence of several

distinguishable peaks. The EDS spectra demonstrated in **figure 32** closely resemble the results obtained from the GNaCl fibers. This is expected and further demonstrates that the processes applied to gelatin can be expanded and utilized with its naive state, collagen. Similar to the GNaCl4 EDS spectra, the CNaCl4 EDS spectra demonstrates no peaks which would indicate the presence of NaCl in the fiber mats. The spectra does however demonstrate the peaks for elements indicative of gelatin including carbon (C), oxygen (O) and a small unlabeled peak for nitrogen (N). It is important to note the lack of a fluorine peak in this spectra which implies the concentration of residual HFIP is either very low or non existent. Also, the aluminum (Al) peak is most likely attributable to error in preparing the sample for EDS [**Table 19**]. Residual aluminum from the collector may have been removed along with the fibers after electrospinning. Also, the stubs used for EDS are made of aluminum and may be another potential source for this peak. The second spectra located in **figure 32b** corresponds to the spectra obtained from CNaCl20 fibers. Again, this spectra demonstrates peaks indicative of gelatin and residual HFIP, although the fluorine peak in this spectra is truncated in comparison to previously discussed EDS spectra. Again, this spectra demonstrates peaks for the elements of interest, sodium (Na) and chlorine (Cl) [**Table 19**]. The presence of these peaks indicates that the CNaCl20 fibers were electrospun with a relatively substantial amount of intrafiber and interfiber entrapped salts. Both of these spectra correlate back to what was visualized under FESEM.

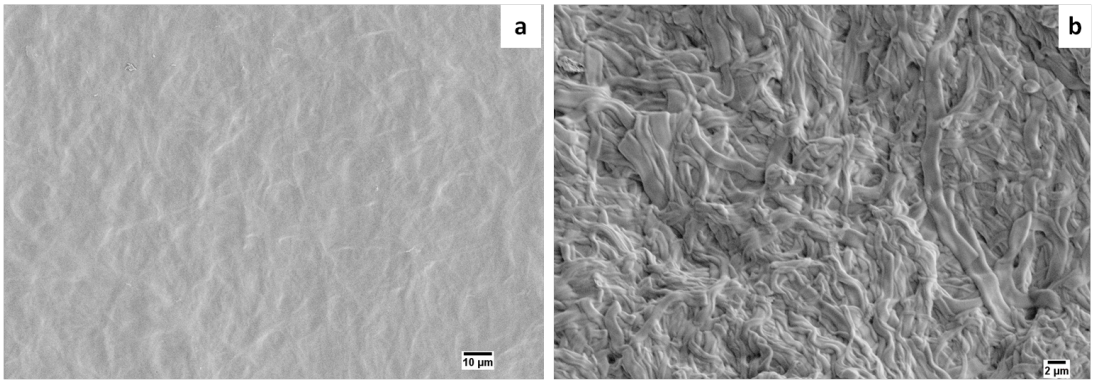

Figure 33: FESEM images of leached collagen nanofibers with (a) 4 wt/v% and (b) 20 wt/v% NaCl

After the presence of salts was confirmed and the fibers had been DHT crosslinked the mats were placed in deionized water baths for 5 min in order to leach the salts while attempting to prevent fiber swelling and filming. After leaching, the fibers were placed on precut Teflon sheets and heated in the vacuum oven at 70 °C to remove residual water. In order to confirm that the salts had been leached while retaining fibrous mats the leached mats were again imaged under FESEM. **Figure 33a** demonstrates the resulting mat for the CNaCl4 fibers. It appears as though these fibers were not sufficiently crosslinked and so all fibrous structure was lost during leaching. The fibrous structure is still very slightly visible on the surface but the mat overall can be considered to have filmed. **Figure 33b** demonstrates the resulting mat for the CNaCl20 fibers. This fibrous mat appears to have retained its structure post leaching with a small amount of visible swelling and filming. Overall, it can be seen that these fibers experienced some crosslinking although further crosslinking may be needed. It can also be seen, under close observation, that these fibers no longer present with a large dispersion of salts. This implies that the salts were effectively leached from the fibers but that the potentially generated pore structures were lost as a result of fiber filming and swelling. Again, these results imply that further investigation into the crosslinking methods of these fibers should be investigated.

5.1.4. MONOAXIAL COLLAGEN WITH SODIUM CITRATE

Collagen and sodium citrate (CNaCit) solutions were investigated for their capacity to generate controllable, porous nanofibrous mats, which could potentially be used as cell scaffolds. The NaCit salt was also investigated in order to determine if salt type and complexity could be used to control salt infiltration in collagen. The collagen polymer was dissolved in HFIP and the solution was then loaded with ground NaCit. HFIP was again used, despite previous literature that demonstrated it denatured collagen, in order to ensure that the NaCit salt would only very slightly dissociate in the solution. This very slight dissociation is due to the aforementioned slight solubility of NaCit in HFIP. After addition,

the NaCit was visibly suspended and well dispersed in solution. The concentration of the salts was varied similarly to CNaCl solutions with CNaCit solutions containing 4 wt/v% (CNaCl4) and 20wt/v% (CNaCl20). Once the NaCit had been added to the 7.5 wt/v% collagen solution, it was allowed to mix for 2-3 hours on a rotator prior to electrospinning. The solutions were measured prior to electrospinning in order to determine pH, conductivity (change with respect to deionized water) and kinematic viscosity. These solution parameters can be found in **table 20**. The same trends in conductivity that were seen in CNaCl solutions were observed in the CNaCit solutions. Once more these conductivities were compared to other solvent/solution systems [**Table 21**]. A similar mechanism to that described previously for the CNaCl solutions may very well be acting in these solutions as well.

Table 20: Collagen with NaCitrate Solution Parameters

[NaCitrate]	**pH**	**Conductivity (μS)**	**Kinematic Viscosity (cSt)**
0 wt/v%	7.0	87.6	33.0
4 wt/v%	7.0	65.1	28.2
20 wt/v%	7.0	60.9	32.0

Table 21: Conductivity of various [NaCit] in water, HFIP and CNaCit

[NaCit]	**DI Water**	**HFIP**	**Collagen**
0 wt/v%	12.8 μS	0.75 μS	87.6 μS
4 wt/v%	25.6 mS	1.06 μS	65.1 μS
20 wt/v%	93.6 mS	1.24 μS	60.9 μS

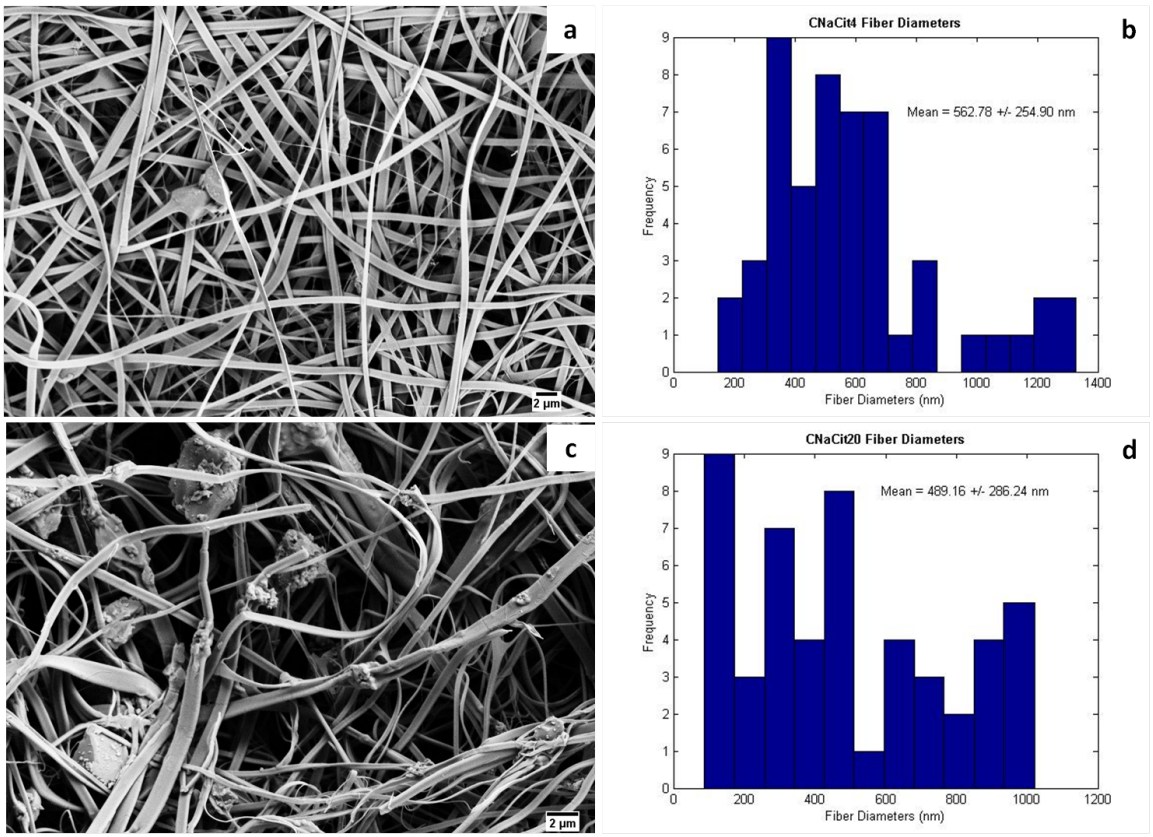

Figure 34: FESEM images and histograms of associated fiber diameters for collagen nanofibers with (a and b) 4 wt/v% NaCit and (c and d) 20 wt/v% NaCit

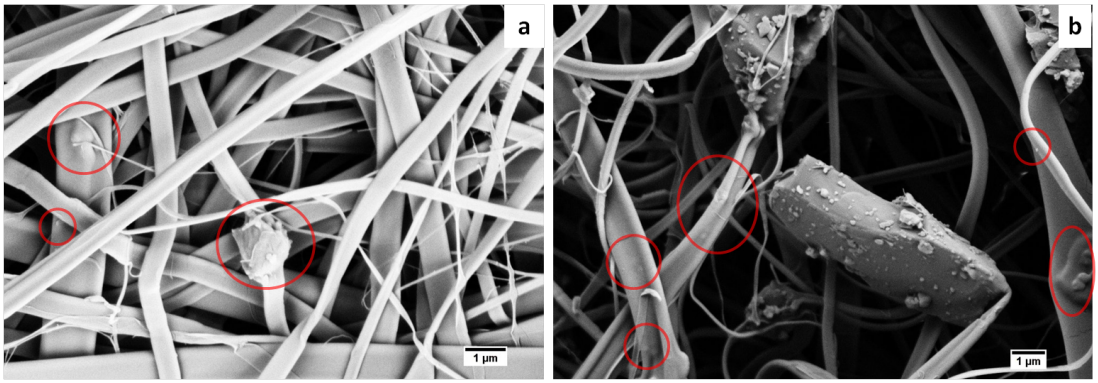

Figure 35: High magnification FESEM images of collagen nanofibers with (a) 4 wt/v% and (b) 20 wt/v% NaCit with intrafiber salts circled in red

Table 22: Average diameters of the fibers formed from various CNaCit solutions

[NaCit]	Average Diameter (nm)	Standard Deviation (nm)
4 wt/v%	563	± 255
20 wt/v%	489	± 286

Three solutions were electrospun under similar environmental conditions and utilizing the same electrospinning parameters. Once electrospun, the fibers' morphology and average fiber diameter were analyzed utilizing FESEM images. **Figure 34** demonstrates the morphology and size distributions of the CNaCit4 and CNaCit20 fibers. It can be seen from the FESEM images obtained, that both the CNaCit4 and CNaCit20 fibers demonstrate randomly aligned, continuous, ribbon like fiber morphologies. The major difference, as seen with the previous fibers, is that the CNaCit4 fibers present with a reduced NaCl salt density in comparison to their heavily concentrated counterpart. A feature that is again unique to the CNaCl4 and CNaCit4 samples is that they exhibit more obvious salts then their gelatin counterparts. It is still difficult to locate the salts due to their relative sparsity in the CNaCit4 fibers but this changes under high magnification (intrafiber salts circled in red) [**Figure 30a**]. These low concentration salt fibers demonstrate significantly larger areas of infiltration into the fibers then previous low concentration fibers. These fibers also exhibit a significant amount of subsurface salts in comparison to their gelatin counterparts. The size distribution of these fibers (n = 50) was mostly normal with a slight positive skew and a mean diameter residing at 563 nm (± 255 nm) as demonstrated by the histogram. The FESEM obtained for the CNaCit20 nanofibers shows a very dense distribution of visible intra- and interfiber salts. Similar to the previously described high concentration fibers, the majority of fibers in the sample exhibit several surface penetrating and subsurface intrafiber salts. The salts in these fibers are very visbile even a low magnification and appear to be well distributed throughout the imaged area [**Figure 29c**]. This FESEM also indicates the ability for these fibers to entrap larger interfiber NaCit salts, which are highly visible in the top and left corner of **figure 29c**. At higher magnification the salt infiltration and

entrapment can be better visualized [**Figure 30b**]. In this image, the intrafiber salts have been circled in red to better indicate their location. It can be seen that these salts vary in size, orientation and degree of fiber infiltration which indicates that the NaCit salts are well distributed in the matrix. The size distribution for these fibers (n = 50) appears to demonstrate either a J shaped distribution or a normal distribution with a large positive skew. The actual distribution could be better determined with a larger sample size. The mean diameter for this distribution resides at 489 nm ($\pm$ 286 nm). The average fiber diameters for both NaCit concentrations appear typical and have been described previously in literature [137, 152, 157]. The ribbon morphology observed at both salt concentrations has also been previously described in literature. Again, the novel component of these nanofibrous mats is the presence of intra- and interfiber salts. As stated previously, the closest comparison to this novel feature is the mineralization of collagen, which demonstrated entrapment and fiber surface roughening, but no interfiber entrapment [158].

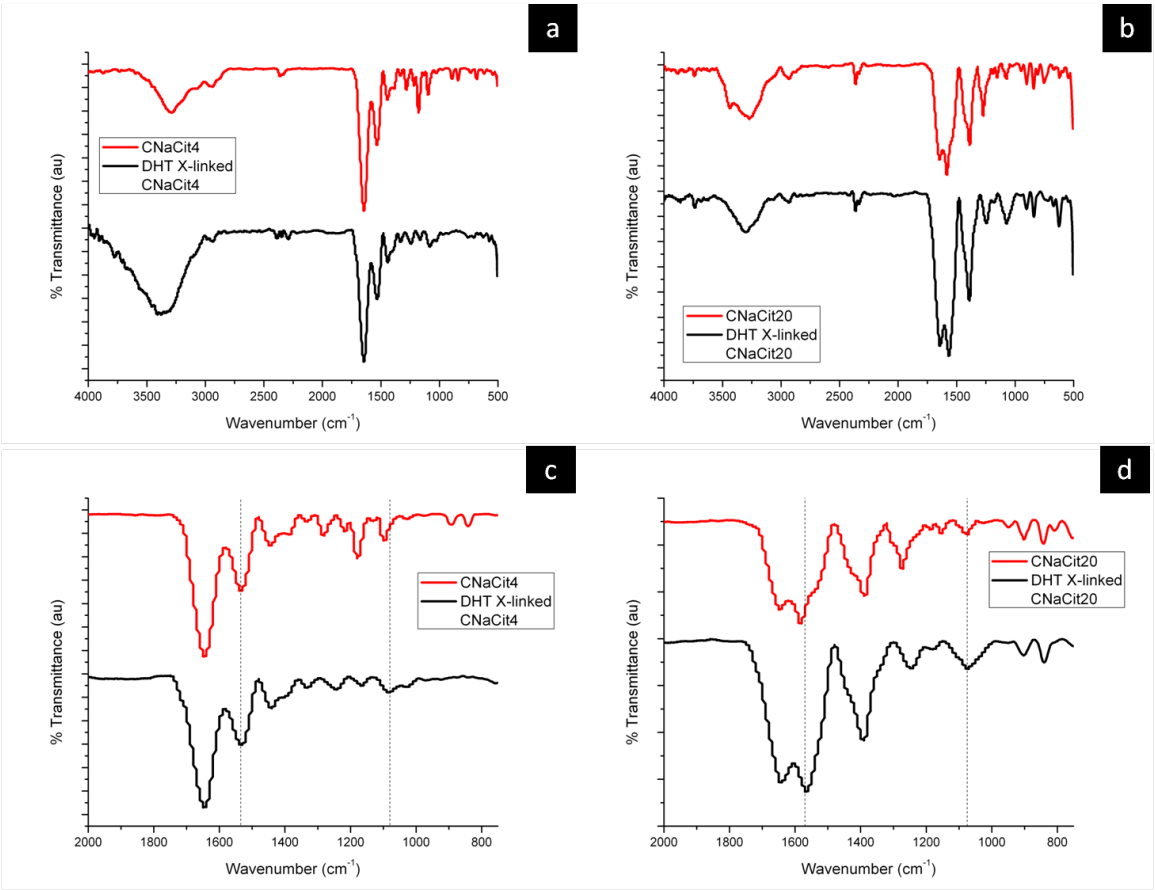

Figure 36: FTIR spectrographs of as spun and DHT crosslinked collagen nanofibers with 4 wt/v% NaCit (a) at 500-4000 cm^{-1} & (c) 750-2000 cm^{-1} and 20 wt/v% NaCit (b) at 500-4000 cm^{-1} & (d) 750-2000 cm^{-1}

Table 23: CNaCit FTIR peaks of interest

Group	Mode	Peak Location (cm^{-1})
Amide II band (N-H)	Bending	1530-1550
Ester Bond (C-O)	Stretch	1090-1110

Prior to leaching out the infiltrating and fiber entrapped NaCit in deionized water, the CNaCit fibers needed to be crosslinked to increase their chemical stability. The fibers were analyzed by FTIR, DHT corsslinked and then analyzed again by FTIR to determine if the DHT process had been successful. **Figure 36** demonstrates the resulting FTIR spectra and the peaks of interest are listed in **table 23**. Similar to the CNaCl spectra, increases in the intensity of both the amide peak at 1535 cm^{-1} and the ester peak at 1095 cm^{-1} would

indicate that the DHT crosslinking method was successful. Increases in these peaks would be attributable to covalent crosslinks forming at the residues previously described in the gelatin and NaCl analysis. When analyzing the CNaCit4 spectra it is hard to differentiate whether an increase has occurred after DHT treatment, similar to the CNaCl spectra. These peaks appear to present slight-to-no increases but any changes in peak intensity could be attributable to a change in sample size which again makes the difference inconclusive.

As was observed previously with the GNaCit20 spectra, the amide I and II bands (1635 cm^{-1} and 1550 cm^{-1}, respectively) were significantly reduced in the CNaCit20 spectra. This reduction has been described in depth in the gelatin NaCit spectra analysis but can be summarized as the reduction in heterogeneity of neighboring peptide backbone carbonyl stretching. This is, as stated previously, most likely a result of the homogenizing effect of sodium citrate hydrogen bonding uniformly across the peptide backbone. This reduction in the intensity of the amide bands allows for a greater visibility of the peaks of interest, the amide II band and the ester band. Increased visibility of these peaks permits for the observation of a significant increase in both bands after DHT crosslinking. These significant increases are indicative of the formation of covalent crosslinks but it is important to note that these increases could again be attributed to sample size differences. This however is unlikely due to the relatively large increases in intensity as well as the non-uniform increase in peaks across the spectra.

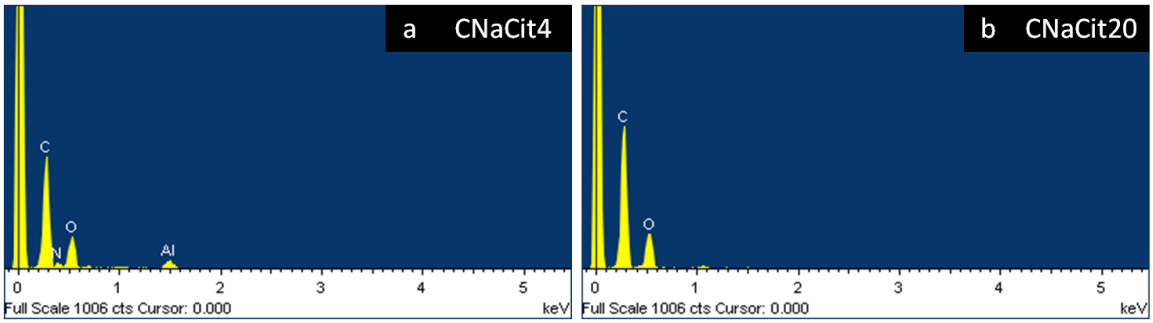

Figure 37: EDS spectrographs of as spun (a) collagen nanofibers with 4 wt/v% and (b) 20 wt/v% sodium citrate

Table 24: The atomic and weight percents of specific elements in CNaCit fibers

	CNaCit4		**CNaCit20**	
Element	**Weight %**	**Atomic %**	**Weight %**	**Atomic %**
C	54.9	63.7	69.4	75.1
N	7.8	7.7	Undetected	Undetected
O	26.3	22.9	30.6	24.9
Al	11.1	5.7	Undetected	Undetected

Similarly to all previously reported fibers, EDS was utilized to further indicate the presence of NaCit in the fibrous mats [**Figure 37**]. It can be seen from these spectra that the salt distribution observed in the FESEM images is again reciprocated by the presence of a single small peak and the absence of another peak. Similar to the GNaCit4 fiber spectra, the CNaCit4 EDS spectra demonstrates no peaks, which would indicate the presence of NaCit in the fiber mats. The spectra does however demonstrate peaks for elements present in both citrate and gelatin including carbon (C), oxygen (O) and nitrogen (N). The spectra also demonstrates sample preparation error with the existence of the Al peak [**Table 24**]. Similar to the CNaCl4 fibers, this spectra exhibits no fluorine peak, which may imply the concentration of residual HFIP is either low or non existent. The second spectra located in **figure 37b** corresponds to the spectra obtained from CNaCit20 fibers. Again, this spectra demonstrates peaks indicative of gelatin and citrate. One peak, that is missing, which may indicate a very high concentration of citrate at the sample surface is the N peak. The concentrations of C and O at the sample surface may over come any other peaks corresponding to elements at low concentrations. EDS is a surface technique and if citrate is very densely distributed at the surface where the fibers were analyzed, then peaks indicative of gelatin may be lost (N peaks in this case). This spectra also demonstrates the presence of a single, small, unlabeled peak indicating the presence of Na. The presence of this peak further implies that the analyzed surface was densely coated with NaCit. The presence of this peak and the absence of the N peak indicate that the CNaCit20 fibers were electrospun with a very substantial amount of intrafiber and interfiber entrapped salts. Both of these spectra

correlate back to what was visualized under FESEM.

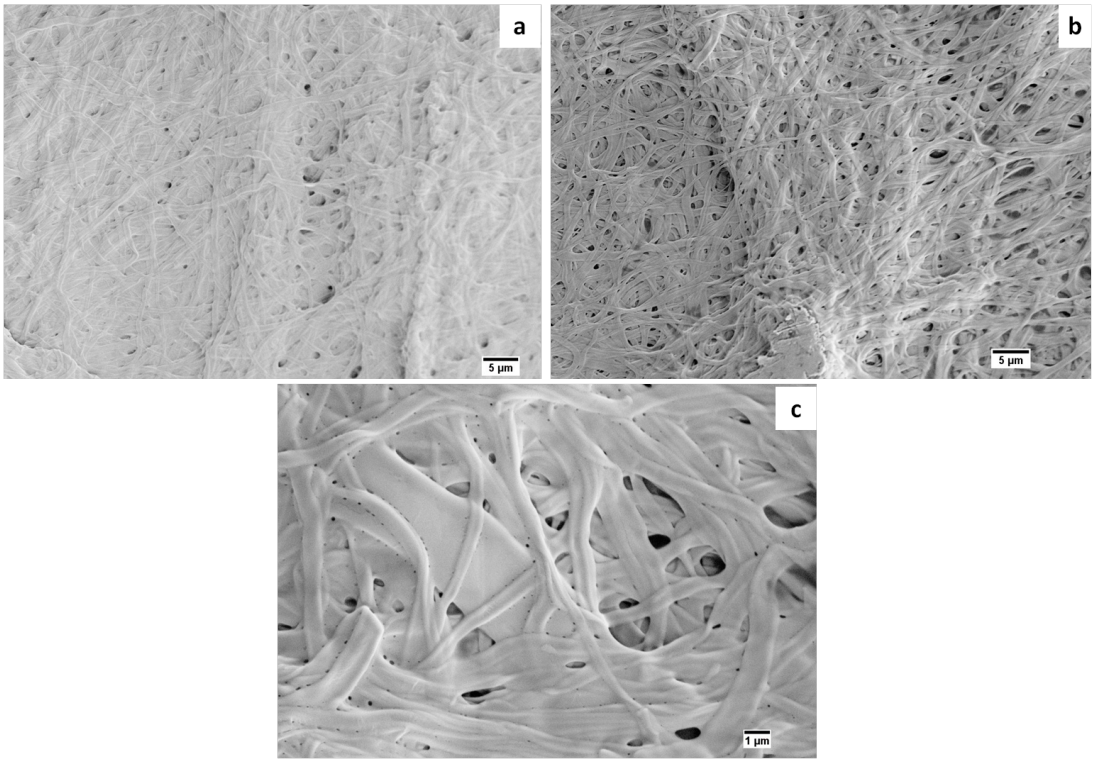

Figure 38: FESEM images of leached collagen nanofibers with (a) 4 wt/v% and (b) 20 wt/v% NaCit and (c) high magnification FESEM of leached CNaCit20 fibers

After the presence of salts was confirmed and the fibers had been DHT crosslinked the mats were placed in deionized water baths for 5 min in order to leach the salts while attempting to prevent fiber swelling and filming. After leaching, the fibers were placed on precut Teflon sheets and heated in the vacuum oven at 70 °C to remove residual water. In order to confirm that the salts had been leached while retaining fibrous mats the leached mats were again imaged under FESEM. **Figure 38a** demonstrates the resulting mat for the CNaCit4 fibers which exhibit no apparent salts. The fibers also appear to have retained a large amount of their fibrous structure with some slight swelling and filming. The fibers, although still present, appear to have no apparent intrafiber pores but do present some pores which may be a result of dislocated interfiber salts. These results are very similar to those of the leached GNaCit4 fiber mats. **Figure 38b** demonstrates the resulting mat for the CNaCit20 fibers. Again, the results here seem to exhibit behavior similar to the leached

GNaCit20. These fibers have retained their fibrous structure with some fiber swelling and filming. As was seen with all previously reported leached, NaCit containing fibers, this fiber mat appears to exhibit large pores where interfiber salts may have been leached from. These fibers, as was seen with the GNaCit20 fibers, demonstrate intrafiber pores. These intrafiber pores are not only present but also well dispersed and were found all over this sample. They are hard to visualize under low magnification and can be better visualized in the high magnification FESEM image, **figure 28c**. These results indicate that the salt infiltration and subsequent leaching method is a viable option for generating controlled inter- and intrafiber pores. Although pores were observed, their size and distribution may have been effected by the partial swelling and filming of the fibers during leaching. This may indicate that the DHT crosslinking process could be improved by either increasing the time and/or temperature or by utilizing another method of crosslinking.

5.1.5. COAXIAL PVDF-TrFE AND GELATIN WITH SODIUM CHLORIDE

After analysis and determination of the methods suitable to generate intra- and inter-fiber salts in monoaxial electrospun gelatin and collagen fibers, the methods which obtained the highest degree of salt infiltration were applied to coaxial electrospun fibers. A single polymer, salt and concentration were selected based on prior results. Monoaxial gelatin nanofibers with 20 wt/v% NaCl demonstrated the largest most distinguishable salt densities according to FESEM and EDS results. The positive results shown in monoaxial fibers led to its choice as the shell solution for the coaxially electrospun PVDF-TrFE core fibers. Again, the goal of this continuation to coaxial fibers is to determine the capacity of these method to generate controllable, porous, piezoelectric nanofibrous mats which can be applied to further investigations in cell nanogenerators and sensors. The gelatin polymer was dissolved in HFIP and the solution was then loaded with ground NaCl at 20 wt/v%. After addition, the NaCl was visibly suspended and well dispersed in solution, which had been deemed important with the monoaxial fibers. The PVDF-TrFE was dissolved in MEK at

15 wt/v% prior to the addition of NaCl to the gelatin solution in order to give it sufficient time to homogenize. The GNaCl20 solution was allowed to mix for 2-3 hours on a rotator prior to coaxial electrospinning.

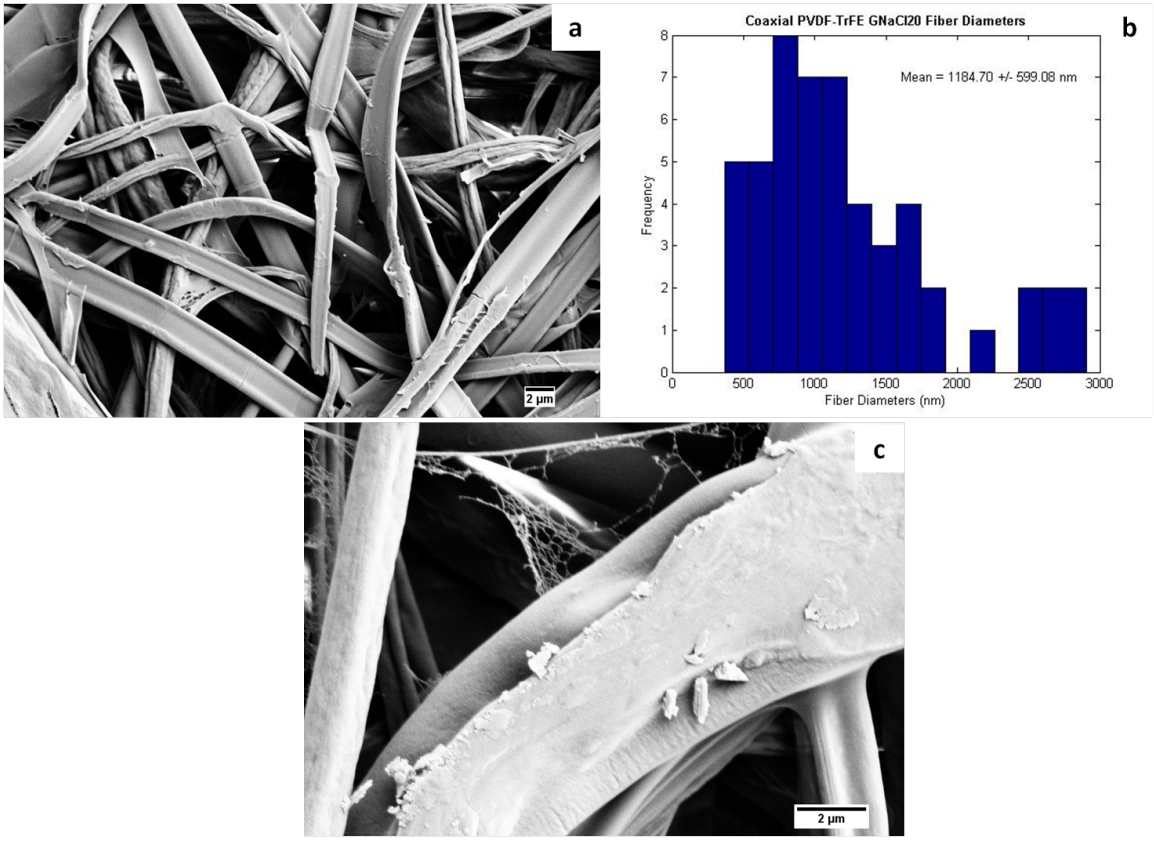

Figure 39: (a and b) FESEM image and histogram of associated fiber diameters for coaxial PVDF-TrFE core/GNaCl20 shell nanofibers and (c) high magnification FESEM image

Table 25: Average diameter of the fibers formed from coaxial GNaCl20 solution

[NaCl]	**Average Diameter (nm)**	**Standard Deviation (nm)**
20 wt/v%	1185	± 599

Once electrospun the fibers were analyzed for morphology and average fiber diameter utilizing FESEM images. **Figure 39** demonstrates the morphology and size distributions of the coaxial GNaCl20 fibers. It can be seen from the FESEM images obtained, that the fibers demonstrate randomly aligned, continuous, ribbon like morphologies with a relatively good distribution of intrafiber salts. Interfibers salts were also present in the fibers but are not

demonstrated in **figure 39a**. The intrafiber salts can be seen with relative ease in low magnification FESEM but are extremely apparent in the high magnification image [**Figure 39c**]. The high magnification FESEM shows several intrafiber salts along one fiber, some of which are surface penetrating and others are subsurface. The size distribution of these fibers (n = 50) is mostly normal with a slight positive skew and a mean diameter of 1185 nm ($\pm$ 599 nm) as demonstrated by the histogram. As was seen with the monoaxial gelatin fibers, the average fiber diameter appears high in comparison to previous literature. Again, this could be due to the increased conductivity and viscosity of the GNaCl20 solution which has been shown to play a role in electrospun gelatin fiber diameters [151, 152, 153]. The morphology of these coaxial fibers is not novel as the continuous ribbon structure has been recorded previously for both gelatin and PVDF-TrFE nanofibers [152, 159]. The average fiber diameter of these coaxial fibers is also in context with previous literature regarding these polymers monoaxially as well as PVDF-TrFE in a blend polymer system [159, 160, 161].

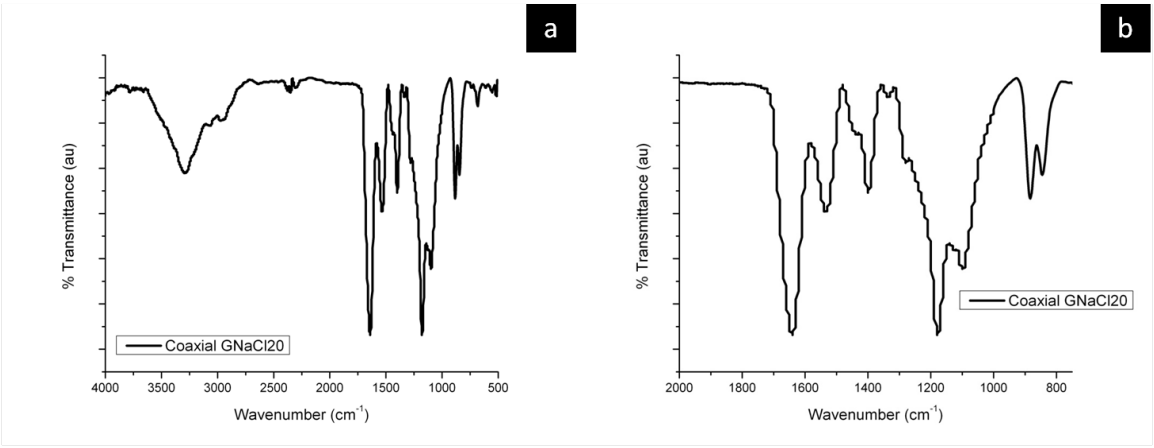

Figure 40: FTIR spectrograph of as spun coaxial PVDF-TrFE core and gelatin with 20 wt/v% NaCl shell nanofibers (a) 500-4000 (b) 750-2000 cm^{-1}

Table 26: Coaxial GNaCl20 FTIR prominent peaks

Polymer	Group	Mode	Peak Location (cm^{-1})
Gelatin	Amide I band (C=O)	Stretching	1630-1650
Gelatin	Amide II band (N-H)	Bending	1530-1550
PVDF-TrFE	(C-F_2),(C-C)	Sym. stretch, sym. stretch	835-845
PVDF-TrFE	(C-H_2),(C-F_2),(C-F_2)	Rock, antisym. stretch, rock	878-885
PVDF-TrFE	(C-C),(C-F_2),(C-H_2)	Antisym. stretch, wag, wag	1060-1080
PVDF-TrFE	(C-F_2),(C-F_2)	Antisym. stretch, rock	1168-1174
PVDF-TrFE	(C-H_2),(C-C)	Wag, sym. stretch	1390-1405

FTIR was utilized on the as-spun coaxial fibers in order to ensure the presence of both gelatin and PVDF-TrFE as well as to determine that the piezoelectric β-phase of PVDF-TrFE was present. **Figure 40** demonstrates the FTIR spectra for coaxial GNaCl20 fibers and the prominent peaks are labeled in **table 26**. As can be referenced from the table, the spectra demonstrates pronounced peaks for both the proposed core and shell polymers. The peaks that are present for PVDF-TrFE are well known to correspond to the ferroelectric β-phase while the peaks for the α-phase are absent (870, 970 and 1179 cm^{-1}) [162, 163, 164]. Although this spectra cannot prove that the fibers are arranged in a core-shell morphology, it does exhibit the presence of both polymers and that PVDF-TrFE is in the piezoelectric phase.

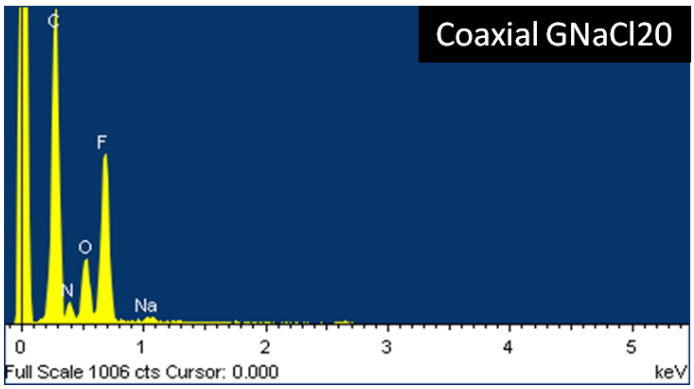

Figure 41: EDS spectrographs of as spun coaxial PVDF-TrFE core and gelatin with 20 wt/v% sodium chloride shell nanofibers

Table 27: The atomic and weight percents of specific elements in coaxial GNaCl20 fibers

Coaxial GNaCl20		
Element	**Weight %**	**Atomic %**
C	40.0	49.4
N	7.2	7.6
O	11.9	11.0
F	40.3	31.5
Na	0.7	0.5

Another method that was utilized to determine the presence of both the salts and the two polymers was EDS. The spectra in **figure 41** demonstrates several peaks of importance including a fluorine, oxygen, nitrogen and sodium peak [**Table 27**]. The carbon peak although important gives no information about the presence of any unique materials. The importance of the sodium peak is that it indicates the presence of NaCl in the coaxial fibers. This result confirms what was observed in the FESEM images. The fluorine peak indicates that the fluoropolymer PVDF-TrFE is present in the fibers and in relatively large amounts. The last two important elements, oxygen and nitrogen indicate the presence of gelatin. This spectra reaffirms the findings of the other analytical methods but once again it does not provide proof that the fibers were in a core-shell morphology.

5.2. CHONDROITIN SULFATE BLEND POLYMER SYSTEMS

5.2.1. PEO AND CHONDROITIN SULFATE

Poly (ethylene oxide) (PEO) was investigated for its capacity to act as a co-electrospinning blend polymer for the glycosaminoglycan (GAG) chondroitin sulfate (ChS) during electrospinning. Both PEO and ChS are soluble in deionized water and all solutions were electrospun using only deionized water as the solvent. PEO maintains charge neutrality in aqueous solutions which made it of primary interest in this study in order to determine how the blend polymers charge in solution effects the fiber forming capacity. Each solution was electrospun containing 5 wt/v % PEO and 10 wt/v % ChS which is a mer molar ratio of

approximately 1:5.3 ChS to PEO. The solutions were measured prior to electrospinning in order to determine pH, conductivity (change with respect to deionized water) and kinematic viscosity. These solution parameters can be found in **table 28**.

Table 28: PEO–ChS Solution Parameters

pH	Conductivity (mS)	Kinematic Viscosity (cSt)
5.6	1.67	1579

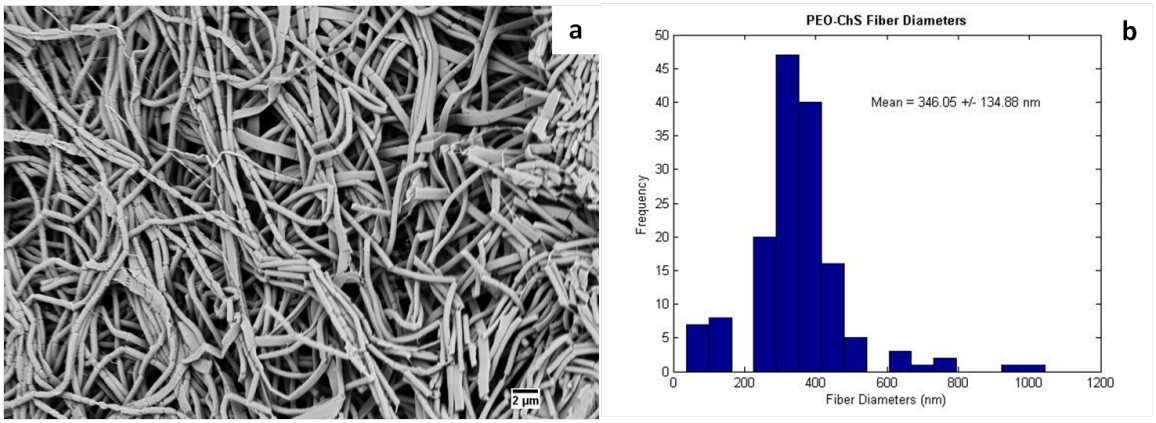

Figure 42: PEO-ChS nanofibers (a) FESEM image and (b) histogram of fiber diameters

Three solutions were electrospun under similar environmental conditions and utilizing the same electrospinning parameters. Once electrospun the fibers were analyzed for morphology and average fiber diameter utilizing FESEM images. **Figure 42** demonstrates the morphology of the blended fibers and their size distributions. It can be seen from the FE-SEM images obtained that PEO-ChS fibers demonstrated a cylindrical morphology with regions of thinning within the fiber. In these thin regions small fibrous threads (60-150 nm) are visible connecting the larger cylindrical components of the fibers (250-1000 nm). The size distribution of these fibers (n = 150) was mostly normal with a mean diameter residing at 346.1 nm ($\pm$ 134.9 nm) as demonstrated by the histogram. The fiber diameter distribution observed is similar to those described in previous literature where PEO has been electrospun monoaxially, at similar parameters, in a polymer blend or individually [165, 166]. The brittle non-continuous morphology observed appears to be unique to this

study as most literature reports smooth, continuous cylindrical fibers. This may be due to the inclusion of the GAG, ChS, which is known to be a rigid biopolymer [167].

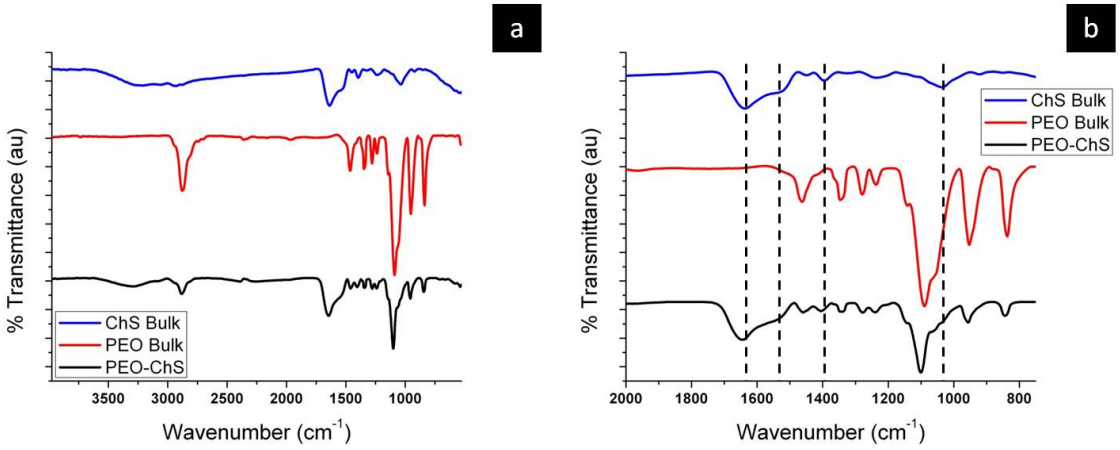

Figure 43: FTIR spectrographs for bulk ChS, bulk PEO and the PEO-ChS fibers (a) 500-4000 cm^{-1} and (b) range of interest 750-2000 cm^{-1}

Table 29: PEO–ChS FTIR peaks of interest

Group	**Mode**	**Peak Location (cm^{-1})**
Amide I band (C=O) coupled with (N-H)	Stretching and bending respectively	1630-1650
Amide II band (N-H)	Bending	1540-1560
(COO^-)	Symmetrical vibration	1400-1415
Pyranose ring	Multiple vibrations	950-1100

FTIR spectroscopy was utilized in order to determine the presence of ChS in the PEO-ChS blend fibers [**Figure 43**]. The peaks of interest in order to determine the presence of ChS in the blended fibers are listed in **table 29**. As can be seen from the FTIR spectra the appearance of several peaks in the PEO-ChS fibers indicate the presence of ChS. The peak around 1640 cm^{-1} is indicative of the amide I band seen in bulk ChS and reported previously in literature. This peak indicates the presence of the amide groups not otherwise observed in PEO. The shoulder around 1540 cm^{-1} is the amide II band which further indicates the presence of ChS in the fibers. The presence of symmetrical vibrations of a carboxylate group at 1400 cm^{-1} further demonstrates the presence of ChS. The final

observable difference between bulk PEO and the PEO-ChS fibers is the shoulder around 1035 cm^{-1} which indicates the presence of pyranose rings from ChS. Along with the many observable peaks for ChS in the dual polymer fibers, the distinguishable peaks of PEO are also present including: (C-O-C) stretch at 1104 cm^{-1}, (CH_2) rock coupled with (C-O-C) vibration at 960 cm^{-1} and (CH_2) rock at 841 cm^{-1}.

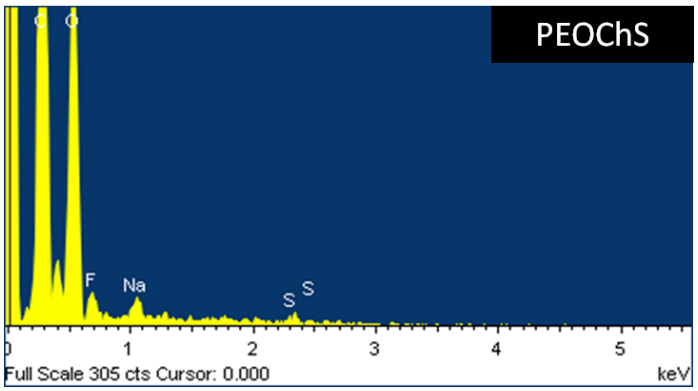

Figure 44: EDS spectrograph for the PEO-ChS fibers

Table 30: The atomic and weight percents of specific elements in PEO-ChS fibers

PEO-ChS		
Element	**Weight %**	**Atomic %**
C	56.5	64.1
O	38.1	32.5
F	3.2	2.3
Na	1.0	0.6
S	1.3	0.5

In order to further determine the presence of ChS in the PEO-ChS fibers EDS was utilized [**Figure 44**]. The spectrograph demonstrates a large presence of the expected elements for PEO including carbon and oxygen. Along with these basic elements the spectrograph also demonstrates the presence of two important elements sodium (Na) and sulfur (S) [**Table 30**]. These two peaks indicate the presence of ChS which contains sulfur and is commonly complexed with sodium at the sulfate group ($-SO_3^-$). The intensities of these peaks are weak, 1.01 wt% and 1.28 wt% respectively, indicating that the concentration of

ChS within the fibers may be low. Although this is likely, it is also possible that only the surface concentration is low given that EDS is a surface technique and does not penetrate into the matrix.

Overall, it can be stated that PEO-ChS solutions have a high fiber forming capacity and demonstrate the presence of both polymers. The fibers also demonstrate a uniform size distribution which is within the indicated range of optimal fiber diameters for chondrocyte cell viability [168].

5.2.2. PAA AND CHONDROITIN SULFATE

Poly (acrylic acid) (PAA) was investigated for its capacity to act as a co-electrospinning polymer for the glycosaminoglycan (GAG) chondroitin sulfate (ChS). Both PAA and ChS are soluble in deionized water and all solutions were electrospun using only deionized water as the solvent. PAA maintains a net negative charge in aqueous solutions which made it of primary interest in this study in order to determine how the blend polymers charge in solution effects the fiber forming capacity. Each solution was electrospun containing 5 wt/v % PAA and 10 wt/v % ChS which is a mer molar ratio of approximately 1:3.2 ChS to PAA. The solutions were measured prior to electrospinning in order to determine pH, conductivity (change with respect to deionized water) and kinematic viscosity. These solution parameters can be found in **table 31**.

Table 31: PAA–ChS Solution Parameters

pH	**Conductivity (mS)**	**Kinematic Viscosity (cSt)**
4.0	2.24	18.8

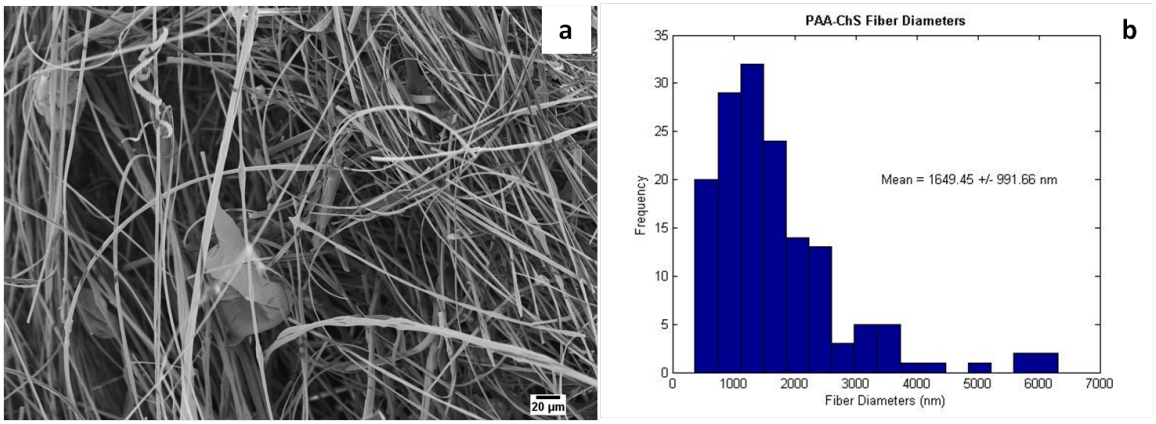

Figure 45: PAA-ChS nanofibers (a) FESEM image and (b) histogram of fiber diameters

Three solutions were electrospun under similar environmental conditions and utilizing the same electrospinning parameters. Once electrospun the fibers were analyzed for morphology and average fiber diameter utilizing FESEM images. **Figure 45** demonstrates the morphology of the dual polymer fibers and their size distributions. It can be seen from the FESEM images obtained that PAA-ChS fibers demonstrated a mostly cylindrical morphology with regions of fibers twisting, braiding and adhering to other fibers, forming large fiber bundles. A single non-bundled fiber was much smaller (300-500 nm) then the fiber bundles (1000-6000 nm), which were most prevalent in the imaged mats. The size distribution of these fibers (n = 150) is unimodal with a positive skew and the mean diameter is located at 1649.5 nm ($\pm$ 991.7 nm) as demonstrated by the histogram. The fiber diameter distribution and morphology is different from previous literature observations [169, 170, 171]. The fibers bundling nature has not been reported previously in literature and may be a result of a number of factors including the inclusion of the GAG, ChS. This inclusion would increase the ionic strength of the solution *via* the addition of positively charged sodium ions. The increased ionic strength may influence a conformational change of the PAA chains in order to reduce electrostatic forces in solution [170].

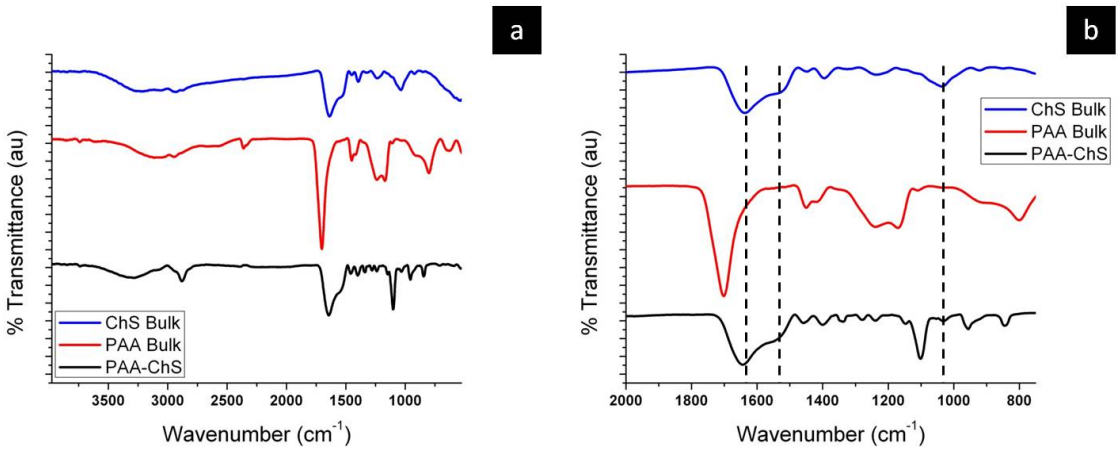

Figure 46: FTIR spectrographs for bulk ChS, bulk PAA and the PAA-ChS fibers (a) 500-4000 cm^{-1} and (b) range of interest 750-2000 cm^{-1}

Table 32: PAA–ChS FTIR peaks of interest

Group	**Mode**	**Peak Location (cm^{-1})**
Amide I band (C=O) coupled with (N-H)	Stretching and bending respectively	1630-1650
Amide II band (N-H)	Bending	1540-1560
Pyranose ring	Multiple vibrations	950-1100

FTIR spectroscopy was utilized in order to determine the presence of ChS in the PAA-ChS fibers [**Figure 46**]. The peaks of interest used to determine the presence of ChS in the polymer blend fibers are listed in **table 32**. As can be seen from the FTIR spectra the appearance of several peaks in the PAA-ChS fibers indicate the presence of ChS. The peak around 1640 cm^{-1} is indicative of the amide I band seen in bulk ChS and reported previously in literature. This peak indicates the presence of the amide groups not otherwise observed in PAA. The shoulder around 1540 cm^{-1} is the amide II band which further indicates the presence of ChS in the fibers. Although small, the final peak of interest seen in the PAA-ChS FTIR is the weak peak at 1035 cm^{-1} which indicates the presence of pyranose rings from ChS. Along with the ChS peaks in the FTIR of the fibers, the peaks associated with PAA can also be distinguished and include: the (C=O) stretch at 1042 cm^{-1} which is visualized by a broadening and slight shift to to the left of the amide I band and the (C-O)

stretch coupled with (O-H) bend of neighboring carboxyl groups at 1110 cm^{-1}. The later of the two PAA peaks is shifted down as a result of decreased coupling of the neighboring carboxyl (O-H) bending resulting in just the presence of a (C-O) stretching peak.

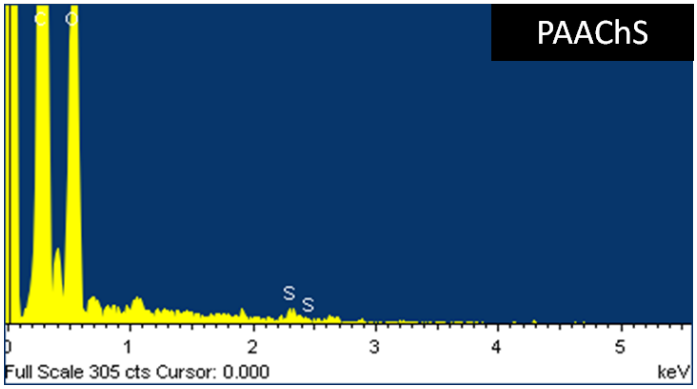

Figure 47: EDS spectrograph for the PAA-ChS fibers

Table 33: The atomic and weight percents of specific elements in PAA-ChS fibers

PAA-ChS		
Element	**Weight %**	**Atomic %**
C	61.5	68.4
O	37.3	31.2
S	1.2	0.5

EDS was utilized in order to provide support for the presence of ChS in the PAA-ChS fibers [**Figure 47**]. Similarly to the PEO-ChS spectrograph, there is a large presence of the expected elements for PAA including carbon and oxygen. Along with these elements, the spectrograph also demonstrates the presence of sulfur (S) atoms. This sulfur peak further indicates the presence of ChS in the polymer blend fibers. There also appears to be signs of a sodium peak at around 1 keV which would be expected due to the complexing of sodium to the sulfate group ($-SO_3^-$). The intensities of these peaks are weak, with sodium not being recognized by the analytical software and sulfur showing up at 1.2 wt% [**Table 33**]. Again, this may indicate that the concentration of ChS within the fibers may be low but it is also possible that only the surface concentration is low given that EDS is a surface technique and does not penetrate into the matrix.

The overall impression is that PAA-ChS solutions exhibit fiber forming capacity but with potentially low fiber yields. Also, the concentration of ChS appears to be low when analyzing the EDS data but the FTIR spectra showed a significant presence of ChS. This may imply low surface concentrations of ChS in the composite fibers but higher concentrations at greater matrix depths. It is also important to note the novel morphology formed by the PAA-ChS composite fibers which resulted in large fiber bundles and a fiber distribution not considered within the viable range for chondrocytes [168].

5.2.3. HA AND CHONDROITIN SULFATE

Hyaluronic acid (HA) was investigated for its capacity to act as a co-electrospinning polymer for the glycosaminoglycan (GAG) chondroitin sulfate (ChS). HA and ChS are soluble in a mixture of 1:1 DMF:deionized water and all solutions were electrospun using this solvent mixture. HA maintains a net negative charge in aqueous solutions and is also a natural polymer often found along with aggrecan in articulating cartilage. The combination of these features made HA a prime candidate for this study and determining how the blend polymer charge in solution effects the fiber forming capacity of this natural polymer solution is of extreme interest. Each solution was electrospun containing 2 wt/v % HA and 10 wt/v % ChS which is a mer molar ratio of approximately 4:1 ChS to HA. The solutions were measured prior to electrospinning in order to determine pH and conductivity (change with respect to deionized water). The kinematic viscosity of the electrospun HA-ChS solutions had to be estimated *via* a dilution series, due to the large resistance to flow demonstrated by the electrospun solutions. These solution parameters can be found in **table 34** and the dilution series plot is **figure 48**.

Table 34: HA–ChS Solution Parameters

pH	**Conductivity (mS)**	**Kinematic Viscosity (cSt)**
6.5	1.01	5887

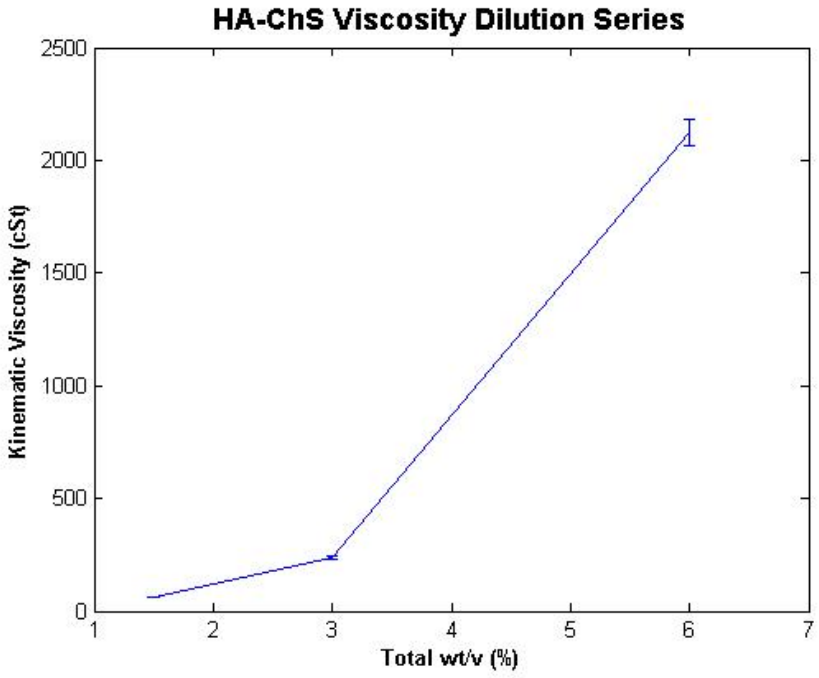

Figure 48: Dilution series plot used to estimate the kinematic viscosity (with error bars)

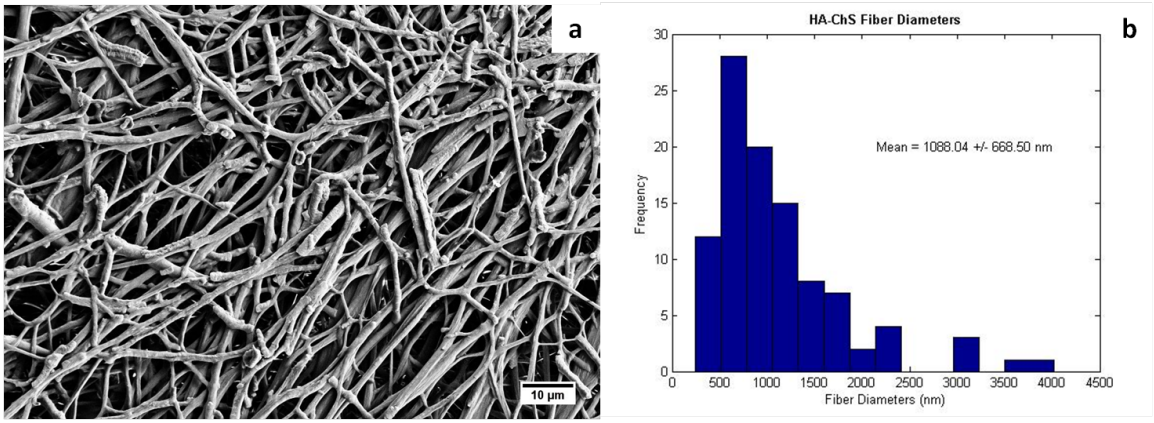

Figure 49: HA-ChS nanofibers (a) FESEM image and (b) histogram of fiber diameters

Figure 50: HA-ChS nanofibers high magnification FESEM image

Three solutions were electrospun under similar environmental conditions and utilizing the same electrospinning parameters. Once electrospun the fibers were analyzed for morphology and average fiber diameter utilizing FESEM images. **Figure 49** demonstrates the morphology of the dual polymer fibers and their size distributions. It can be seen from the FESEM images obtained that HA-ChS fibers demonstrated continuous semi cylindrical fibers with a rough fiber surface morphology and a significant degree of branching. The imaged mats contained a large variation of fiber sizes and types including large continuous fibers and smaller branched fibers. The size distribution of these fibers (n = 100) is unimodal with a positive skew and a mean diameter of 1088 nm ($\pm$ 668.5 nm) as demonstrated by the histogram. The fiber diameter distribution and morphology is different from previous literature observations in a multitude of ways. The fibers large average diameter is the most notable difference from previous literature which recorded averages at or below 300 nm [172, 173, 174, 175]. The HA-ChS fibers also differ from previous literature in that they exhibit both continuous and highly branched morphologies. Previously, it had been demonstrated that HA at low concentrations would form continuous fibers but at high concentrations in the same solution would exhibit a highly branched morphology [172]. The fiber surface roughness is also a novel feature of these dual polymer fibers and its appearance at high magnifications indicates the potential for fiber bundling as was witnessed for

the PAA-ChS fibers [**Figure 50**]. This novel morphology may be a result of a number of factors including the inclusion of the GAG, ChS. Due to HA having a net negative charge in solution like PAA, a similar mechanism could be attributing to the fiber bundling behavior. This involves increased ionic strength influencing a conformational change of the HA chains in order to reduce electrostatic forces in solution [170].

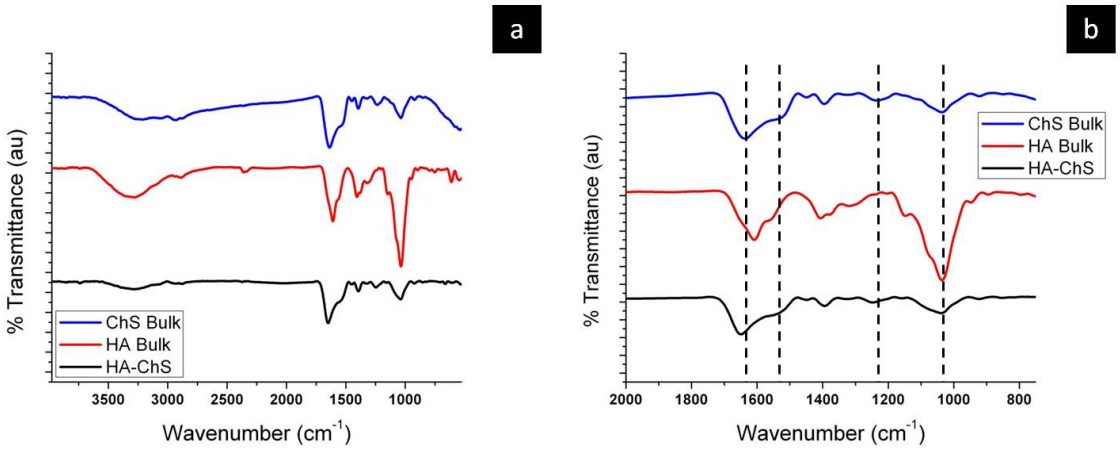

Figure 51: FTIR spectrographs for bulk ChS, bulk HA and the HA-ChS fibers (a) 500-4000 cm^{-1} and (b) range of interest 750-2000 cm^{-1}

Table 35: HA–ChS FTIR peaks of interest

Group	**Mode**	**Peak Location (cm^{-1})**
Amide I band (C=O) coupled with (N-H)	Stretching and bending respectively	1630-1650
Amide II band (N-H)	Bending	1540-1560
($-SO_3^-$)	Antisymmetrical stretching	1220-1235
Pyranose ring	Multiple vibrations	950-1100

FTIR spectroscopy was utilized in order to determine the presence of ChS in the HA-ChS fibers [**Figure 51**]. The peaks of interest used to determine the presence of ChS in the polymer blend fibers are listed in **table 35**. As can be seen from the FTIR spectra the appearance of a single peak and several peak shifts in the HA-ChS fibers indicate the presence of ChS. Many of the peaks observed are shared due to the drastically similar molecular structure of these two GAGs.The peak around 1640 cm^{-1} is indicative of the

amide I band seen in bulk ChS and reported previously in literature. This peak demonstrates a shift to the left in comparison to bulk HA to a position similar to that of the amide I band in bulk ChS. This shift is an indicator but it could be attributed to other factors and so the presence of other peaks is important. The shoulder around 1540 cm^{-1} is the amide II band which is also shifted to a position resembling that of bulk ChS rather than bulk HAs amide II band. Another shared peak at 1035 cm^{-1} demonstrates a change in peak intensity from bulk HA to an intensity closer to that witnessed in bulk ChS. The final and most definitive peak of interest is the weak peak at 1230 cm^{-1} which indicates the presence of sulfate. This peak is the most definitive indicator in that it is one of the few unshared peaks and represents the sulfate group which is not present in HA.

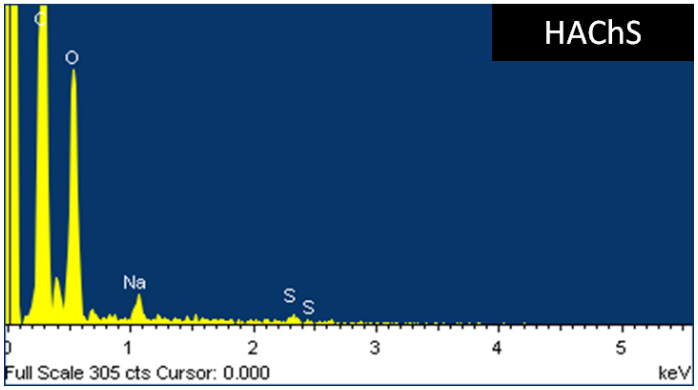

Figure 52: EDS spectrograph for the HA-ChS fibers

Table 36: The atomic and weight percents of specific elements in HA-ChS fibers

HA-ChS		
Element	**Weight %**	**Atomic %**
C	58.6	66.3
O	37.0	31.4
Na	2.2	1.3
S	2.3	1.0

HA-ChS fibers were also analyzed under EDS in order to support findings from other analytical methods [**Figure 52**]. Similarly to all previous spectrographs, there is a large presence of the expected elements for HA including carbon, oxygen and nitrogen (although

not labeled this peak appears around 0.4 keV). Along with these elements, the spectrograph also demonstrates the presence of sulfur (S) and sodium (Na) atoms. The sulfur peak further indicates the presence of ChS in the polymer blend fibers due to HAs nature of being the only non sulfated GAG. The sodium peak at around 1 keV is in part due to the presence of ChS and in part due to the complex of sodium to HAs carboxyl group. The intensities of these peaks are weak but stronger then previously described dual polymer fibers, with sodium levels at 2.2 wt% and sulfur showing up at 2.3 wt% [**Table 36**]. This indicates that although the surface concentration of ChS may be low, it is increased from that of previously described results. This increase could be due, in part, to the high molar ratio of ChS to HA in the HA-ChS solutions, which was greatly increased from previously described polymer systems.

Analysis of the HA-ChS fibers has demonstrated the high fiber forming capacity of this polymer blend system. EDS and FTIR analysis have demonstrated the presence of sulfur and sulfate peaks in the HA-ChS fibers which would not appear in the analysis of HA. The morphology of these fibers is novel and may be explained by the effects of ionic strength on HA and ChS chain conformation. The overall mean diameter of these fibers is at the top of the range for viable chondrocyte infiltration, proliferation and differentiation and may be prove promising in further investigation.

5.2.4. PAAm AND CHONDROITIN SULFATE

Poly (allylamine) (PAAm) was investigated for its capacity to act as a co-electrospinning polymer for the glycosaminoglycan (GAG) chondroitin sulfate (ChS). PAAm and ChS are both soluble in deionized water but form a polyelectrolytic complex due to the net negative charge of ChS ($pKa_{sulfate}$=2-2.5) (pKa_{COOH}=3.5-4) and the net positive charge of PAAm (pKa = 8.7-8.8) at neutral pH [176]. In order to electrospin this polymer blend, the solution needed to be acidified to a pH below the pKa for ChSs sulfate. This was accomplished by dissolving ChS and PAAm in a mixture of 1:1 THF:deionized water which brought the

pH of the solution close to 1. All of the fiber mats were electrospun using this solvent mixture which permitted the combination of the dissimilarly charged polymers without gelling. PAAm was chosen for this study due to its net positive charge in an aqueous solution, which is important for determining how the blend polymer charge in solution effects the fiber forming capacity. Each solution was electrospun containing 20 wt% PAAm and 10 wt/v% ChS which is a mer molar ratio of approximately 1:7.2 ChS to PAAm. The PAAm solutions could not be measured with ChS due to the lack of availability of PAAm from Sigma-Aldrich but PAAm in TFA was measured for pH, conductivity (change with respect to deionized water) and kinematic viscosity. These solution parameters can be found in **table 37**. It is important to note that the conductivity was measured in a TFA solution with a pH of 4 rather than 1 in order to avoid damaging the equipment.

Table 37: PAAm in TFA Solution Parameters

pH	Conductivity (mS)	Kinematic Viscosity (cSt)
1.0	18.57	614

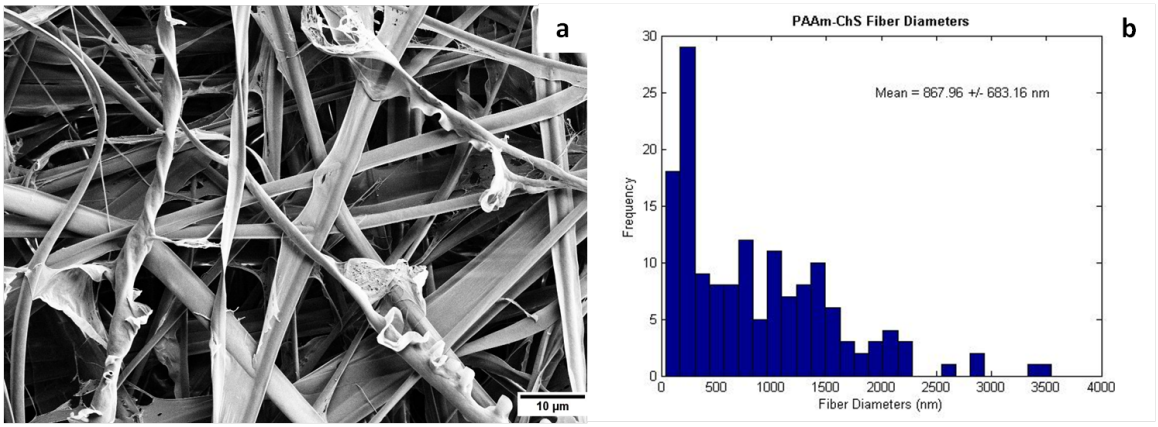

Figure 53: PAAm-ChS nanofibers (a) FESEM image and (b) histogram of fiber diameters

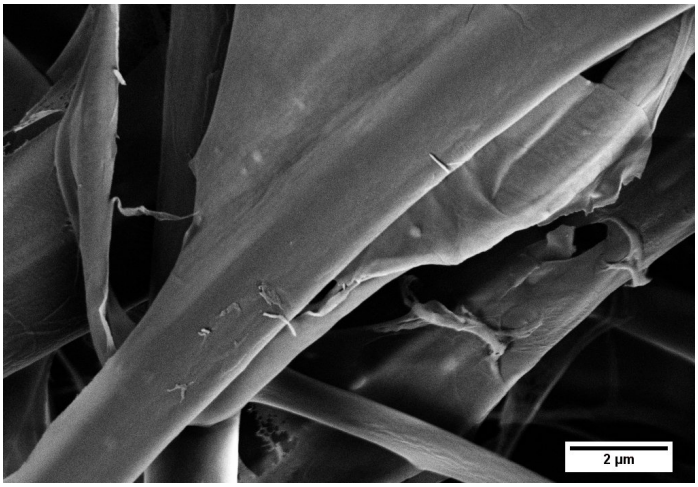

Figure 54: High magnification of PAAm-ChS nanofibers demonstrating the thin film around the fibers

Three solutions were electrospun under similar environmental conditions and utilizing the same electrospinning parameters. Once electrospun the fibers were analyzed for morphology and average fiber diameter utilizing FESEM images. **Figure 53** demonstrates the morphology of the dual polymer fibers and their size distributions. It can be seen from the FESEM images obtained that PAAm-ChS fibers demonstrated randomly oriented, continuous, semi-cylindrical fibers with what appears to be a second interpenetrating network of smaller, semi-cylindrical fibers and filmed regions. The size distribution of these fibers (n = 150) appears to demonstrate a slight bimodal distribution with an overall mean diameter of 868 nm ($\pm$ 683.2 nm) as demonstrated by the histogram. The two modes of the distribution appear to be centered around 250 nm and 1125 nm. The morphology observed tends to support the idea that two fiber populations are present. This is intriguing in that one population may or may not contain an excess concentration of ChS in comparison to the other population. The mean fiber diameter recorded has been observed in previous literature, in which PAAm fibers were electrospun from a TFA solution or with glutaraldehyde in solution [177]. The morphology of the PAAm-ChS fibers appears to be novel and has not been reported previously [111, 177, 178, 179, 180]. This novel morphology may be a result of a number of factors including the inclusion of the GAG, ChS. Previous literature which

referenced electrospinning PAAm fibers with an anionic polyelectrolyte usually involved PAA which can be fully protonated at relatively high pHs due to its high pKa of 6.5 [111]. The researchers were able to reduce the solution to a pH of 2.7 which resulted in fully protonated PAA. In the case of ChS the sulfate group ($-SO_3^-$) cannot be fully protonated until the pH is below 0-0.5. This means that at a pH of 2 (1:1 TFA:deionized water), almost half of the sulfate groups are protonated and able to complex with the fully protonated amine groups of PAAm. The ability for the complex to form may play a role in the observed bimodal morphology. The filming that is visualized is most likely a result of the hygroscopic nature of PAAm. As water is absorbed from the atmosphere the PAAm fibers will start to film and swell, while the complex fibers will retain their fibrous morphology.

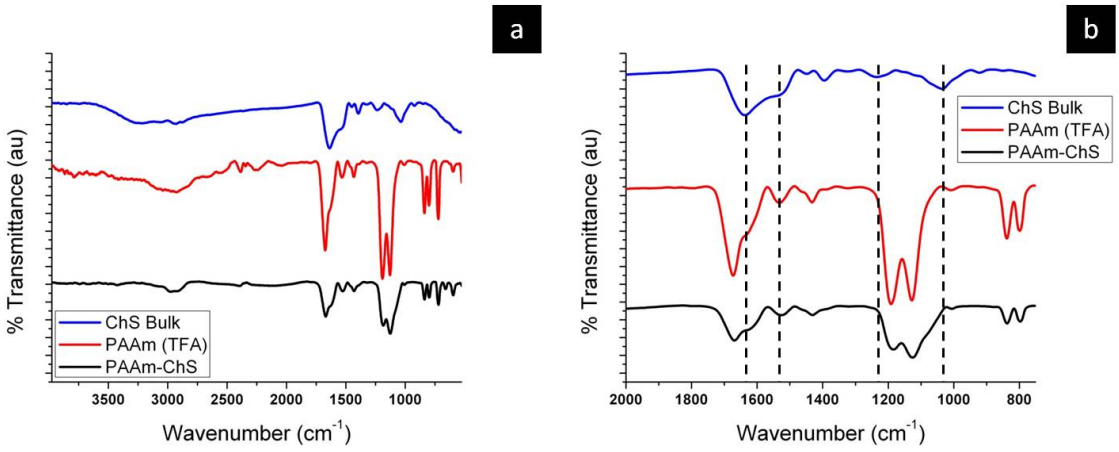

Figure 55: FTIR spectrographs for bulk ChS, monoaxial PAAm fibers and the PAAm-ChS (a) 500-4000 cm^{-1} and (b) range of interest 750-2000 cm^{-1}

Table 38: PAAm–ChS FTIR peaks of interest

Group	**Mode**	**Peak Location (cm^{-1})**
Amide I band (C=O) coupled with (N-H)	Stretching and bending respectively	1630-1650
Amide II band (N-H)	Bending	1540-1560
($-SO_3^-$)	Antisymmetrical stretching	1220-1235
Pyranose ring	Multiple vibrations	950-1100

FTIR spectroscopy was utilized in order to determine the presence of ChS in the PAAm-ChS fibers [**Figure 55**]. The peaks of interest used to determine the presence of ChS in the

polymer blend fibers are listed in **table 38**. As can be seen from the FTIR spectra a couple of peak shifts in the PAAm-ChS fibers may indicate the presence of ChS. Many of the peaks observed in the FTIR spectra are overlapping which makes determining the presence of specific bands difficult. The peak around 1640 cm^{-1} is indicative of the amide I band seen in bulk ChS and reported previously in literature. This peak is blocked by the amine (N-H) bending peak located around 1680 cm^{-1} of PAAm. This peak can be observed as the broad shoulder to the right of the amine peak in the PAAm-ChS fibers, although the appearance of this peak cannot be solely attributed to the amide I band of ChS. The amide II band at 1540 cm^{-1} is blocked by another (N-H) deformation peak of PAAm and thus cannot be used for determining the presence of ChS. The peak which is indicative of the sulfate group of ChS is also blocked but in this instance the overlapping peak is the large splitting peak due to (O-H) stretching indicating the presence of water. Another peak, which can normally be used to indicate the presence of a GAG, is located at 1035 cm^{-1} in the ChS bulk sample. This peak, which indicates the presence of pyranose rings, is blocked by the sharp splitting peak which ranges from 1100-1210 cm^{-1}. This large splitting peak indicates the presence of (O-H) stretching which implies there is a large quantity of water which was absorbed due to the hygroscopic nature of PAAm fibers. This peak in the PAAm-ChS fibers appears to broaden substantially on the right side which may indicate the presence of the pyranose ring vibrations. Due to the large overlap of peaks it is hard to distinguish any obvious bands that point to the presence of ChS but these few peak shift may give minor indications of its presence. It is also interesting to note that the amine peak around 1680 cm^{-1} is greatly truncated which may indicate the onset of complex formation between the sulfate and the amine groups, although this may be a result of the decreased concentration of pure PAAm.

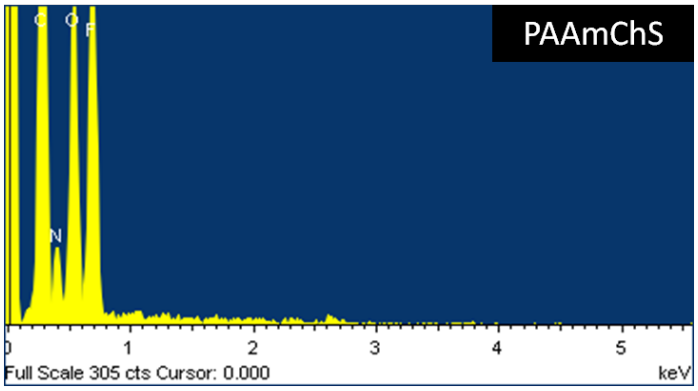

Figure 56: EDS spectrograph for the PAAm-ChS fibers

Table 39: The atomic and weight percents of specific elements in PAAm-ChS fibers

PAAm-ChS		
Element	**Weight %**	**Atomic %**
C	37.9	46.3
N	9.3	9.8
O	21.3	19.6
F	31.5	24.4

PAAm-ChS fibers were also analyzed utilizing EDS for indications of the presence of ChS [**Figure 56**]. Similarly to all previous spectrographs, there is a large presence of the expected elements for PAAm including carbon and nitrogen. Along with these elements, the spectrograph also demonstrates the presence of fluorine (F) and oxygen (O) [**Table 39**]. The presence of F indicates that there is residual TFA in solution while the oxygen peak may indicate the presence of a number of entities including: water, TFA and ChS. There appears as though peaks for sulfur (S) and sodium (Na) atoms may be present around 2.35 keV and 1.05 keV, respectively but these peaks are surround by noise and thus cannot be used to indicate the presence of ChS. The lack of peaks which correlate to ChS could be due to the large presence of other elements at the surface which may block or over shadow the signal, for example fluorine. The lack of peaks may also be attributed in part to the low molar ratio of ChS:PAAm in comparison to the other polymer systems.

After analysis it appears as though PAAm-ChS solutions may be fiber forming but the

data obtained it not conclusive. The FTIR spectra exhibit peak shifts which may correlate to the presence of specific ChS bands but these shifts may not be solely attributable to the ChS vibration modes. Also, the novel fiber morphology demonstrated by the PAAm-ChS fibers seems to indicate the presence of two unique fiber networks, which may correlate to differences in polyelectrolytic complexing.

6. CONCLUSIONS

6.1. COLLAGEN AND GELAIN INTRAFIBER POROSITY AND SALT INFILTRATION

Gelatin and collagen were successfully electrospun from solutions containing suspended NaCl and NaCit. The fibers demonstrated the ability to entrap salts within the matrix as well as allow for salt infiltration into the individual fibers. The monoaxial gelatin-salt fibers exhibited relatively large, continuous, ribbon like morphologies with randomly dispersed, network and fiber infiltrating salts. The GNaCl4 and GNaCit4 fibers displayed a low density of visual salts and no measurable quantity of identifying atoms. The GNaCl20 and GNaCit20 fibers demonstrated extremely visible salt infiltration and measurable quantities of the salt identifying elements. The collagen was electrospun utilizing the same parameters as the gelatin control fibers. The results for the collagen solutions were very similar to those of the gelatin control. The low salt concentration fibers demonstrated some salt infiltration while the high concentrations demonstrated a very dense infiltration. The collagen samples demonstrated much smaller fibers then the gelatin samples but still had a continuous, ribbon like morphology. These results demonstrate that the intra- and interfiber salt concentrations of both gelatin-salt and collagen-salt mats, can be controlled by controlling the concentration of the suspended salts in solution.

A small sample size of, coaxial PVDF-TrFE core-Gelatin with 20 wt/v% NaCl shell fibers, were analyzed to determine if the optimal processes could be further applied to coaxial electrospinning. These fibers demonstrated all of the same positive results as their high concentration monoaxial counterparts. Along with demonstrating salt infiltration, these fibers also exhibited the presence of the piezoelectric phase of the PVDF-TrFE core. These two results are highly important for future analysis of how the inter- and intrafiber salts and leached porosity, effect the piezoelectric response.

FTIR Analysis of the monoaxial fibers after applying a non-toxic DHT crosslinking

treatment demonstrated indications that the crosslinking process was working and that the NaCit may be interacting with the peptide backbone. This analysis was further supported by FESEM images of the DHT crosslinked and leached fibrous mats. Most of these mats retained their fibrous structure to some degree but a greater degree of crosslinking may be desired in order to maintain any porous structures obtained.

While all of the fibers exhibited the ability to entrap salts to some degree only the 20 wt/v% NaCit containing salts were able to generate intrafiber pores post leaching. This indicates that the best method for controlling the inter- and intrafiber porosity of these gelatin and collagen nanofibrous mats is by utilizing a NaCit salt suspension. Further studies are indicated in determining better methods of crosslinking in order to further analyze the effects of generating porosity by leaching the entrapped fibers in water.

6.2. CHONDROITIN SULFATE BLEND POLYMER SYSTEMS

Chondroitin sulfate was electrospun from four different polymer blend solutions each containing a blend polymer with a different net charge in solution. The exception was that HA and PAA solutions both maintained a net negative charge in solution but HA is a natural polymer commonly found in cartilage, while PAA is a synthetic polymer which has been shown to act similar to cartilage in combination with other polymers. The fiber forming capacity was analyzed for each polymer blend and it was found that all four polymer blends showed signs of both ChS and the blend polymer after electrospinning. The presence of multiple polymers in the fibers was determined by FTIR and EDS analysis, which demonstrated characteristic peaks and peak shifts, which may be correlated to the specific polymers.

Electrospinning of the polymer blends demonstrated the ability to electrospin sulfated GAGs with polymers of varying solution charge including net neutral (PEO), net negative and synthetic (PAA), net negative and natural (HA) and net positive (PAAm). Analysis of the electrospun fibers indicate that HA had the greatest fiber forming capacity of the four

blends while PAAm had the lowest/least distinguishable fiber forming capacity for dual polymer fibers. The amount of ChS observed in the fibers via EDS (wt%) correlated to the molar ratio of ChS to blend polymer in solution. As the molar ratio increased from one polymer solution to the next so did the concentration of sulfur and sodium atoms in the EDS spectra. This observation should be noted as a correlation and not causation and the effect of molar ratio should be further investigated before any conclusions can be made.

All of the polymers used as blends with ChS have been previously reported as biocompatible and pose no risk to future cell studies. It is important to note that all of these fibers would need to be crosslinked prior to cell studies in order to increase their chemical stability in media. The PAAm-ChS fibers would also require the removal of residual TFA by either neutralization with base or evaporation in a vacuum oven. Based on previous literature it would appear that the PEO-ChS fibers exhibited the most promising fiber distribution for chondrocyte growth, proliferation and differentiation. PAAm-ChS and HA-ChS fibers also demonstrated fiber distributions that would be viable for cell seeding but were at the upper end of the viable range. PAA-ChS fibers exhibited a distribution of large bundles of fibers which were above the range previously indicated for chondrocyte viability. The fiber morphologies may also play a role in their ability to act as a tissue scaffolds and the novel morphologies observed should be studied furthered in order to determine what role they may play in cell viability.

7. FUTURE WORK

7.1. COLLAGEN AND GELAIN INTRAFIBER POROSITY AND SALT INFILTRATION

- Further analysis of how the intra- and interfiber salt concentration can be controlled by controlling the solution concentration of both salts and peptide, would be of interest in order to further distinguish the most efficient control method.

- Application of these findings to further coaxial fiber studies and analyzing the effects of porosity and the intra- and interfiber salts on the piezoelectric response is of interest.

- The use of further coaxial studies could also be extended to understanding the effects of the salts and their residual porosity on cellular in-growth, attachment, proliferation and differentiation on these mats.

- Utilizing other methods of crosslinking may also be of interest in order to reduce time and increase the chemical stability of the fibrous mats.

7.2. CHONDROITIN SULFATE BLEND POLYMER SYSTEMS

- Further analysis of the effect of molar ratio on fiber forming capacity for each polymer blend system would be of interest in determining if the fiber concentration is controllable and/or limiting.

- Studies regarding how GAG concentration effects the fiber morphology may be of interest in order to determine how to decrease the average fiber diameters and how to control the fiber morphology to form a more uniform matrix.

- Crosslinking of these polymer blend fibers would be of interest in determining the ability to be used in aqueous environments as cell scaffolds and drug delivery devices.

- Quantifying and describing how each polymer blend effects the enzymatic digestion of ChS is of great interest.
- ChS release kinetics from each polymer blend in aqueous solutions may be of interest in determining the ability for these mats to act as drug delivery devices.
- Cell studies for each polymer blend system could be promising for future biomedical scaffolds. These studies may look at how each polymer system effects chondrogenesis and specific cartilage like tissue generation (*i.e.* collagen II formation and expression)

7. REFERENCES

[1] G. K. Vincent and V. A. Velkoff. The next four decades the older population in the united states: 2010 to 2050. Technical Report 1, U.S. Census Bureau, 2010.

[2] National Center for Chronic Disease Prevention and Health Promotion. *Healthy Aging: Helping People to Live Long and Productive Lives and Enjoy a Good Quality of Life*, 2011.

[3] F. J. Schoen. Mechanisms of function and disease of natural and replacement heart valves. *Annual Review of Pathology: Mechanisms of Disease*, 7(1):161–183, 2012. PMID: 21942526.

[4] N. T. Elliott and F. Yuan. A review of three-dimensional in vitro tissue models for drug discovery and transport studies. *Journal of Pharmaceutical Sciences*, 100(1):59–74, 2011.

[5] M. Lotz. Osteoarthritis year 2011 in review: biology. *Osteoarthritis and Cartilage*, 20(3):192 – 196, 2012.

[6] R. Adalbert and M. P. Coleman. Review: Axon pathology in age-related neurodegenerative disorders. *Neuropathology and Applied Neurobiology*, 39(2):90–108, 2013.

[7] A. D. Woolf and B. Pfleger. Burden of major musculoskeletal conditions. *Bulletin of the World Health Organization*, 81:646 – 656, 09 2003.

[8] B. H. Sun, C. W. Wu, and K. C. Kalunian. New developments in osteoarthritis. *Rheumatic Disease Clinics of North America*, 33(1):135 – 148, 2007.

[9] W. Zhang, G. Nuki, R. W. Moskowitz, S. Abramson, R. D. Altman, N. K. Arden, S. Bierma-Zeinstra, K. D. Brandt, P. Croft, M. Doherty, M. Dougados, M. Hochberg,

D. J. Hunter, K. Kwoh, L. S. Lohmander, and P. Tugwell. Oarsi recommendations for the management of hip and knee osteoarthritis: Part iii: changes in evidence following systematic cumulative update of research published through january 2009. *Osteoarthritis and Cartilage*, 18(4):476 – 499, 2010.

[10] Arthritis Foundation Staff. Osteoarthritis fact sheet. Technical report, Arthritis Foundation, 2008.

[11] Department of Chronic Diseases and Health Promotion Staff. Chronic rheumatic conditions. Technical report, World Health Organization, 2013.

[12] San Francisco Department of Orthopedic Surgery Staff University of California. Arthritis & joint replacement. Technical report, University of California, San Francisco, 2013.

[13] O. Bruyre, O. Ethgen, A. Neuprez, B. Zgels, Ph. Gillet, J.-P. Huskin, and J.-Y. Reginster. Health-related quality of life after total knee or hip replacement for osteoarthritis: a 7-year prospective study. *Archives of Orthopaedic and Trauma Surgery*, 132(11):1583–1587, 2012.

[14] M. Blagojevic, C. Jinks, A. Jeffery, and K. P. Jordan. Risk factors for onset of osteoarthritis of the knee in older adults: a systematic review and meta-analysis. *Osteoarthritis and Cartilage*, 18(1):24 – 33, 2010.

[15] J. Dunning, M. Nagendran, O. R. Alfieri, S. Elia, A. P. Kappetein, U. Lockowandt, G. E. Sarris, P. H. Kolh, and on behalf of the EACTS Clinical Guidelines Committee. Guideline for the surgical treatment of atrial fibrillation. *European Journal of Cardio-Thoracic Surgery*, 44(5):777–791, 2013.

[16] A. J. et al. Camm. Guidelines for the management of atrial fibrillation: The task force for the management of atrial fibrillation of the european society of cardiology (esc). *European Heart Journal*, 31(19):2369–2429, 2010.

[17] G. V. Naccarelli, H. Varker, J. Lin, and K. L. Schulman. Increasing prevalence of atrial fibrillation and flutter in the united states. *The American Journal of Cardiology*, 104(11):1534 – 1539, 2009.

[18] Mayo Clinic Staff. Atrial fibrillation. Technical report, Mayo Clinic, 2013.

[19] G. Y. H. Lip, R. Nieuwlaat, R. Pisters, D. A. Lane, and H. J. G. M. Crijns. Refining clinical risk stratification for predicting stroke and thromboembolism in atrial fibrillation using a novel risk factor-based approach: The euro heart survey on atrial fibrillation. *CHEST Journal*, 137(2):263–272, 2010.

[20] N. Bhardwaj and S. C. Kundu. Electrospinning: A fascinating fiber fabrication technique. *Biotechnology Advances*, 28(3):325 – 347, 2010.

[21] A. Greiner and J.H. Wendorff. Electrospinning: A fascinating method for the preparation of ultrathin fibers. *Angewandte Chemie International Edition*, 46(30):5670–5703, 2007.

[22] J. Lin, X. Wang, B. Ding, J. Yu, G. Sun, and M. Wang. Biomimicry via electrospinning. *Critical Reviews in Solid State and Materials Sciences*, 37(2):94–114, 2012.

[23] A. J. Meinel, O. Germershaus, T. Luhmann, H. P. Merkle, and L. Meinel. Electrospun matrices for localized drug delivery: Current technologies and selected biomedical applications. *European Journal of Pharmaceutics and Biopharmaceutics*, 81(1):1 – 13, 2012.

[24] N. E. Zander. Hierarchically structured electrospun fibers. *Polymers*, 5(1):19–44, 2013.

[25] G. C. Ingavle and J. K. Leach. Advancements in electrospinning of polymeric nanofibrous scaffolds for tissue engineering. *Tissue Engineering Part B: Reviews*, 00(00):1–17, 2013.

[26] A. Guo, M. Roso, M. Modesti, J. Liu, and P. Colombo. Hierarchically structured polymer-derived ceramic fibers by electrospinning and catalyst-assisted pyrolysis. *Journal of the European Ceramic Society*, 34(2):549 – 554, 2014.

[27] H. Chen, J. Di, N. Wang, H. Dong, J. Wu, Y. Zhao, J. Yu, and L. Jiang. Fabrication of hierarchically porous inorganic nanofibers by a general microemulsion electrospinning approach. *Small*, 7(13):1779–1783, 2011.

[28] H. Wu, W. Pan, D. Lin, and H. Li. Electrospinning of ceramic nanofibers: Fabrication, assembly and applications. *Journal of Advanced Ceramics*, 1(1):2–23, 2012.

[29] H. Wu, L. Hu, M. W. Rowell, D. Kong, J. J. Cha, J. R. McDonough, J. Zhu, Y. Yang, M. D. McGehee, and Y. Cui. Electrospun metal nanofiber webs as high-performance transparent electrode. *Nano Letters*, 10(10):4242–4248, 2010.

[30] N. A. M. Barakat, K. A. Khalil, I. H. Mahmoud, M. A. Kanjwal, F. A. Sheikh, and H. Y. Kim. Coni bimetallic nanofibers by electrospinning: Nickel-based soft magnetic material with improved magnetic properties. *The Journal of Physical Chemistry C*, 114(37):15589–15593, 2010.

[31] C.J. Thompson, G.G. Chase, A.L. Yarin, and D.H. Reneker. Effects of parameters on nanofiber diameter determined from electrospinning model. *Polymer*, 48(23):6913 – 6922, 2007.

[32] V. Beachley and X. Wen. Effect of electrospinning parameters on the nanofiber diameter and length. *Materials Science and Engineering: C*, 29(3):663 – 668, 2009.

[33] W. Cui, X. Li, S. Zhou, and J. Weng. Investigation on process parameters of electrospinning system through orthogonal experimental design. *Journal of Applied Polymer Science*, 103(5):3105–3112, 2007.

[34] S.-H. Jegal, J.-H. Park, J.-H. Kim, T.-H. Kim, U. S. Shin, T.-I. Kim, and H.-W. Kim. Functional composite nanofibers of poly(lactideco-caprolactone) containing gelatinapatite bone mimetic precipitate for bone regeneration. *Acta Biomaterialia*, 7(4):1609 – 1617, 2011.

[35] J. Nunes-Pereira, V. Sencadas, V. Correia, J. G. Rocha, and S. Lanceros-Mndez. Energy harvesting performance of piezoelectric electrospun polymer fibers and polymer/ceramic composites. *Sensors and Actuators A: Physical*, 196(0):55 – 62, 2013.

[36] C. Kim and K. S. Yang. Electrochemical properties of carbon nanofiber web as an electrode for supercapacitor prepared by electrospinning. *Applied Physics Letters*, 83(6):1216–1218, 2003.

[37] J. Lyons, C. Li, and F. Ko. Melt-electrospinning part i: processing parameters and geometric properties. *Polymer*, 45(22):7597 – 7603, 2004.

[38] V. Jacobs, R. D. Anandjiwala, and M. Maaza. The influence of electrospinning parameters on the structural morphology and diameter of electrospun nanofibers. *Journal of Applied Polymer Science*, 115(5):3130–3136, 2010.

[39] D. Li, A. Babel, S.A. Jenekhe, and Y. Xia. Nanofibers of conjugated polymers prepared by electrospinning with a two-capillary spinneret. *Advanced Materials*, 16(22):2062–2066, 2004.

[40] D. Li and Y. Xia. Direct fabrication of composite and ceramic hollow nanofibers by electrospinning. *Nano Letters*, 4(5):933–938, 2004.

[41] H. Dong, V. Nyame, A. G. MacDiarmid, and W. E. Jones. Polyaniline/poly(methyl methacrylate) coaxial fibers: The fabrication and effects of the solution properties on the morphology of electrospun core fibers. *Journal of Polymer Science Part B: Polymer Physics*, 42(21):3934–3942, 2004.

[42] Y. Zhang, Z.-M. Huang, X. Xu, C. T. Lim, and S. Ramakrishna. Preparation of core-shell structured pcl-r-gelatin bi-component nanofibers by coaxial electrospinning. *Chemistry of Materials*, 16(18):3406–3409, 2004.

[43] A.L. Yarin. Coaxial electrospinning and emulsion electrospinning of coreshell fibers. *Polymers for Advanced Technologies*, 22(3):310–317, 2011.

[44] K. M. Forward, A. Flores, and G. C. Rutledge. Production of core/shell fibers by electrospinning from a free surface. *Chemical Engineering Science*, 104(0):250 – 259, 2013.

[45] H. Qu, S. Wei, and Z. Guo. Coaxial electrospun nanostructures and their applications. *J. Mater. Chem. A*, 1:11513–11528, 2013.

[46] Z. Kurban, A. Lovell, S. M. Bennington, D. W. K. Jenkins, K. R. Ryan, M. O. Jones, N. T. Skipper, and W. I. F. David. A solution selection model for coaxial electrospinning and its application to nanostructured hydrogen storage materials. *The Journal of Physical Chemistry C*, 114(49):21201–21213, 2010.

[47] V. Pillay, C. Dott, and Y. E. et al. Choonara. A review of the effect of processing variables on the fabrication of electrospun nanofibers for drug delivery applications. *Journal of Nanomaterials*, 2013(49):1–22, 2013.

[48] G. H. Lee, J.-C. Song, and K.-B. Yoon. Controlled wall thickness and porosity of polymeric hollow nanofibers by coaxial electrospinning. *Macromolecular Research*, 18(6):571–576, 2010.

[49] A. Townsend-Nicholson and S. N. Jayasinghe. Cell electrospinning: a unique biotechnique for encapsulating living organisms for generating active biological microthreads/scaffolds. *Biomacromolecules*, 7(12):3364–3369, 2006.

[50] S. Klein, J. Kuhn, R. Avrahami, S. Tarre, M. Beliavski, M. Green, and E. Zussman. Encapsulation of bacterial cells in electrospun microtubes. *Biomacromolecules*, 10(7):1751–1756, 2009.

[51] C. Kim, Y. I. Jeong, B. T. N. Ngoc, K. S. Yang, M. Kojima, Y. A. Kim, M. Endo, and J.-W. Lee. Synthesis and characterization of porous carbon nanofibers with hollow cores through the thermal treatment of electrospun copolymeric nanofiber webs. *Small*, 3(1):91–95, 2007.

[52] D. Han and A. J. Steckl. Triaxial electrospun nanofiber membranes for controlled dual release of functional molecules. *ACS Applied Materials & Interfaces*, 5(16):8241–8245, 2013.

[53] W. Liu, C. Ni, D. Chase, and J. F. Rabolt. Preparation of multilayer biodegradable nanofibers by triaxial electrospinning. *ACS Macro Letters*, 2(6):466–468, 2013.

[54] Q. Li, R. Jiang, Y. Dou, Z. Wu, T. Huang, D. Feng, J. Yang, A. Yu, and D. Zhao. Synthesis of mesoporous carbon spheres with a hierarchical pore structure for the electrochemical double-layer capacitor. *Carbon*, 49(4):1248 – 1257, 2011.

[55] E. A. Jackson and M. A. Hillmyer. Nanoporous membranes derived from block copolymers: From drug delivery to water filtration. *ACS Nano*, 4(7):3548–3553, 2010.

[56] C. M. Murphy, M. G. Haugh, and F. J. O'Brien. The effect of mean pore size on cell attachment, proliferation and migration in collagenglycosaminoglycan scaffolds for bone tissue engineering. *Biomaterials*, 31(3):461 – 466, 2010.

[57] F. P. W. Melchels, J. Feijen, and D. W. Grijpma. A review on stereolithography and its applications in biomedical engineering. *Biomaterials*, 31(24):6121 – 6130, 2010.

[58] S. Deville. Freeze-casting of porous biomaterials: Structure, properties and opportunities. *Materials*, 3(3):1913–1927, 2010.

[59] T. G. Kim, H. J. Chung, and T. G. Park. Macroporous and nanofibrous hyaluronic acid/collagen hybrid scaffold fabricated by concurrent electrospinning and deposition/leaching of salt particles. *Acta Biomaterialia*, 4(6):1611 – 1619, 2008.

[60] Y.-Z. Cai, G.-R. Zhang, L.-L. Wang, Y.-Z. Jiang, H.-W. Ouyang, and X.-H. Zou. Novel biodegradable three-dimensional macroporous scaffold using aligned electrospun nanofibrous yarns for bone tissue engineering. *Journal of Biomedical Materials Research Part A*, 100A(5):1187–1194, 2012.

[61] S. Zhong, Y. Zhang, and C. T. Lim. Fabrication of large pores in electrospun nanofibrous scaffolds for cellular infiltration: A review. *Tissue Engineering Part B: Reviews*, 18(2):77–87, 2012.

[62] S. O. Han, W. K. Son, J. H. Youk, T. S. Lee, and W. H. Park. Ultrafine porous fibers electrospun from cellulose triacetate. *Materials Letters*, 59(2425):2998 – 3001, 2005.

[63] J. Rnjak-Kovacina and A. S. Weiss. Increasing the pore size of electrospun scaffolds. *Tissue Engineering Part B: Reviews*, 17(5):365–372, 2011.

[64] Y. Yokoyama, S. Hattori, C. Yoshikawa, Y. Yasuda, H. Koyama, T. Takato, and H. Kobayashi. Novel wet electrospinning system for fabrication of spongiform nanofiber 3-dimensional fabric. *Materials Letters*, 63(910):754 – 756, 2009.

[65] C. S. Ki, J. W. Kim, J. H. Hyun, K. H. Lee, M. Hattori, D. K. Rah, and Y. H. Park. Electrospun three-dimensional silk fibroin nanofibrous scaffold. *Journal of Applied Polymer Science*, 106(6):3922–3928, 2007.

[66] Y. H. Lee, J. H. Lee, I.-G. An, C. Kim, D. S. Lee, Y. K. Lee, and J.-D. Nam. Electrospun dual-porosity structure and biodegradation morphology of montmorillonite reinforced plla nanocomposite scaffolds. *Biomaterials*, 26(16):3165 – 3172, 2005.

[67] J. Nam, Y. Huang, S. Agarwal, and J. Lannutti. Improved cellular infiltration in electrospun fiber via engineered porosity. *Tissue Engineering*, 13(9):2249–2257, 2007.

[68] M. Bognitzki, W. Czado, T. Frese, A. Schaper, M. Hellwig, M. Steinhart, A. Greiner, and J. H. Wendorff. Nanostructured fibers via electrospinning. *Advanced Materials*, 13(1):70–72, 2001.

[69] S. Megelski, J. S. Stephens, D. B. Chase, and J. F. Rabolt. Micro- and nanostructured surface morphology on electrospun polymer fibers. *Macromolecules*, 35(22):8456–8466, 2002.

[70] J. Lin, F. Tian, Y. Shang, F. Wang, B. Ding, and J. Yu. Facile control of intra-fiber porosity and inter-fiber voids in electrospun fibers for selective adsorption. *Nanoscale*, 4:5316–5320, 2012.

[71] Z. Zhang, X. Li, C. Wang, S. Fu, Y. Liu, and C. Shao. Polyacrylonitrile and carbon nanofibers with controllable nanoporous structures by electrospinning. *Macromolecular Materials and Engineering*, 294(10):673–678, 2009.

[72] M. Mehraban, A. Zadhoush, S. Abdolkarim Hosseini Ravandi, R. Bagheri, and A. Heidarkhan Tehrani. Preparation of porous nanofibers from electrospun polyacrylonitrile/calcium carbonate composite nanofibers using porogen leaching technique. *Journal of Applied Polymer Science*, 128(2):926–933, 2013.

[73] American Chemical Society National Historic Chemical Landmarks Staff. Bakelite: The worlds first synthetic plastic. Technical report, American Chemical Society National Historic Chemical Landmarks, 2013.

[74] G. Llanos. Crosslinked polyethylene oxide coatings to improve the biocompatibility of implantable medical devices. Technical Report 5,507,804, United States Patent, 1996.

[75] R. G. Mason, D. E. Scarborough, S. R. Saba, K. M. Brinkhous, L. D. Ikenberry, J. J. Kearney, and H. G. Clark. Thrombogenicity of some biomedical materials: Platelet-interface reactions. *Journal of Biomedical Materials Research*, 3(4):615–644, 1969.

[76] K. Knop, R. Hoogenboom, D. Fischer, and U.S. Schubert. Poly(ethylene glycol) in drug delivery: Pros and cons as well as potential alternatives. *Angewandte Chemie International Edition*, 49(36):6288–6308, 2010.

[77] Y. Ji, K. Ghosh, X. Z. Shu, B. Li, J. C. Sokolov, G. D. Prestwich, R. A. F. Clark, and M. H. Rafailovich. Electrospun three-dimensional hyaluronic acid nanofibrous scaffolds. *Biomaterials*, 27(20):3782 – 3792, 2006.

[78] J.-W. Lu, Y.-L. Zhu, Z.-X. Guo, P. Hu, and J. Yu. Electrospinning of sodium alginate with poly(ethylene oxide). *Polymer*, 47(23):8026 – 8031, 2006.

[79] S. Safi, M. Morshed, S. A. Hosseini Ravandi, and M. Ghiaci. Study of electrospinning of sodium alginate, blended solutions of sodium alginate/poly(vinyl alcohol) and sodium alginate/poly(ethylene oxide). *Journal of Applied Polymer Science*, 104(5):3245–3255, 2007.

[80] R. A. A. Muzzarelli, F. Greco, A. Busilacchi, V. Sollazzo, and A. Gigante. Chitosan, hyaluronan and chondroitin sulfate in tissue engineering for cartilage regeneration: A review. *Carbohydrate Polymers*, 89(3):723 – 739, 2012.

[81] I. Villanueva, S. K. Gladem, J. Kessler, and S. J. Bryant. Dynamic loading stimulates chondrocyte biosynthesis when encapsulated in charged hydrogels prepared from poly(ethylene glycol) and chondroitin sulfate. *Matrix Biology*, 29(1):51 – 62, 2010.

[82] S. Jo, D. Kim, J. Woo, G. Yoon, Y. D. Park, G. Tae, and I. Noh. Development and physicochemical evaluation of chondroitin sulfate-poly(ethylene oxide) hydrogel. *Macromolecular Research*, 19(2):147–155, 2011.

[83] J. Zhu. Bioactive modification of poly(ethylene glycol) hydrogels for tissue engineering. *Biomaterials*, 31(17):4639 – 4656, 2010.

[84] J. B. Lando and W. W. Doll. The polymorphism of poly(vinylidene fluoride). i. the effect of head-to-head structure. *Journal of Macromolecular Science, Part B*, 2(2):205–218, 1968.

[85] A. J. Lovinger, G. T. Davis, T. Furukawa, and M. G. Broadhurst. Crystalline forms in a copolymer of vinylidene fluoride and trifluoroethylene (52/48 mol *Macromolecules*, 15(2):323–328, 1982.

[86] J. P. Luongo. Far-infrared spectra of piezoelectric polyvinylidene fluoride. *Journal of Polymer Science Part A-2: Polymer Physics*, 10(6):1119–1123, 1972.

[87] D. R. Dillon, K. K. Tenneti, C. Y. Li, F. K. Ko, I. Sics, and B. S. Hsiao. On the structure and morphology of polyvinylidene fluoridenanoclay nanocomposites. *Polymer*, 47(5):1678 – 1688, 2006.

[88] Q. Wang and L. Zhu. Polymer nanocomposites for electrical energy storage. *Journal of Polymer Science Part B: Polymer Physics*, 49(20):1421–1429, 2011.

[89] O. Martnez, A. G. Bravo, and N. J. Pinto. Fabrication of poly(vinylidene fluoridetrifluoroethylene)/poly(3,4-ethylenedioxythiophene)polystyrene sulfonate composite nanofibers via electrospinning. *Macromolecules*, 42(20):7924–7929, 2009.

[90] A. Ferreira, J. Silva, V. Sencadas, J. L. G. Ribelles, and S. Lanceros-Mndez. Poly[(vinylidene fluoride)-co-trifluoroethylene] membranes obtained by isother-

mal crystallization from solution. *Macromolecular Materials and Engineering*, 295(6):523–528, 2010.

[91] P. Martins, X. Moya, L. C. Phillips, S. Kar-Narayan, N. D. Mathur, and S. Lanceros-Mendez. Linear anhysteretic direct magnetoelectric effect in ni0.5zn0.5fe2*o*4/poly(vinylidene fluoride-trifluoroethylene) 0–3 nanocomposites. *Journal of Physics D: Applied Physics*, 44(48):1–4, 2011.

[92] R. Costa, C. Ribeiro, A.C. Lopes, P. Martins, V. Sencadas, R. Soares, and S. Lanceros-Mendez. Osteoblast, fibroblast and in vivo biological response to poly(vinylidene fluoride) based composite materials. *Journal of Materials Science: Materials in Medicine*, 24(2):395–403, 2013.

[93] P. Martins, A.C. Lopes, and S. Lanceros-Mendez. Electroactive phases of poly(vinylidene fluoride): Determination, processing and applications. *Progress in Polymer Science*, 39(4):683 – 706, 2014.

[94] A.C. Lopes, C. Caparros, J.L. Gmez Ribelles, I.C. Neves, and S. Lanceros-Mendez. Electrical and thermal behavior of -phase poly(vinylidene fluoride)/nay zeolite composites. *Microporous and Mesoporous Materials*, 161(0):98 – 105, 2012.

[95] B.L. Atkins, R.N. Bashaw, and B.G. Harper. Absorbent product containing a hydrocelloidal composition, 1972. US Patent 3,669,103.

[96] E. Carretti, L. Dei, and P. Baglioni. Aqueous polyacrylic acid based gels: physicochemical properties and applications in cultural heritage conservation. In M. Miguel and H. D. Burrows, editors, *Trends in Colloid and Interface Science XVI*, volume 123 of *Progress in Colloid and Polymer Science*, pages 280–283. Springer Berlin Heidelberg, 2004.

[97] Y. Zheng, S. Hua, and A. Wang. Adsorption behavior of cu2+ from aqueous so-

lutions onto starch-g-poly(acrylic acid)/sodium humate hydrogels. *Desalination*, 263(13):170 – 175, 2010.

[98] A. Rsler, G. W.M. Vandermeulen, and HA. Klok. Advanced drug delivery devices via self-assembly of amphiphilic block copolymers. *Advanced Drug Delivery Reviews*, 64, Supplement:270 – 279, 2012.

[99] E. N. Chiang, R. Dong, C. K. Ober, and B. A. Baird. Cellular responses to patterned poly(acrylic acid) brushes. *Langmuir*, 27(11):7016–7023, 2011.

[100] R. Xu, M. Jia, F. Li, H. Wang, B. Zhang, and J. Qiao. Preparation of mesoporous poly (acrylic acid)/sio2 composite nanofiber membranes having adsorption capacity for indigo carmine dye. *Applied Physics A*, 106(3):747–755, 2012.

[101] C. R. Kinnane, G. K. Such, and F. Caruso. Tuning the properties of layer-by-layer assembled poly(acrylic acid) click films and capsules. *Macromolecules*, 44(5):1194–1202, 2011.

[102] K.D. McKeon-Fischer, D.H. Flagg, and J.W. Freeman. Poly(acrylic acid)/poly(vinyl alcohol) compositions coaxially electrospun with poly(-caprolactone) and multi-walled carbon nanotubes to create nanoactuating scaffolds. *Polymer*, 52(21):4736 – 4743, 2011.

[103] A. Awadallah-F. Five years in vitro study of (poly vinyl alcohol/poly vinyl pyrrolidone/poly acrylic acid) hydrogel to mimic the knee joint meniscus. *Polymers for Advanced Technologies*, 25(5):581–587, 2014.

[104] J. H. Hamman. Chitosan based polyelectrolyte complexes as potential carrier materials in drug delivery systems. *Marine Drugs*, 8(4):1305–1322, 2010.

[105] A. A. Antipov, D. Shchukin, Y. Fedutik, A. I. Petrov, G. B. Sukhorukov, and H. Mhwald. Carbonate microparticles for hollow polyelectrolyte capsules fabrication. *Col-*

loids and Surfaces A: Physicochemical and Engineering Aspects, 224(13):175 – 183, 2003.

[106] K. Itano, J. Choi, and M. F. Rubner. Mechanism of the ph-induced discontinuous swelling/deswelling transitions of poly(allylamine hydrochloride)-containing polyelectrolyte multilayer films. *Macromolecules*, 38(8):3450–3460, 2005.

[107] L. Wgberg, G. Decher, M. Norgren, T. Lindstrm, M. Ankerfors, and K. Axns. The build-up of polyelectrolyte multilayers of microfibrillated cellulose and cationic polyelectrolytes. *Langmuir*, 24(3):784–795, 2008.

[108] A. Szarpak, I. Pignot-Paintrand, C. Nicolas, C. Picart, and R. Auzly-Velty. Multilayer assembly of hyaluronic acid/poly(allylamine): Control of the buildup for the production of hollow capsules. *Langmuir*, 24(17):9767–9774, 2008.

[109] S. Srivastava and N. A. Kotov. Composite layer-by-layer (lbl) assembly with inorganic nanoparticles and nanowires. *Accounts of Chemical Research*, 41(12):1831–1841, 2008.

[110] C. Qiu, S. Qi, and C. Y. Tang. Synthesis of high flux forward osmosis membranes by chemically crosslinked layer-by-layer polyelectrolytes. *Journal of Membrane Science*, 381(12):74 – 80, 2011.

[111] A. Chunder, S. Sarkar, Y. Yu, and L. Zhai. Fabrication of ultrathin polyelectrolyte fibers and their controlled release properties. *Colloids and Surfaces B: Biointerfaces*, 58(2):172 – 179, 2007.

[112] S. Kundu, R. S. Gill, and R. F. Saraf. Electrospinning of pah nanofiber and deposition of au nps for nanodevice fabrication. *The Journal of Physical Chemistry C*, 115(32):15845–15852, 2011.

[113] J. D. Schiffman, M. A. Kiechel, A. E. Donius, U. G. K. Wegst, and C. L. Schauer. Crosslinking poly(allylamine) fibers electrospun from basic and acidic solutions. *Journal of Materials Science*, 48(22):7856–7862, 2013.

[114] O. Bukal, M. Schachner, and A. Dityatev. Modification of extracellular matrix by enzymatic removal of chondroitin sulfate and by lack of tenascin-r differentially affects several forms of synaptic plasticity in the hippocampus. *Neuroscience*, 104(2):359 – 369, 2001.

[115] D. Uebelhart, M. Malaise, R. Marcolongo, F. DeVathaire, M. Piperno, E. Mailleux, A. Fioravant, L. Matoso, and E. Vignon. Intermittent treatment of knee osteoarthritis with oral chondroitin sulfate: a one-year, randomized, double-blind, multicenter study versus placebo. *Osteoarthritis and Cartilage*, 12(4):269 – 276, 2004.

[116] D. Uebelhart. Clinical review of chondroitin sulfate in osteoarthritis. *Osteoarthritis and Cartilage*, 16, Supplement 3(0):S19 – S21, 2008.

[117] Y. Lee, J. Woo, S. Choi, J. Ji, and G. Song. Effect of glucosamine or chondroitin sulfate on the osteoarthritis progression: a meta-analysis. *Rheumatology International*, 30(3):357–363, 2010.

[118] S. Yamada and K. Sugahara. Potential therapeutic application of chondroitin sulfate/dermatan sulfate. *Current Drug Discovery Technologies*, 5(4):289–301, 2008-12-01T00:00:00.

[119] J. M. Coburn, M. Gibson, S. Monagle, Z. Patterson, and J. H. Elisseeff. Bioinspired nanofibers support chondrogenesis for articular cartilage repair. *Proceedings of the National Academy of Sciences*, 109(25):10012–10017, 2012.

[120] C. Lee, P. Kung, and Y. Lee. Preparation of poly(vinyl alcohol)-chondroitin sulfate hydrogel as matrices in tissue engineering. *Carbohydrate Polymers*, 61(3):348 – 354, 2005.

[121] S. Varghese, N. S. Hwang, A. C. Canver, P. Theprungsirikul, D. W. Lin, and J. Elisseeff. Chondroitin sulfate based niches for chondrogenic differentiation of mesenchymal stem cells. *Matrix Biology*, 27(1):12 – 21, 2008.

[122] J. R. E. Fraser, T. C. Laurent, and U. B. G. Laurent. Hyaluronan: its nature, distribution, functions and turnover. *Journal of Internal Medicine*, 242(1):27–33, 1997.

[123] J. A. Burdick and G. D. Prestwich. Hyaluronic acid hydrogels for biomedical applications. *Advanced Materials*, 23(12):H41–H56, 2011.

[124] G. Kogan, L. olts, R. Stern, and P. Gemeiner. Hyaluronic acid: a natural biopolymer with a broad range of biomedical and industrial applications. *Biotechnology Letters*, 29(1):17–25, 2007.

[125] R. R. Bannuru, N. S. Natov, U. R. Dasi, C. H. Schmid, and T. E. McAlindon. Therapeutic trajectory following intra-articular hyaluronic acid injection in knee osteoarthritis meta-analysis. *Osteoarthritis and Cartilage*, 19(6):611 – 619, 2011.

[126] J. R. E. Fraser, L. Appelgren, and T. C. Laurent. Tissue uptake of circulating hyaluronic acid. *Cell and Tissue Research*, 233(2):285–293, 1983.

[127] C. E. Schant, G. Zuber, C. Herlin, and T. F. Vandamme. Chemical modifications of hyaluronic acid for the synthesis of derivatives for a broad range of biomedical applications. *Carbohydrate Polymers*, 85(3):469 – 489, 2011.

[128] W. S. Toh, E. H. Lee, X. Guo, J. K. Y. Chan, C. H. Yeow, A. B. Choo, and T. Cao. Cartilage repair using hyaluronan hydrogel-encapsulated human embryonic stem cell-derived chondrogenic cells. *Biomaterials*, 31(27):6968 – 6980, 2010.

[129] M. D. Shoulders and R. T. Raines. Collagen structure and stability. *Annual review of biochemistry*, 78:929–958, 2009.

[130] A. Asghar and R. L. Henrickson. *Advances in food research*, volume 28, chapter Chemical, biochemical, functional, and nutritional characteristics of collagen in food systems, pages 232 – 372. London: Academic Press, 1982.

[131] C. H. Lee, A. Singla, and Y. Lee. Biomedical applications of collagen. *International Journal of Pharmaceutics*, 221(12):1 – 22, 2001.

[132] B. D. Ulery, L. S. Nair, and C. T. Laurencin. Biomedical applications of biodegradable polymers. *Journal of Polymer Science Part B: Polymer Physics*, 49(12):832–864, 2011.

[133] S. Rammelt, T. Illert, S. Bierbaum, D. Scharnweber, H. Zwipp, and W. Schneiders. Coating of titanium implants with collagen, rgd peptide and chondroitin sulfate. *Biomaterials*, 27(32):5561 – 5571, 2006.

[134] G. S. Jeong, G. H. Kwon, A. R. Kang, B. Y. Jung, Y. Park, S. Chung, and S. Lee. Microfluidic assay of endothelial cell migration in 3d interpenetrating polymer semi-network ha-collagen hydrogel. *Biomedical Microdevices*, 13(4):717–723, 2011.

[135] Y. Lin, F. Tan, K. G. Marra, S. Jan, and D. Liu. Synthesis and characterization of collagen/hyaluronan/chitosan composite sponges for potential biomedical applications. *Acta Biomaterialia*, 5(7):2591 – 2600, 2009.

[136] J. A. Matthews, G. E. Wnek, D. G. Simpson, and G. L. Bowlin. Electrospinning of collagen nanofibers. *Biomacromolecules*, 3(2):232–238, 2002.

[137] K. S. Rho, L. Jeong, G. Lee, B. Seo, Y. J. Park, S. Hong, S. Roh, J. J. Cho, W. H. Park, and B. Min. Electrospinning of collagen nanofibers: Effects on the behavior of normal human keratinocytes and early-stage wound healing. *Biomaterials*, 27(8):1452 – 1461, 2006.

[138] M.C. Gmez-Guilln, B. Gimnez, M.E. Lpez-Caballero, and M.P. Montero. Functional and bioactive properties of collagen and gelatin from alternative sources: A review. *Food Hydrocolloids*, 25(8):1813 – 1827, 2011. 25 years of Advances in Food Hydrocolloid Research.

[139] P. Taddei, V. Chiono, A. Anghileri, G. Vozzi, G. Freddi, and G. Ciardelli. Silk fibroin/gelatin blend films crosslinked with enzymes for biomedical applications. *Macromolecular Bioscience*, 13(11):1492–1510, 2013.

[140] V. Chiono, E. Pulieri, G. Vozzi, G. Ciardelli, A. Ahluwalia, and P. Giusti. Genipin-crosslinked chitosan/gelatin blends for biomedical applications. *Journal of Materials Science: Materials in Medicine*, 19(2):889–898, 2008.

[141] K. Pal, A. K. Banthia, and D. K. Majumdar. Preparation and characterization of polyvinyl alcohol-gelatin hydrogel membranes for biomedical applications. *AAPS PharmSciTech*, 8(1):E142–E146, 2007.

[142] Y. Zhang, H. Ouyang, C. T. Lim, S. Ramakrishna, and Z.-M. Huang. Electrospinning of gelatin fibers and gelatin/pcl composite fibrous scaffolds. *Journal of Biomedical Materials Research Part B: Applied Biomaterials*, 72B(1):156–165, 2005.

[143] J. Li, A. He, J. Zheng, and C. C. Han. Gelatin and gelatin-hyaluronic acid nanofibrous membranes produced by electrospinning of their aqueous solutions. *Biomacromolecules*, 7:2243–2247, 2006.

[144] W.-H. Lin and W.-B. Tsai. In situ uv-crosslinking gelatin electrospun fibers for tissue engineering applications. *Biofabrication*, 5(3):035008, 2013.

[145] M. Skotak, S. Noriega, G. Larsen, and A. Subramanian. Electrospun cross-linked gelatin fibers with controlled diameter: The effect of matrix stiffness on proliferative and biosynthetic activity of chondrocytes cultured in vitro. *Journal of Biomedical Materials Research Part A*, 95A(3):828–836, 2010.

[146] P. Zhao, H. Jiang, H. Pan, K. Zhu, and W. Chen. Biodegradable fibrous scaffolds composed of gelatin coated poly(-caprolactone) prepared by coaxial electrospinning. *Journal of Biomedical Materials Research Part A*, 83A(2):372–382, 2007.

[147] H. M. Powell and S. T. Boyce. Fiber density of electrospun gelatin scaffolds regulates morphogenesis of dermalepidermal skin substitutes. *Journal of Biomedical Materials Research Part A*, 84A(4):1078–1086, 2008.

[148] K. S. Weadock, E. J. Miller, E. L. Keuffel, and M. G. Dunn. Effect of physical crosslinking methods on collagen-fiber durability in proteolytic solutions. *Journal of Biomedical Materials Research*, 32(2):221–226, 1996.

[149] I. V. Yannas and A. V. Tobolsky. Cross-linking of gelatine by dehydration, 1967.

[150] M. M. Pakulska, K. Vulic, and M. S. Shoichet. Affinity-based release of chondroitinase abc from a modified methylcellulose hydrogel. *Journal of Controlled Release*, 171(1):11 – 16, 2013.

[151] Z. Huang, Y. Z. Zhang, S. Ramakrishna, and C. T. Lim. Electrospinning and mechanical characterization of gelatin nanofibers. *Polymer*, 45(15):5361 – 5368, 2004.

[152] T. A. Telemeco, C. Ayres, G. L. Bowlin, G. E. Wnek, E. D. Boland, N. Cohen, C. M. Baumgarten, J. Mathews, and D.G. Simpson. Regulation of cellular infiltration into tissue engineering scaffolds composed of submicron diameter fibrils produced by electrospinning. *Acta Biomaterialia*, 1(4):377 – 385, 2005.

[153] N. Choktaweesap, K. Arayanarakul, D. Aht-ong, C. Meechaisue, and P. Supaphol. Electrospun gelatin fibers: Effect of solvent system on morphology and fiber diameters. *Polymer Journal*, (6):622–631, 2007.

[154] J. E. Eastoe. The amino acid composition of mammalian collagen and gelatin. *Biochemical Journal*, 61(4):589, 1955.

[155] S. Suarasan, M. Focsan, D. Maniu, and S. Astilean. Gelatinnanogold bioconjugates as effective plasmonic platforms for sers detection and tagging. *Colloids and Surfaces B: Biointerfaces*, 103:475 – 481, 2013.

[156] K. J. Payne and A. Veis. Fourier transform ir spectroscopy of collagen and gelatin solutions: Deconvolution of the amide i band for conformational studies. *Biopolymers*, 27(11):1749–1760, 1988.

[157] S. Tsai, H. Liou, C. Lin, K. Kuo, Y. Hung, R. Weng, and F. Hsu. Mg63 osteoblast-like cells exhibit different behavior when grown on electrospun collagen matrix versus electrospun gelatin matrix. *PLoS ONE*, 7(2):e31200, 02 2012.

[158] Y. Zhang, V. J. Reddy, S. Y. Wong, X. Li, B. Su, S. Ramakrishna, and C. T. Lim. Enhanced biomineralization in osteoblasts on a novel electrospun biocomposite nanofibrous substrate of hydroxyapatite/collagen/chitosan. *Tissue Engineering Part A*, 16(6):1949–1960, 2010.

[159] Y. S. Lee and T. L. Arinzeh. The influence of piezoelectric scaffolds on neural differentiation of human neural stem/progenitor cells. *Tissue Engineering Part A*, 18(19-20):2063–2072, 2012.

[160] N. Weber, Y. S. Lee, S. Shanmugasundaram, M. Jaffe, and T. L. Arinzeh. Characterization and in vitro cytocompatibility of piezoelectric electrospun scaffolds. *Acta Biomaterialia*, 6(9):3550 – 3556, 2010.

[161] H. F. Guo, Z. S. Li, S. W. Dong, W. J. Chen, L. Deng, Y. F. Wang, and D. J. Ying. Piezoelectric pu/pvdf electrospun scaffolds for wound healing applications. *Colloids and Surfaces B: Biointerfaces*, 96(0):29 – 36, 2012.

[162] Y. S. Lee, G. Collins, and T. L. Arinzeh. Neurite extension of primary neurons on electrospun piezoelectric scaffolds. *Acta Biomaterialia*, 7(11):3877 – 3886, 2011.

[163] R.D. Simoes, M.A. Rodriguez-Perez, J.A. De Saja, and C.J.L. Constantino. Tailoring the structural properties of pvdf and p(vdf-trfe) by using natural polymers as additives. *Polymer Engineering & Science*, 49(11):2150–2157, 2009.

[164] J. D. A. S. Pereira, R. C. T. Camargo, J. C. S. C. Filho, N. Alves, M. A. Rodriguez-Perez, and C. J. L. Constantino. Biomaterials from blends of fluoropolymers and corn starchimplant and structural aspects. *Materials Science and Engineering: C*, 36(0):226 – 236, 2014.

[165] W. K. Son, J. H. Youk, T. S. Lee, and W. H. Park. The effects of solution properties and polyelectrolyte on electrospinning of ultrafine poly(ethylene oxide) fibers. *Polymer*, 45(9):2959 – 2966, 2004.

[166] J. M. Deitzel, J.D. Kleinmeyer, J.K. Hirvonen, and N.C. Beck Tan. Controlled deposition of electrospun poly(ethylene oxide) fibers. *Polymer*, 42(19):8163 – 8170, 2001.

[167] G. M. Castillo and D. M. Templeton. Subunit structure of bovine esf (extracellular-matrix stabilizing factor(s)): A chondroitin sulfate proteoglycan with homology to human ii (inter--trypsin inhibitors). *FEBS Letters*, 318(3):292 – 296, 1993.

[168] S.E. Noriega, G.I. Hasanova, M.J. Schneider, G.F. Larsen, and A. Subramanian. Effect of fiber diameter on the spreading, proliferation and differentiation of chondrocytes on electrospun chitosan matrices. *Cells Tissues Organs*, 195(3):207 – 221, 2012.

[169] L. Li and Y. Hsieh. Ultra-fine polyelectrolyte fibers from electrospinning of poly(acrylic acid). *Polymer*, 46(14):5133 – 5139, 2005.

[170] B. Kim, H. Park, S. Lee, and W. M. Sigmund. Poly(acrylic acid) nanofibers by electrospinning. *Materials Letters*, 59(7):829 – 832, 2005.

[171] J. S. Atchison and C. L. Schauer. Fabrication and characterization of electrospun semiconductor nanoparticlepolyelectrolyte ultra-fine fiber composites for sensing applications. *Sensors*, (11), 2011.

[172] E. K. Brenner, J. D. Schiffman, E. A. Thompson, L. J. Toth, and C. L. Schauer. Electrospinning of hyaluronic acid nanofibers from aqueous ammonium solutions. *Carbohydrate Polymers*, 87(1):926 – 929, 2012.

[173] J. Li, A. He, C. C. Han, D. Fang, B. S. Hsiao, and B. Chu. Electrospinning of hyaluronic acid (ha) and ha/gelatin blends. *Macromolecular Rapid Communications*, 27(2):114–120, 2006.

[174] E. K. Brenner, J. D. Schiffman, L. J. Toth, J. C. Szewczyk, and C. L. Schauer. Phosphate salts facilitate the electrospinning of hyaluronic acid fiber mats. *Journal of Materials Science*, 48(22):7805–7811, 2013.

[175] T. G. Kim, H. J. Chung, and T. G. Park. Macroporous and nanofibrous hyaluronic acid/collagen hybrid scaffold fabricated by concurrent electrospinning and deposition/leaching of salt particles. *Acta Biomaterialia*, 4(6):1611 – 1619, 2008.

[176] L. Ng, A. Plaas, A. Grodzinsky, and C. Ortiz. Structure, conformation, and self-assembly of cartilage polyelectrolyte macromolecules studied via atomic force microscopy. *DIM*, 100:200, 2002.

[177] J. D. Schiffman, M. A. Kiechel, A. E. Donius, U. G. K. Wegst, and C. L. Schauer. Crosslinking poly(allylamine) fibers electrospun from basic and acidic solutions. *Journal of Materials Science*, 48(22):7856–7862, 2013.

[178] R. S. Gill, R. F. Saraf, and S. Kundu. Self-assembly of gold nanoparticles on poly(allylamine hydrochloride) nanofiber: A new route to fabricate necklace as single electron devices. *ACS Applied Materials & Interfaces*, 5(20):9949–9956, 2013.

[179] S. Kundu, R. S. Gill, and R. F. Saraf. Electrospinning of pah nanofiber and deposition of au nps for nanodevice fabrication. *The Journal of Physical Chemistry C*, 115(32):15845–15852, 2011.

[180] H. Chen, A. Chunder, X. Liu, F. Haque, J. Zou, L. Austin, G. Knowles, L. Zhai, and Q. Huo. A multifunctional gold nanoparticle/polyelectrolyte fibrous nanocomposite prepared from electrospinning process. *Materials Express*, 1(2):154–159, 2011-06-01T00:00:00.

[181] L. Ge, C. Pan, H. Chen, X. Wang, C. Wang, and Z. Gu. The fabrication of hollow multilayered polyelectrolyte fibrous mats and its morphology study. *Colloids and Surfaces A: Physicochemical and Engineering Aspects*, 293(13):272 – 277, 2007.